GREENER SYNTHESES OF METALLIC NANOPARTICLES AND ZINC OXIDE NANOPOWDERS

by

JACOPO SAMSON

A dissertation submitted to the Graduate Faculty in Chemistry in partial fulfillment of the requirements for the degree of Doctor of Philosophy,

The City University of New York

2011

This manuscript has been read and accepted for the
Graduate Faculty in Chemistry in satisfaction of the dissertation requirement
for the degree of Doctor of Philosophy.

Dr. Charles Michael Drain

_____

September 7, 2011 Chair of Examining Committee

Dr. Maria Tamargo

_____

September 7, 2011 Executive Officer

Dr. Spiro Alexandratos

Dr. Harry Gafney

Dr. Frida Kleiman

Supervisory Committee

THE CITY UNIVERSITY OF NEW YORK

Abstract

Greener Syntheses of Metallic Nanoparticles and Zinc Oxide Nanopowders

by

Jacopo Samson

Adviser: Professor Charles Michael Drain

In recent years, nanotechnology and nanomaterials synthesis have attracted a great deal of attention in the scientific community. Nanomaterials display size and morphology-related optical properties that differ from their bulk counterparts and therefore can be used for many applications in different fields such as biomedicine, electronics, antibacterial agents, and energy. Attempts to fabricate different morphologies of metallic and metal oxide nanoparticles (NPs) have successfully yielded attractive nanostructures such as particles, rods, helices, combs, tetra-pods, and flowers, all displaying properties mainly related to their enhanced surface area and/or aspect ratios. Most of the above mentioned nanomaterials productions have employed harsh synthetic routes such as high temperatures, low pressures, and the use of costly equipments. Here we show how a greener approach to nanomaterials synthesis is feasible with both minimization of aqueous precursors, energy and employment of a multi-block heater for temperature control.

We present in this thesis several methods for the preparation of NPs of several materials that focus on minimizing the environmental impact of the synthesis itself. First, we describe the use of the toroidal form of plasmid DNA as a rigid narrowly dispersed bio-polymeric nanocavity, which mold the formation of disc-shaped nanoparticles of several types of metals. This approach exploits several properties of plasmid DNA: (a) DNA affinity for metal cations, (b) toroidal plasmid DNA structures which are favored by metal ionic binding, and (c) the ability to vary

plasmid size. Herein, we present a complementary synthetic method based on a kinetic approach wherein the plasmid DNA acts as a template to initiate and control the formation of Au and other metallic NPs by incubation at elevated temperatures.

Also reported herein is a simple, scalable hydrothermal method to make ZnO NPs that exploits temperature to precisely control the range of pH values of an organic amine buffer. The presence or absence of ethylenediaminetetraacetic acid in the tris(hydroxymethyl)aminomethane buffer further modulates the morphology of the ZnO nanomaterials since both compounds can serve as nucleating sites, and as stabilizing agents that prevents agglomeration.

To simplify the identification of the materials formed in these new methods, when one has an idea what the material might be, and standards with which to compare them, we present two easily applied and straightforward methods for analysis of electron diffraction (ED) patterns. Identifying total unknowns, however, will still require indexing individual diffraction patterns.

Acknowledgments

The encouragement and support of many people have contributed to the successful outcome of this dissertation. First and foremost, I would like to extend thanks and appreciation to my adviser, Dr. Charles Michael Drain for his generous time, commitment, and expertise. I would also like to thank my colleagues and friends: Dr. Ivana Radivojevic, Dr. Sebastian Thompson, Dr. Alessandro Varotto, Dr. Giorgio Bazzan, Dr. Gabriela Smeureanu, my current lab mates, above all Chris Farley, and the undergraduate students who have helped me with proofreading my thesis and manuscripts, especially Alex Yampolsky. I owe special thanks to my doctoral committee: Drs. Alexandratos, Kleiman, Gafney, Matsui, and Nahirney, one of the best histologists I have ever encountered. Special thanks to Irene Piscopo whose expertise and vibrancy have given me the opportunity to appreciate the effectiveness and improve my understanding of the transmission electron microscope. I would also like to thank my family, especially my parents, Mamma and Papa`, whose hard work and determination in their own lives as well as their encouragement inspired me to reach for this goal. Last but not least, I am especially grateful to my wife Victoria, who has been so supportive and has helped me greatly through this incredible journey.

Dedicated to my parents, Anna and Stefan, my brother Reuben, my wife Victoria, and The Bump

Table of Contents

List of Figures

List of Tables, Schemes and Charts

List of Appendices

Chapter 1

NANOTECHNOLOGY AND NANOPARTICLE APPLICATIONS

1.1 Introduction: Nanotechnology

Nanotechnology, commonly referred to as "nanotech," is the study of manipulating matter on an atomic and molecular scale. The purpose of nanotechnology is to synthesize structures that measure between 1 to 100 nm in at least one dimension, roughly corresponding to a size 10 to 1000 times larger than the average atomic radius (Figure 1.1). This technology involves the fabrication of materials or devices that possess at least one dimension in the above-referenced size range.

The transition from bulk materials to nanoscale structures is associated with numerous changes in physical properties. Two of the most significant factors that contribute to these changes are: (1) an exponential increase in the nanoparticles' (NPs) surface area to volume ratio; and (2) the behavior of the nanoparticles – because of their minute size, the NPs behave according to a quantum regulated realm [1]. As a result of the increase in surface area to volume ratio, the atoms on the surface of the NP usually dictate the chemical properties over the inner atoms, affecting the collective properties of the nanoparticles [2].

Because of its ability to modify physical properties, nanotechnology has evolved into a diverse discipline, ranging from the optimization of conventional devices to novel approaches based upon molecular self-assembly: from developing new materials with nanoscale dimensions, to investigating whether matter can be directly controlled on the atomic scale. One of the aims of nanotechnology is to create novel properties that arise from the shape and size of newly synthesized nanomaterials, which can be used in a wide variety of fields, including: medicine, electronics, biomaterials and energy production. Over the last decade, hundreds of companies, including NanoInk, NanoSurf, NanoTerra and Nanobiomatters, have recognized the importance of nanotechnology, invested in resources, and brought the benefits of this emerging field to everyday life.

Although companies recognize its benefits, the future implications of nanotechnology are the subject of much debate. On the one hand, in addition to the state of art constructs and devices [3, 4], nanotechnologists are working to overcome challenges, such as the need to engineer drug delivery systems capable of eradicating cancer [5] and extremely sensitive diagnostic tools to prevent the development of initial tumors [6]. Additionally, they hope to obtain the ability to develop tools that can provide viable energy alternatives to gasoline [7]. Over the past 3 or 4 years, nanotechnology has experienced such extensive progress that the reality of nano-robots able to repair biomedical tissue on the inside of the human body no longer seems like an illusory idea [8]. On the other hand, because nanotechnology is a relatively new field of science, there is general concern about the toxicity and environmental impact these nanomaterials may pose [9].

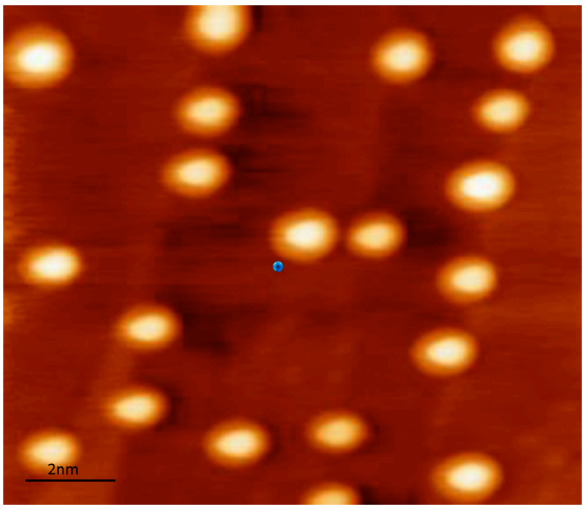

Figure 1.1. AFM phase image representing narrowly dispersed AuNPs forming inside the cavity of a 70 base-pair segment of DNA which act as a template (image took using a "DI" AFM). The blue sphere in the center represents the radius of diatomic hydrogen.

1.2 Nanoparticles

Most of today's nanotechnology-related applications are feasible because of the considerable efforts made to synthesize newly-shaped and size-controlled nanoparticles (NPs) and nanostructures (NSs). In recent years, the need for fabricating nanomaterials such as NPs or NSs has risen drastically. Evidence of this increased need can be observed by typing the keywords "nanoparticles" or "nanostructure" into the Scifinder scientific database. Approximately 11,000 (as of 7/20/2011) papers containing these words in the title are available.

1.2.1 Gold Nanoparticles

Despite nanotechnology being a fairly new discipline, "nano-gold" has been around since ancient times and was used mainly for glass-coloring purposes. One of the earliest scientific reports mentioning gold not in the bulk state is traceable back to Michael Faraday, the English chemist and physicist who is considered to be one of the fathers of modern nanotechnology. In

1897, Faraday described the sudden color change of a solution into deep red, after an aqueous precursor, hydrogen tetrachloroaurate, was reduced by carbon disulfide (CS_2). Four year later, Sir Graham, referring to this new "form" of gold aggregates, coined the terminology "colloidal" gold. As Faraday first observed, by studying the optical properties of the thin films fabricated using some of his dried products, this colloidal material differed from the bulk gold. Since then, many studies have confirmed that gold nanocolloids (with dimensions below 20 nm) differ from their corresponding bulk material because they display fundamentally different physical properties, as well as new optical properties [10]. Indeed, narrowly dispersed colloidal gold nanostructures (as well as other different metallic nanostructures) exhibit a broad absorption band that is completely absent in the bulk spectra [11]. As a consequence, solutions containing gold NPs exhibit a variety of colors, which can be detected by the naked eye, that correspond to specific wavelengths of absorption strictly dependent on the size and shape, and to some extent the dispersity, of the NPs in solution (Figure 1.2) [2]. For instance, a solution with 10 nm NPs displays a red color and actually absorb in the green region of the UV-Vis spectrum (λ~520 nm). The unique properties of these nanomaterials have opened many doors for the exploitation of innovative applications towards electronics [12], biology [13], and catalysts [14]. More specifically, these unique optical properties have been exploited in the construction of optical filters, as labels for biomacromolecules [15], for optical switching based on their large, ultrafast nonlinear optical response [16], and for optical trapping (or "tweezers"), based on their high polarizability [11].

Figure 1.2. Gold colloids exhibit different colors in relation to different particle sizes. The larger the NP size, the more red-shifted wavelength it absorbs, and the more blue it appears. (Picture taken from http:// beforeitsnews.com/story /104/900/NanoGold_ Revolution:_Alchemy _of_ the_21st_ Century.html)

1.2.2 Other Metal Nanoparticles

The interest for fabricating other metallic nanoparticles such as cobalt (Co, Figure 1.3), silver (Ag), nickel (Ni), ruthenium (Ru), and copper (Cu) has been driven by the scientific *curiositas* to further investigate the potential novel properties that non-gold containing nanomaterials may also exhibit. Studies on Co NPs, synthesized via different methodologies, for example, have been driven by the necessity for enhancing magnetic information storage as well as catalysis. More recently scientists at the National Institute of Standards and Technology (NIST) have shown that varying the shape of cobalt nanoparticles from spherical to cubic can result in a basic alteration of the magnetic properties [17]. Another unique property that a colloidal solution of magnetic Co NPs display is that they spontaneously assemble into well-

ordered two-dimensional lattices, three-dimensional superlattices and micron-sized rings when deposited onto a substrate upon slow evaporation of the solvent [17].

In addition many studies have investigated and reported the antibacterial properties of silver nanocolloids, e.g. the company Samsung launched the Silver Nano Health System trademark in 2003. The inner walls of their appliances such as refrigerators and air conditioners can be covered with nano silver coatings since the silver ions inhibit growth of airborne bacteria by suppressing the respiration [18]. Overall, metallic NPs have been synthesized for copious applications: from antibacterial agents [18], to drug delivery systems [19], as well as for biosensors [20] to bioimaging [21]. Many companies and laboratories have approached NP synthesis utilizing several methodologies, which as illustrated in section 1.3, despite the "monodispersity" and relatively good yields achieved, still present a number of drawbacks including lack of "green" pathways, gradual size tunability, and ultimate size and morphology control.

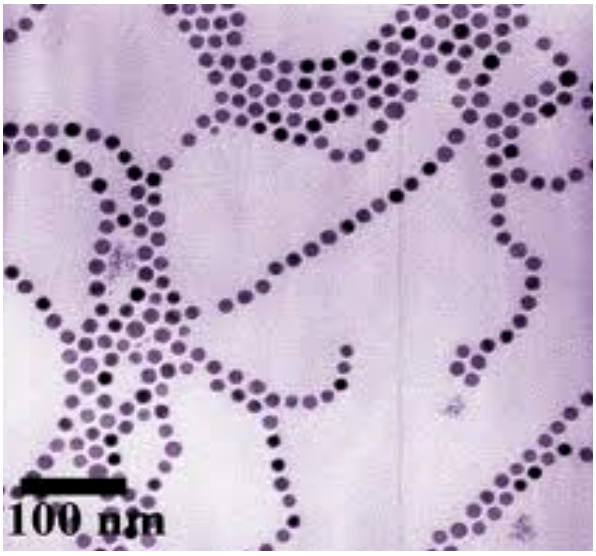

Figure 1.3. TEM image of cobalt nanoparticles [22]

1.2.3 Metal Oxide Nanoparticles

Metal oxide nanoparticles are also attractive for a variety of applications including catalysis, sensors, opto-electronic materials, and environmental remediation [23, 24]. In the same fashion as the metallic nanoparticles, a controlled synthesis of metal oxide nanoparticles is necessary for efficient applications. Solution-phase methods offer large degree of control over the synthesized products [25]. There are two main classes of applications of metal oxide nanoparticles: high surface area materials and materials taking advantage of the size-dependence of physical properties. For example, materials for super-capacitors rely on the large surface area per weight or film thickness for their function. This is a structural consideration and is not related to unique size dependent physical properties. On the other hand, attempts to apply ZnO nanoparticles in tunable light emitting devices are based on the size dependence of the luminescence wavelength. Catalysis applications are an example where both the high surface area and size-dependent properties play a role. The surface energy is expected to depend on the particle size, and hence, the catalytic activity may be enhanced due to a change of the surface physical properties with size. Similar arguments hold for high surface area sensors, and more research is needed on the elucidation of mechanisms in such applications. In the fabrication of high surface area materials, the controlled synthesis of nanoparticles with a relatively small size distribution has several advantages including better control over film deposition and film properties. For example, thin, porous films of TiO_2 nanoparticles are transparent to visible light, whereas the use of commercial nanopowders results in white, opaque films. Similar properties for ZnO films is being applied in the fabrication of sun block cream; using ZnO nanoparticles fabricated in a controlled way (although not quantum-sized), the cream is transparent instead of the white paste that results from using micron-sized ZnO particles.

Zinc oxide may be found in many different products, including: zinc oxide ointment, skin lotions, sunscreen lotion, cosmetics, paint, rubber goods, and paper coating. One of the reasons why ZnO has been used for decades in many cosmetic products and in sun-block creams is related to its capability of absorbing in the UV light region (λ =360nm). ZnO nanoparticles have been investigated recently for three main applications: fungicide [26], solar energy [27] and electronics [28]. The doping with aluminum, copper, or tin is essential for these nanostructures to absorb more in the red region of the visible spectrum.

Cobalt oxide (Co_3O_4) nanoparticles have shown magnetism and been used for catalytic purposes [29]. Cobalt catalysts have been fabricated recently by Nocera to mimic the MgO core in the leaves responsible of photosynthesis and capable of splitting water into H_2 and O_2 [30]

1.3 Current Methodologies of NP Synthesis

In order to synthesize NPs or nanostructures and concomitantly aim to optimize yields, to narrow dispersity, obtain shape control, and size tunability, many methods have been developed including: gas phase synthesis [31], laser ablation, and solution phase (e.g. seed mediated [32], sonication-assisted [33], and sonochemical [34]). Most of the current methodologies are time consuming and employ harsh conditions even for the micro scale syntheses (Tables 1 and 2). The former two synthetic approaches are energy intensive since they employ relatively high temperatures and low pressures (>200^{o}C, and <<1atm). Several methodologies make use of organic solvents or organic-aqueous mixed solvents, often at high temperatures, which are also not ideal for scale-up procedures because of chemical wastes. The solution phase synthesis facilitates milder synthetic routes. For example, some original protocols, such as the Turkevich [35] and the Brust-Schiffrin [36], have utilized greener approaches by employing aqueous

solutions of predominantly inorganic precursors, e.g. hydrogen tetrachloroaurate, and/or aqueous-organic solvent mixtures. These methods guarantee a fair yield (>60%), a narrow dispersity (particle size is within 5% of standard deviation), discrete shape control (the morphology is nearly homogeneous), but not a great degree of size tunability. In addition to that, these milder synthetic routes present problems associated with the disproportionation of cationic gold in solution (e.g. $3Au^{+} \rightarrow Au^{3+} + Au^{o}$, [37], Figure 1.4).

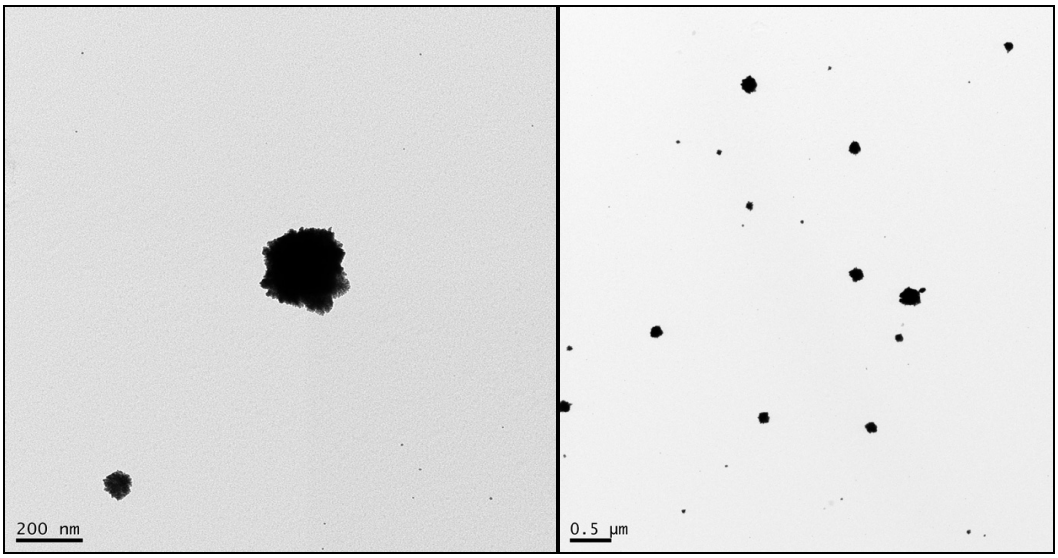

Figure 1.4. TEM image of gold nanoparticles formed by the disproportionation of gold in an aqueous solution of hydrogen tetrachloroaurate indicates that preparations using this solution may be 'contaminated' with NP arising from the starting material rather than the specific procedure reported.

The lack of cheap, fast, and environmentally friendly methodologies issues drove our focus on the development of a greener biologically-based approach to metal NP synthesis. Furthermore most of the present methods do not show versatility in terms of size and material. Here it will be shown how very similar methodologies to nanomaterials synthesis can yield metal NPs as well as metal oxide NPs, and can be easily modified to scale up the NP fabrication (Figure 1.5)

1.4 "Greener" Synthetic Methodologies

The need to use biological entities such as viruses [38] and/or biomolecules such as proteins [39] [40], single stranded RNA [41], or linear segments of DNA [42] [43] to template nanomaterials has been dictated mostly by environmental issues since these potential platforms are stable in water and/or buffer solutions at mildly basic pH values (7.4-8.2), and are biodegradable. These entities may also constitute relatively stiff templates; e.g. viruses' cavity only consisting of a capsid envelop [44] and inner diameters of toroidal topologies of plasmid DNA [45].

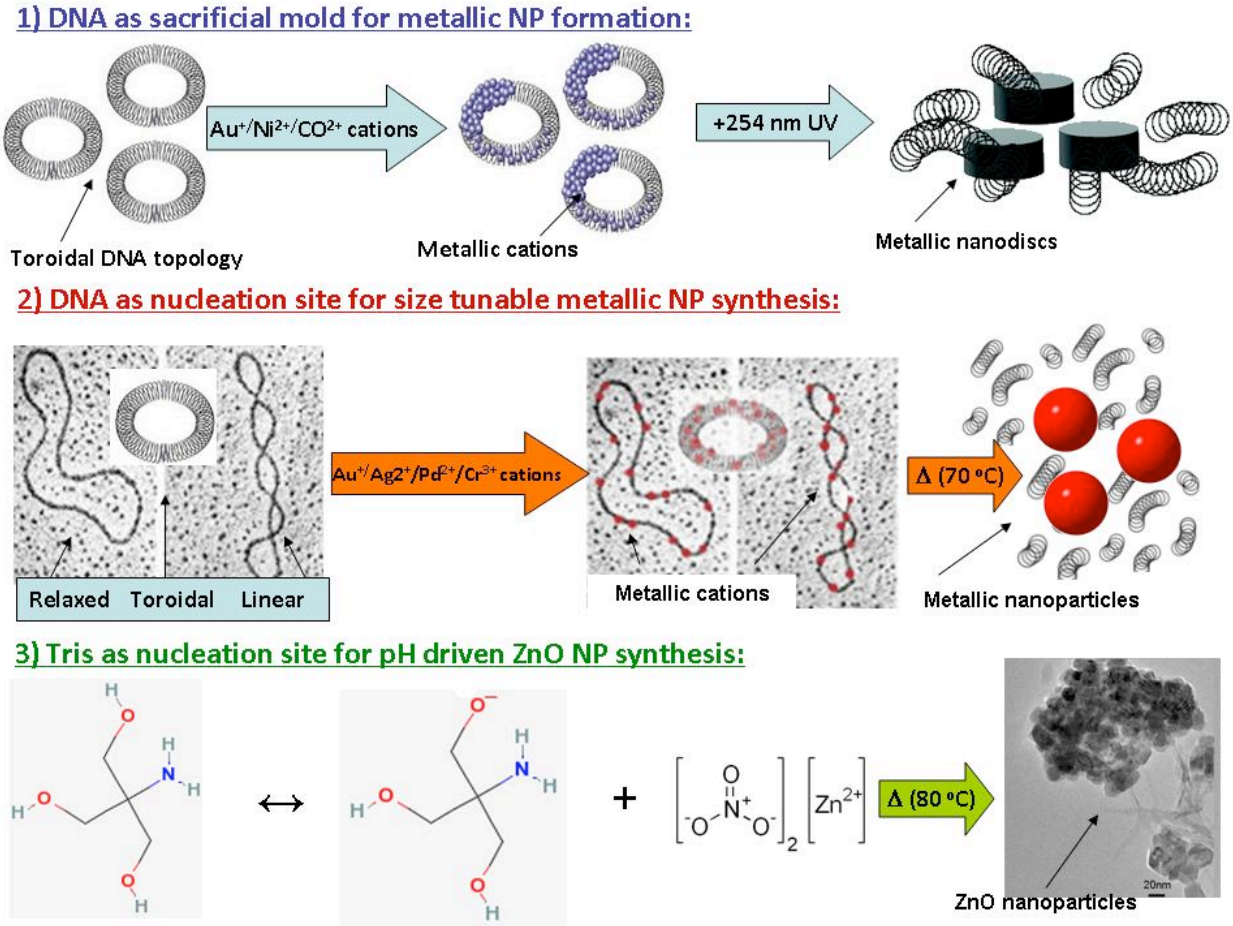

Figure 1.5. Scheme of the three versatile synthetic approaches we use to yield metallic NPs as well as metal oxide NPs in water below 80°C. Since other buffers do not work in this method, the chelating effect of the Tris may play an important role in the ZnO NP formation.

Synthesis	*Overview*	*Reagents/Machines*	*Morphology of NPs*
Turkevich Method [34]	Using $HAuCl_4$ and a reducing agent, heating and boiling cause the gold to disperse into NPs	$HAuCl_4$, 1% trisodium citrate dehydrate as reducing agent (it also prevents aggregation). Heat source	Spherical shaped NPs, 10-20nm diameter
Brust Method [35]	Similar to the Turkevich method, $HAuCl_4$ is reduced and mono-dispersed NP are yielded. However, this process allows NPs to be made in organic liquids that are not miscible with water	$HAuCl_4$ tetraoctyl-ammonium bromide (TOAB, phase transfer catalyst), toluene, $NaBH_4$ (reducing agent) H_2SO_4, (separates organic/ aqueous layer)	Spherical shaped, approx. 5-6nm in diameter. To ensure narrow-dispersity, stir the solution for up to 24 hours
Electro-chemical Synthesis [46]	Gold nanorods are synthesized via redox reaction using a gold plate as the cathode and a platinum plate as the anode. Both electrodes are immersed in cationic surfactants	Metallic gold, metallic platinum, C_{16}TAB (hexadecyl-trimethylammonium bromide, surfactant). Process done under ultrasonication, typically at ~38°C	Nanorods, approx. length: 50-100nm
AuNP synthesis in graft copoly-mer micelles [47]	Using an amphiphilic copolymer of poly acrylic acid and polystyrene, one can introduce gold (III) chloride and reduce the product in UV to synthesize Au NPs	(poly)acrylic acid/polystyrene copolymer, $HAuCl_4$, (either powder or dissolved in Ether), UV radiation. Copolymerization itself takes several other chemical components, like THF and AIBN	Spherical shaped NPs, approximately 5-6 nm
Amine stabilized synthesis of gold NPs [48]	Gold NPs could be prepared by using amine chemistry and surface modification: alkylamine is the reducing agent. This is a one-pot process	Aminophenoxyethyl ether, oleyl amine, $AuCl_3$ in water	Spherical shaped NPs, approximately 10nm in diameter
Wet chemical synthesis [49]	Gold nanorods of various aspect ratios are synthesized using a seeding technique, where $HAuCl_4$ is reduced using $NaBH_4$, and is treated with various chemicals and number of seeds	Reagents and Materials used depend largely on the aspect ratio of the rod. All use $HAuCl_4$, CTAB and ascorbic acid; the aspect of the rod depended on the compositions of the reactants.	Length of the nanorods varied between 5-20nm, depending on the process it underwent, from a few hours to a full day
Synthesis of Au NPs using TiO_2 support [50]	NaOH is used as a precipitating agent to synthesize Au NPs using TiO_2 as a catalyst	NaOH, TiO_2, $HAuCl_4$) air liquid, centrifuge, Titania Degussa P25	NPs are extremely small, averaging about 2nm. NPs do not display specific structures
AuNPs on toroi-dal DNA with calf thymus [51]	Calf thymus DNA serves as a type of biotemplate to help reduce and bond Gold NPs to its toroidal surface	Bis(ethylenediamine)gold(III)chloride, calf thymus DNA, polyvinylpyrrolidone (PVP) , $HAuCl_4$, uranyl acetate (to prepare the DNA toroids)	NP aggregates, with sizes from 25 to 100nm. No definitive shape either
AuNPs synthesis using a viral template [52]	Viral templates are exploited to direct NP syntheses. This template is prepared and reacted with many organometallic compounds, $HAuCl_4$	Various structures of CCMV plasmid and HRE plasmid, ascorbic acid/EDTA buffer, SubE yeast, $HAuCl_4$, RNA	In CCMV: NPs with size from about 7 to 12 nm, In HRE: NPs with size from 4 to 7 nm
Size controlled synthesis of Au NPs using seed cells [53]	Nanoparticles of varying sizes prepared using smaller "seed" cells with UV irradiation, then planting larger gold particles to form Au^{3+} ions, which are reduced into neutral NPs	Germicidal lamp, $HAuCl_4$. The entirety of the reaction takes place under UV radiation with prepared gold embedded on more gold	The shapes of the results were all spherical with size depend-ing on the ratio $Au^{3+}$to Au^0

Table 1.1. Various syntheses of colloidal gold/gold nanoparticles using unstable precursors and/or templating agents which guarantee neither narrow size NP distribution nor size tuning.

Name of Synthesis	*Overview of Synthesis*	*Reagents/Materials*	*Temperature Conditions*	*NP Size & Morphology*
Vapor transport synthesis [54]	Zinc and oxygen are heated at high temperatures and react. The direct method has them react together; indirect methods involve the use of an organometallic catalyst or other intermediates	In a direct process, Zn (which is decomposed from zincite) and oxygen and extreme temperatures are needed. In indirect processes, organo-matallic catalysts such as diethyl zinc are used under an N_2O flow	Dependent on how the process was done; direct methods require higher temperatures (~1400°C); indirect methods often have lower maximum temperatures and slower heating rates (~400-700°C)	Dependent on the process style. Most of the ZnO in the world is synthesized in this way
Micro Emulsion Mediated Synthesis [55]	Reagents of various oil/water/surfactant phases are mixed and the product is calcinated into ZnO	Cetyl trimethyl ammonium bromide (CTAB), ammonium carbonate, zinc nitrate, n-octane, and 1-butanol	For ZnO calcination, temperatures of ~220-250°C is optimal	5-40 nm, Discs, polycrystalline
Biomorphic synthesis [56]	Eggshell membrane is immersed in $Zn(NO_3)_2$/EtOH solution for several hours and then dried and calcinated	Eggshell membrane (ESM), Zinc Nitrate/Ethanol solution	Calcination of the dried ESM/ZnO Hybrids take place anywhere from 300-700°C	Approx 1-1.5 μm, nanofibers
Microwave assisted synthesis using imidazolium salt [57]	Zinc nitrate in excess NaOH solution is combined with an ionic liquid and placed in a microwave, making ZnO NPs within 5 to 10 minutes	Zinc nitrate hexahydrate, excess. NaOH, $[BMIM]BF_4$. Microwave emitter (2.54 GHz)	Reaction conditions usually take place at around 50-130°C	Dependent on the composition of the mixtures; most products take a flower-like or needle-like NP shape

Table 1.2. Various syntheses of zinc oxide nanoparticles using high temperatures and pressures and non-exclusive aqueous precursors

1.5 Hypotheses

Since there is a significant demand for the production of metallic, metal oxide, and hybrid nanoparticles (NPs) for a diverse array of applications, many requiring specific particle sizes and morphologies, there is a need for general synthetic strategies that mitigate the environmental impact of these manufacturing processes, i.e. greener syntheses. Greener methods are aimed at eliminating organic solvents, reducing energy costs, and strive to increase yields. The overall

goals of the work described herein are to develop greener methods to produce metallic and metal oxide NPs, while controlling of particle size and dispersity.

The hypotheses are:

(1) Significantly slowing down the rate of reduction of DNA-bound metal cations will allow better control of the size of metallic NPs from the corresponding salts.

(2) Plasmid DNA can be used as an inexpensive mold or template for NPs formation.

(3) Plasmid DNA can be used as a nanoreactor as well as a source of electrons using a kinetically driven synthetic approach.

(4) The known pH dependence of tris(hydroxymethyl)aminomethane (Tris buffer) and the known olation chemistry of zinc salts can be controlled to make ZnO NP at relatively lower temperatures.

Hypotheses 1 and 2 are interconnected and are therefore discussed together below and in Chapters 3 and 4.

1.5.1 Hypothesis 1. Significantly slowing down the rate of reduction of DNA-bound metal cations will allow better control of the size of metallic NPs from the corresponding salts.

1.5.2 Hypothesis 2. Plasmid DNA can be used as an inexpensive mold or template for NPs formation. Plasmid DNA is a circular segment of DNA capable of self-replicating in bacterial hosts, and can exist in many topologies, including relaxed, circular, linear supercoiled, supercoiled, and toroidal (see Figure 1.5) [58]. Factors contributing to this topological arrangement in suspension are: ionic strength, buffer, temperature, and G-C content [59]. Plasmids are the basis of many industrial biotechnology processes and can be produced on

kilogram scales [60]. The size of a plasmid can be controlled by varying the number of base pairs it contains, thus providing a way to modify the size of this template/mold.

Chapter 3 describes the use of the toroidal form of plasmid DNA as a rigid, narrowly dispersed bio-polymeric nanocavity, which molds the formation of disc-shaped nanoparticles of three types of metals, namely Au, Ni, and Co. This approach exploits several properties of plasmid DNA: (a) DNA affinity for metal cations, (b) toroidal plasmid DNA structures, which are favored by metal ionic binding, (c) the redox chemistry of DNA-bound metal cations upon UV irradiation at $\lambda = 254$ nm, and (d) the ease of varying plasmid DNA size.

In this method, UV light is used to photo-initiate electron transfer from the DNA to the metal ions thereby exploiting well-known photo-driven oxidation of DNA in the presence of electron acceptors and other oxidants [61, 62], in this case metal ions [63, see also Figure 1.6]. The key feature is that the reducing equivalents are delivered slowly over a prolonged period of time (>1 hour). UV irradiation ($\lambda = 254$ nm) of the reaction mixture causes a photo-induced electron transfer from the plasmid to the metal ion. The mechanisms of photo-driven DNA oxidation chemistry, including long-range electron transport in DNA, are complex and include radical ions on the bases, oxidation of the sugars, and reactive oxygen species [64, 65, see Figure 1.7]. Nonetheless, prolonged irradiation of the plasmid DNA in the presence of Au(I), Ni(II), and Co(II), and with 254 nm light results in extensive degradation of the DNA and formation of the corresponding metallic NP [63, 66]. Figure 1.8 shows the structures of a guanine positive radical after UV light has triggered an electron loss and the potential side reactions that result in DNA degradation (the reduction potentials at pH 7 are shown in table 1.3). The toroidal topology of DNA has been recently investigated [67] and the redox chemistry, which is responsible for metal bound cations reduction, is also discussed [63].

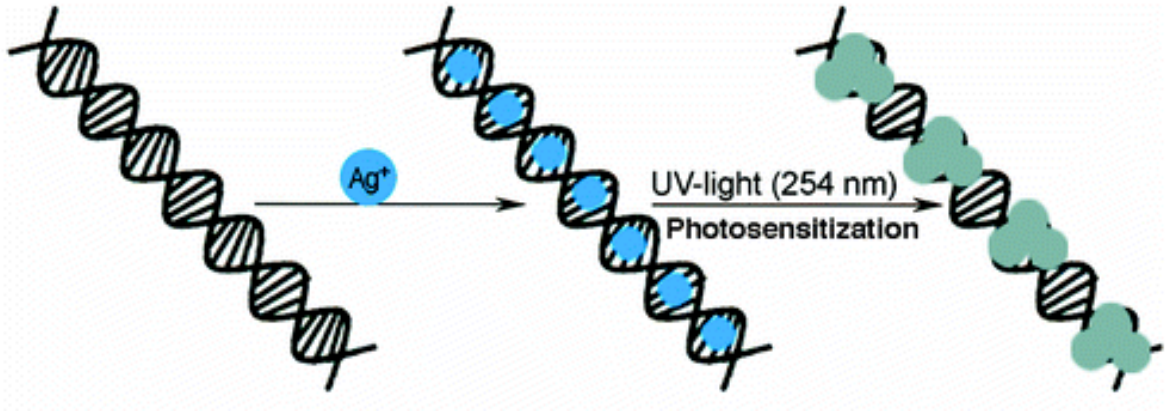

Figure 1.6. A previous report on the formation of Ag NP [63]. Ag^+ cations, incubated with the DNA suspension, first bind to the DNA strands which act as nanoreactors. When irradiated with UV light, photooxidation of DNA bases takes place providing electrons for the reduction of the silver cations to metallic NPs.

Base pair	Redox potentials at pH 7 (V)
(dG(-H)•/dG)	1.29
(dA(-H)•/dA)	1.42
(dT(-H)•/dT)	1.7
(dC(-H)•/dC)	1.6

Table 1.3. The reduction potentials at pH 7 (i.e., midpoint potentials (E7)) of the DNA components at room temperature in aqueous solutions [68].

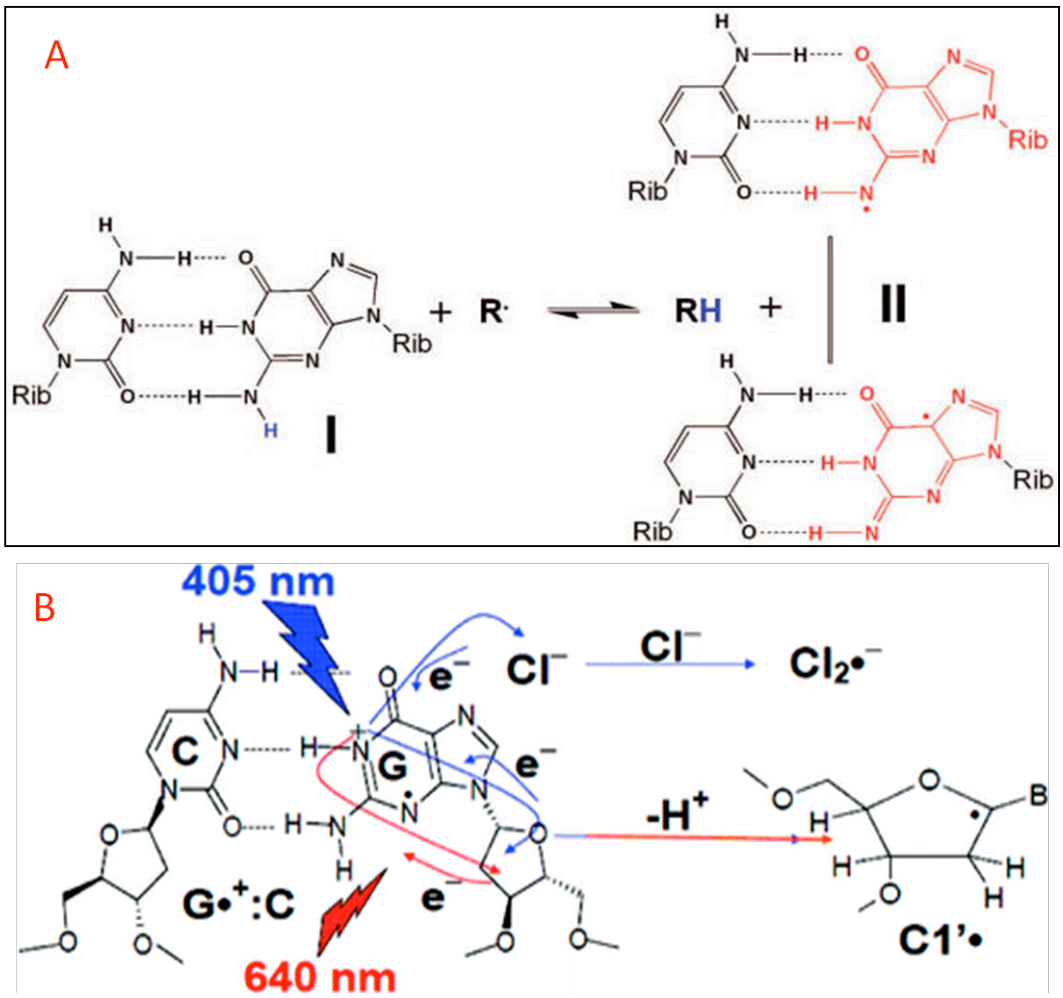

Figure 1.7. (A) Proposed radical pathway and redox equilibrium for the reaction upon interaction with benzotrianzyl radicals. (B) Photoinduced transfer of an electron from cytosine-guanine H-bonded radical cation to either a reactive anion or a sugar moiety

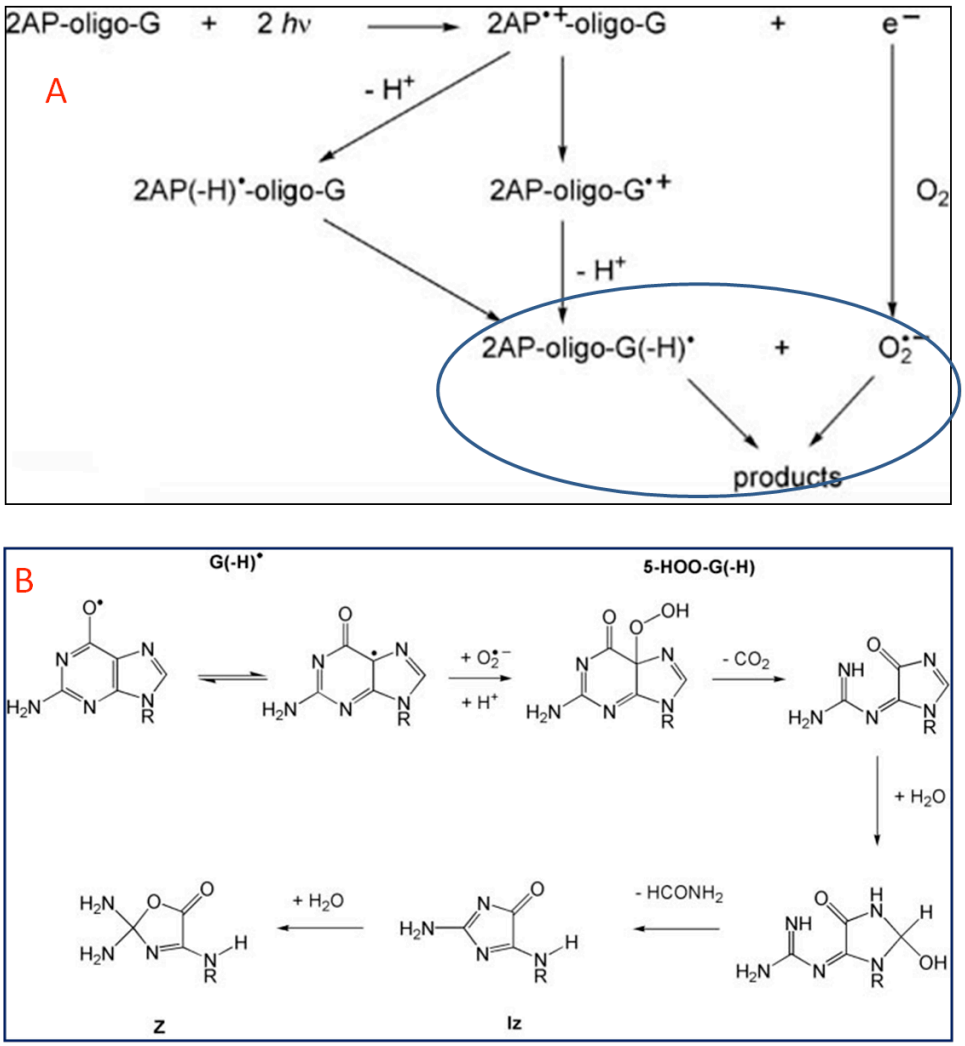

Figure 1.8. (A) Formation of the adduct 8-hydroxideoxyguanosine upon ultraviolet B radiation (UVB) which induces oxidative damage in DNA with consequent degradation products (B).

1.5.3 Hypothesis 3. Plasmid DNA can be used as a nanoreactor as well as a source of electrons using a kinetically driven synthetic approach.

A complementary synthetic method, to the one developed in hypothesis 2, is based on a kinetic rather than photo-oxidative approach, by careful control of the temperature and the duration of the reaction. Here therefore the plasmid or other duplex DNA acts as a nucleation site to initiate and control the formation of Au and other metallic NPs (this approach is sometimes referred to as a templating). The need to simplify the original methodology by disposing of the

UV-light as a reducing photoinitiator is dictated by the diminished reproducibility of the results using small lab UV lamps.

In this case the DNA does not act as a mold, but controls nucleation and inhibits aggregation of the NP. Also, this thermally-driven reaction exploits the well-established oxidation chemistry of alcohols and amines, in this case the Tris buffer and/or the EDTA.

1.5.4 Hypothesis 4. The known pH dependence of Tris buffer and the known olation chemistry of zinc salts can be controlled to make ZnO NP at relatively lower temperatures.

Also reported herein is a simple, scalable hydrothermal method to make ZnO NPs that exploits temperature to precisely control the range of pH values of an organic amine buffer, and control the kinetics of the formation of size controlled NPs with narrow dispersity. The presence or absence of ethylenediaminetetraacetic acid (EDTA) in the buffer solution, further modulates the morphology of the ZnO nanomaterials since both compounds can serve as nucleating sites, chelators, and as stabilizing agents that prevents agglomeration. Though the formation of ZnO and similar oxides under basic conditions is well studied, the role of the Tris buffer in the present system must go beyond pH control since other buffers such as phosphate do not work.

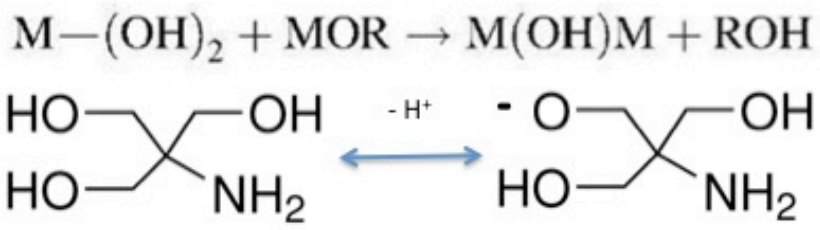

Figure 1.9. (Top) Representation of a typical olation reaction that occurs in aqueous solutions containing metal salts upon hydration. (Bottom) Tris buffer at relatively elevated temperature causes a change in pH value in aqueous solutions.

1.6 Current Characterization Methods of Nanomaterials

The current most common methodologies to characterize nanomaterials are: Transmission Electron Microscopy (TEM), Electron Diffraction (ED), X-Ray Diffraction (XRD), Energy Dispersive X-ray Spectrometry (EDS), Scanning Electron Microscopy (SEM), Atomic Force Microscopy (AFM), and Dynamic Light Scattering (DLS). In Chapter 2 it will be shown how, using two of these techniques, NPs were characterized and the results achieved.

1.6.1 TEM

The TEM uses a series of magnetic lenses to focus the electron beam that comes from the source; Tungsten (W), Lanthanum Hexaboride (LaB6), field emission (FEG). The beam is accelerated by a high potential through the specimen in vacuum. The lenses above the specimen, known as the illumination system, focus the electrons onto the specimen. The electrons pass through the specimen and these transmitted electrons are focused by lenses below the specimen known as the magnification system. An image is produced in the image plane of the objective lens and a diffraction pattern is formed in the back focal plane of the objective lens. One obtains an image or a diffraction pattern depending onto which of these two planes the lower magnification lenses are focused.

1.6.2 Diffraction Principles

Crystalline materials have a regular array of atoms. These atoms form planes that have various orientations to specific crystal axes and distances between them known as interplanar spacings. Scattered and diffracted rays contribute to a diffraction pattern (DP). Those rays coming from a non-specific plane are known as scattered rays. Those that follow Bragg's

Law, $n\lambda = 2d \sin\theta$, in which a diffracted beam arises from specific crystal plane, are known as diffracted beams.

Bragg equation $n\lambda = 2d \sin\theta$

n = integer

λ = wavelength

d = interplanar spacings in angstroms

θ = Bragg angle

1.6.3 XRD

1.6.3.1 Instrumentation

X-rays are the source for the two types of XRD instruments used in X-ray powder diffraction: film camera and diffractometers.

Film camera: The Debye-Scherrer camera is used for X-ray powder diffraction. The film in a light-tight container is exposed to the reflected X-rays from the planes of the crystal. This is the method to use when one has only a very small sample.

A diffractometer: This is a mechanical goniometer where the sample turns at angle θ and the detector moves at twice the angle to intercept the diffracted beam of X-rays. Data are read out as 2θ vs the intensity of the X-rays. This 2θ can be converted to d-spacings by the Bragg equation, which can be written as $1/d \alpha \sin\theta$ or $d = n\lambda / \sin 2\theta$

1.6.3.2 Advantages of XRD

It can be used to identify a compound, it can be used to identify polymorphs of various types, it is non-destructive and it requires a relatively small sample. (A larger sample than required for ED though).

1.6.4 EDS

When an electron beam impinges upon a specimen it transfers part of its energy to the specimen causing a rearrangement of the orbital electrons. When an electron is ejected, a vacancy occurs in one of the shells, causing an unstable state. An electron from an outer shell, having a higher energy, fills the vacancy in an inner shell. The difference in energy released produces characteristic x-rays. The electron energy levels of the atomic shells are distinctive for each element.

Bremsstrahlung: Continuum x-ray radiation caused by the deceleration of electrons in the specimen. (This is the background in an EDS spectrum).

Characteristic x-rays: Each element has a unique way of filling vacancies in shells. The specific electron that fills the vacancy depends on the atomic number of the element. This means that each element will generate a distinct, unique series of peaks, known as a spectrum, as follows:

K_α radiation: a vacancy in a K shell is filled by an electron from the L shell.

K_β radiation: a vacancy in a K shell is filled by an electron from the M shell.

L_α radiation: a vacancy in an L shell is filled by an electron from the M shell.

L_β radiation: a vacancy in an L shell is filled by an electron from the N shell.

M_α radiation: a vacancy in the M shell is filled by an electron from the N shell.

Elements with lower atomic numbers have simple spectra, whereas those with higher atomic numbers will have more complex spectra. For example: **Ca:** has only a K_a and a K_β line and **Cu:** has a K_a and a K_β and an L line. Elements such as C, O, Na, Mg, Al, Si, P have only one line (K_a)

1.6.5 SEM

Generally the SEM is used to study surface morphology and samples that are too large for the TEM. The accelerating voltages are usually lower than in a TEM. Instead of the stationary beam used in TEM, in SEM the beam is scanned over the specimen. A SEM image is usually formed by secondary (SE) or backscattered (BS) electrons reflected from the specimen.

1.6.6 AFM

AFM provides a 3D profile of the surface on a nanoscale, by measuring *forces* between a sharp probe (<10 nm) and surface at very short distance (0.2-10 nm probe-sample separation). The probe is supported on a flexible cantilever. The AFM tip "gently" touches the surface (in contact mode) and records the small force between the probe and the surface. Alternatively, the constant force mode is a non-contact method. The probe is placed on the end with a give spring constant). The amount of force between the probe and the surface is dependent on the *spring constant* (stiffness of the cantilever) and the distance between the probe and the sample surface. This force can be described using Hooke's Law:

$$F = -k\ x$$

F = force; K = spring constant; x = cantilever deflection

If the spring constant of cantilever (typically between 0.1 to 1 nN/nm) is less than surface, the cantilever bends and the deflection is monitored.

1.6.7. DLS

Dynamic Light Scattering is also known as Photon Correlation Spectroscopy. This technique is a rapid method to determine the size of particles. Shining a monochromatic light beam, such as a laser, onto a solution with spherical particles in Brownian motion causes a Doppler shift when the light hits the moving particle, changing the wavelength of the incoming light. This change is related to the size of the particle. It is possible to compute the sphere size distribution and give a description of the particle's motion in the medium, measuring the diffusion coefficient of the particle and using the autocorrelation function and the Einstein-Stokes equations. This method has several advantages: first of all the experiment duration is short and it is almost all automatized and an extensive experience is not required. Moreover, this method has modest development costs.

1.7 References

1. Kelly, K.L., et al., *The Optical Properties of Metal Nanoparticles: The Influence of Size, Shape, and Dielectric Environment.* J. Phys. Chem. B, 2002. **107**(3): p. 668-677.
2. Alvarez, M.M., et al., *Optical Absorption Spectra of Nanocrystal Gold Molecules.* J. Phys. Chem. B, 1997. **101**(19): p. 3706-3712.
3. Tian, Y. and C. Mao, *Molecular Gears: A Pair of DNA Circles Continuously Rolls against Each Other.* J. Am. Chem. Soc., 2004. **126**(37): p. 11410-11411.
4. Deng, J. and et al., *Fabrication and manipulation of solid-state SiO 2 nano-gears on a gold surface.* Nanotechnology, 2011. **22**(27): p. 275307.
5. Yezhelyev, M.V., et al., *Emerging use of nanoparticles in diagnosis and treatment of breast cancer.* Lancet Oncol., 2006. **7**(8): p. 657-667.
6. Service, R.F., *Nanoparticle Trojan Horses Gallop From the Lab Into the Clinic.* Science, 2010. **330**(6002): p. 314-315.
7. Minnich, A.J., et al., *Bulk nanostructured thermoelectric materials: current research and future prospects.* Energy Environ. Sci., 2009. **2**(5): p. 466-479.
8. Cavalcanti, A.a.R.A.F., Jr., *Nanorobotics Control Design: A collective Behavior Approach for Medicine.* IEEE Trans. Nanobio., 2005. **Vol. 4**(No. 2 June 2005): p. 133-140.
9. Balas, F., et al., *Reported nanosafety practices in research laboratories worldwide.* Nature Nanotech., 2010. **5**(2): p. 93-96.
10. Daniel, M.-C. and D. Astruc, *Gold Nanoparticles: Assembly, Supramolecular Chemistry, Quantum-Size-Related Properties, and Applications toward Biology, Catalysis, and Nanotechnology.* Chem. Rev., 2003. **104**(1): p. 293-346.
11. Rechberger, W., et al., *Optical properties of two interacting gold nanoparticles.* Opt. Commun., 2003. **220**(1-3): p. 137-141.
12. Collins, P.G., M.S. Arnold, and P. Avouris, *Engineering Carbon Nanotubes and Nanotube Circuits Using Electrical Breakdown.* Science, 2001. **292**(5517): p. 706-709.
13. Craighead, H.G., *Nanostructure science and technology: Impact and prospects for biology.* J. Vac. Sci. Technol. A 2003. **21**(5): p. S216-S221.
14. Zeng, T., et al., *Fe_3O_4 nanoparticles: a robust and magnetically recoverable catalyst for three-component coupling of aldehyde, alkyne and amine.* Green Chem., 2010. **12**(4): p. 570-573.
15. Stracke, F., I. Rieman, and K. König, *Optical nanoinjection of macromolecules into vital cells.* J. Photochem. Photobiol., B, 2005. **81**(3): p. 136-142.
16. Zheludev, N.I., *Single nanoparticle as photonic switch and optical memory element.* J. Optic. Pure. Appl. Optic., 2006. **8**(4): p. S1.
17. Cheng, G., R.D. Shull, and A.R. Hight Walker, *Dipolar chains formed by chemically synthesized cobalt nanocubes.* J. Magn. Magn. Mater., 2009. **321**(10): p. 1351-1355.
18. Baker C, P.A., Pakstis L, Pochan DJ, Shah SI., *Synthesis and Antibacterial Properties of Silver Nanoparticles.* J. Nanosci. Nanotechnol., 2005. **5**: p. 244-249.
19. Vivero-Escoto, J.L., et al., *Mesoporous Silica Nanoparticles for Intracellular Controlled Drug Delivery.* Small, 2010. **6**(18): p. 1952-1967.

20. Wu, S., et al., *Electrodeposition of silver-DNA hybrid nanoparticles for electrochemical sensing of hydrogen peroxide and glucose.* Electrochem. Commun., 2006. **8**(8): p. 1197-1203.
21. Zhang, J., et al., *One-pot synthesis and characterization of rhodamine derivative-loaded magnetic core–shell nanoparticles.* J. Nanopart. Res., 2011. **13**(5): p. 1909-1916.
22. Cheng, G., et al., *Magnetic-Field-Induced Assemblies of Cobalt Nanoparticles.* Langmuir, 2005. **21**(26): p. 12055-12059.
23. Michael R. Hoffmann, S.T.M., Wonyong Choi, and Detlef W. Bahnemannt, *Environmental Applications of Semiconductor Photocatalysis.* Chem. Rev., 1995. **95**: p. 69-96.
24. Kamat, P.V., *Photochemistry on nonreactive and reactive (semiconductor) surfaces.* Chem. Rev., 1993. **93**(1): p. 267-300.
25. Jolivet, J.-P., *Metal Oxide Chemistry and Synthesis - From Solution to Solid State*2003, Chichester: John Wiley & Sons.
26. He, L., et al., *Antifungal activity of zinc oxide nanoparticles against Botrytis cinerea and Penicillium expansum.* Microbiol. Res., 2011. **166**(3): p. 207-215.
27. Saito, M. and S. Fujihara, *Large photocurrent generation in dye-sensitized ZnO solar cells.* Energy Environ. Sci., 2008. **1**(2): p. 280-283.
28. Ko, S.H., et al., *ZnO nanowire network transistor fabrication on a polymer substrate by low-temperature, all-inorganic nanoparticle solution process.* Appl. Phys. Lett., 2008. **92**(15): p. 154102.
29. Tang, Q., et al., *Characterizations of Cobalt Oxide Nanoparticles within Faujasite Zeolites and the Formation of Metallic Cobalt.* Chem. Mater., 2004. **16**(10): p. 1967-1976.
30. Kanan, M.W. and D.G. Nocera, *In Situ Formation of an Oxygen-Evolving Catalyst in Neutral Water Containing Phosphate and Co2+.* Science, 2008. **321**(5892): p. 1072-1075.
31. Cross, C.E., J.C. Hemminger, and R.M. Penner, *Physical Vapor Deposition of One-Dimensional Nanoparticle Arrays on Graphite: Seeding the Electrodeposition of Gold Nanowires.* Langmuir, 2007. **23**(20): p. 10372-10379.
32. Liu, J., et al., *Precise Seed-Mediated Growth and Size-Controlled Synthesis of Palladium Nanoparticles Using a Green Chemistry Approach.* Langmuir, 2009. **25**(12): p. 7116-7128.
33. Lei, Z., L. Zhang, and X. Wei, *One-step synthesis of silver nanoparticles by sonication or heating using amphiphilic block copolymer as templates.* J. Colloid Interface Sci., 2008. **324**(1-2): p. 216-219.
34. Kumar, P.S.S., et al., *Sonochemical synthesis and characterization of gold-ruthenium bimetallic nanoparticles.* Colloid Surface A, 2010. **356**(1-3): p. 140-144.
35. Kimling, J., et al., *Turkevich Method for Gold Nanoparticle Synthesis Revisited.* J. Phys. Chem. B, 2006. **110**(32): p. 15700-15707.
36. Goulet, P.J.G. and R.B. Lennox, *New Insights into Brust−Schiffrin Metal Nanoparticle Synthesis.* J. Am. Chem. Soc., 2010. **132**(28): p. 9582-9584.
37. Barakat, K.A., et al., *Disproportionation of Gold(II) Complexes. A Density Functional Study of Ligand and Solvent Effects.* J. Phys. Chem. B, 2006. **110**(30): p. 14645-14651.
38. Aljabali, A.A.A., et al., *Virus templated metallic nanoparticles.* Nanoscale, 2010. **2**(12): p. 2596-2600.

39. Asuri, P., et al., *The protein-nanomaterial interface.* Curr. Opin. Biotechnol., 2006. **17**(6): p. 562-568.
40. Kane, R.S. and A.D. Stroock, *Nanobiotechnology: Protein-Nanomaterial Interactions.* Biotechnol. Progr., 2007. **23**(2): p. 316-319.
41. Kumar, A. and A. Jakhmola, *RNA-Mediated Fluorescent Q-PbS Nanoparticles.* Langmuir, 2007. **23**(6): p. 2915-2918.
42. Sun, L., et al., *Fabrication of silver nanoparticles ring templated by plasmid DNA.* Appl. Surf. Sci., 2006. **252**(14): p. 4969-4974.
43. Becerril, H.A. and A.T. Woolley, *DNA-templated nanofabrication.* Chem. Soc. Rev., 2009. **38**(2): p. 329-337.
44. de la Escosura, A., et al., *Viral capsids as templates for the production of monodisperse Prussian blue nanoparticles.* Chem. Commun., 2008(13): p. 1542-1544.
45. Samson, J., et al., *Fabrication of Metal Nanoparticles Using Toroidal Plasmid DNA as a Sacrificial Mold.* ACS Nano, 2009. **3**(2): p. 339-344.
46. Yu, et al., *Gold Nanorods: Electrochemical Synthesis and Optical Properties.* J. Phys. Chem. B, 1997. **101**(34): p. 6661-6664.
47. Carrot, G., et al., *Gold nanoparticle synthesis in graft copolymer micelles.* Colloid Polym. Sci., 1998. **276**(10): p. 853-859.
48. Aslam, M., et al., *Novel one-step synthesis of amine-stabilized aqueous colloidal gold nanoparticles.* J. Mater. Chem., 2004. **14**(12): p. 1795-1797.
49. Jana, N.R., L. Gearheart, and C.J. Murphy, *Wet Chemical Synthesis of High Aspect Ratio Cylindrical Gold Nanorods.* J. Phys. Chem. B, 2001. **105**(19): p. 4065-4067.
50. Zanella, R., et al., *Alternative Methods for the Preparation of Gold Nanoparticles Supported on TiO2.* J. Phys. Chem. B, 2002. **106**(31): p. 7634-7642.
51. Preston, T.C. and R. Signorell, *Formation of Gold Particles on Nanoscale Toroidal DNA Assembled with Bis(ethylenediamine)gold(III).* Langmuir, 2010. **26**(12): p. 10250-10253.
52. Slocik, J.M., et al., *Viral templates for gold nanoparticle synthesis.* J. Mater. Chem., 2005. **15**(7): p. 749-753.
53. Sau, T.K., et al., *Size Controlled Synthesis of Gold Nanoparticles using Photochemically Prepared Seed Particles.* J. Nanopart. Res., 2001. **3**(4): p. 257-261.
54. *Zinc Oxide Nanostructures: Synthesis and Properties.* J. Nanosci. Nanotechno., 2005. **5**: p. 1561-1573.
55. Hingorani, S., et al., *Microemulsion mediated synthesis of zinc oxide nanoparticles for varistors studies*, Mater. Res. Bull., 1993. **28**(12): p. 1303-131.
56. Dong, Q., et al., *Synthesis of biomorphic ZnO interwoven microfibers using eggshell membrane as the biotemplate*, Mater. Lett., 2007. **61**(13): p. 2714-2717.
57. Krishnakuma, T., et al., *Microwave-assisted synthesis and characterization of flower shaped zinc oxide nanostructures*, Mater. Lett., 2009. **63**(2): p. 242-245.
58. Cohen, Stanley N., Chang, Annie C. Y., Boyer, Herbert W., and Robert B. Helling, *Construction of Biologically Functional Bacterial Plasmids In Vitro*. Proc. Natl. Acad. Sci. USA, 1973. **70**(11): p. 3240-3244.
59. Barton, Jacqueline K., Goldberg, Jonathan M., Kumar, Challa V., and Nicholas J. Turro, *Binding Modes and Base Specificity of Tris(phenanthroline)ruthenium(II) Enantiomers with Nucleic Acids: Tuning the Stereoselectivity*. J. Am. Chem. Soc. 1986. **108**: p. 2081-2088.

60. Rosenthal, A., Coutelle, O., and M. Craxton, *Large-scale production of DNA sequencing templates by microtitre format PCR.* Nucleic Acids Res. 1993. **21**(1): p. 173–174.
61. Candeias, L. P. and S. Steenken, *Structure and Acid-Base Properties of One-Electron-Oxidized Deoxyguanosine, Guanosine, and 1 -Met hylguanosine*. J. Am. Chem. Soc. 1989. **111**: p. 1094-1099.
62. Shinde, Sujata S., Maroz, Andrej, Hay, Michael P., and Robert F. Anderson, *One-Electron Reduction Potential of the Neutral Guanyl Radical in the GC Base Pair of Duplex DNA*. J. Am. Chem. Soc. 2009. **131**(14): p. 5203–5207.
63. Berti, Lorenzo, Alessandrini, Andrea, and Paolo Facci, *DNA-Templated Photoinduced Silver Deposition*. J. Am. Chem. Soc. **2005**. **127**(32): p. 11216–11217.
64. Armitage, Bruce, *Photocleavage of Nucleic Acids*. Chem. Rev. 1998. **98**(3): p. 1171–1200.
65. Kawanishi, Shosuke, Hiraku, Yusuke, and Shinji Oikawa, *Mechanism of guanine-specific DNA damage by oxidative stress and its role in carcinogenesis and aging*. Mutation Research. 2001. **488**(1): p.65-76.
66. Khanduri, Deepti, Adhikary, Amitava, and Michael D. Sevilla, *Highly Oxidizing Excited States of One-Electron-Oxidized Guanine in DNA: Wavelength and pH Dependence*. J. Am. Chem. Soc. **2011**. **133**(12): p. 4527–4537.
67. Vilfan, Igor D., Conwell, Christine C., Sarkar, Tumpa, and Nicholas V. Hud, *Time Study of DNA Condensate Morphology: Implications Regarding the Nucleation, Growth, and Equilibrium Populations of Toroids and Rods*. Biochemistry. 2006. **45**(26): p. 8174-8183.
68. Steenken, S.; Jovanovic, S. V. *How Easily Oxidizable Is DNA? One-Electron Reduction Potentials of Adenosine and Guanosine Radicals in Aqueous Solution.* J. Am. Chem. Soc. 1997. **119**: p. 617-618.

Chapter 2

SIMPLIFYING ELECTRON DIFFRACTION PATTERN IDENTIFICATION OF MIXED MATERIAL NANOPARTICLES*

2.1 Introduction

Metallic and non-metallic nanoparticles (NPs), ranging in size from 1-200 nm, have unique functional properties that differ from the bulk materials and the component atoms or molecules [1]. These unique properties have driven the demand for nano-sized materials and new methods to synthesize NPs, which are used in drug delivery systems [2], bio-imaging agents [3], catalysts [4], photonics, and optical devices [5]. Inorganic NPs can be synthesized with a variety of methods that impart size, shape, and other structural properties. Cobalt-based NPs, for instance, display unique size and shape-dependent magnetic properties [6], while the band gap, UV blocking properties, and stability of zinc oxide (ZnO) NPs enable new applications in products ranging from cosmetics [7] to solar cell power [8].

*Part of this work was first presented at the M&M meeting in 2009, other parts at the M&M meeting in 2010. In 2009 *Microscopy Today* requested we add to it for an article, and was published in September. This work was submitted and accepted in the September 2011 issue of *Microscopy Today* with the same title.

Approaches to NP synthesis include solvothermal, biological, and other templates [9], as well as ligands to seed NP growth and molding strategies [10]. Our approach for synthesizing metal NPs involves using toroidal topologies of plasmid DNA as sacrificial molds and varying conditions to fabricate size tunable gold, nickel, and cobalt NPs [9]. Plasmid DNA provides a relatively inexpensive monodispersed template that can be engineered to form in a range of sizes and exploits the well-established high affinity for metal cations. This strategy is generally a greener approach to NP synthesis since the solvent is water and the template is biodegradable.

We have characterized these NPs by atomic force microscopy (AFM) and transmission electron microscopy (TEM). For example, a pcDNA3.1 (+) plasmid can be used as a sacrificial mold to yield disc-shaped gold and nickel NPs in the range of 28±3 nm x 8±1 nm and 52±5 nm x 13±1 nm, respectively. Columnar-shaped ZnO NPs were synthesized using a pH gradient and imaged to reveal a bimodal distribution in the range of 70±10 nm x 50±10 nm and 135±15 nm x 80±10 nm. In order to confirm the nature of these NPs, which were composed of both metals and non-metallic materials, we compared their electron microdiffraction (μD) patterns to known standards [11, 12].

There are two methods for obtaining electron diffraction (ED) patterns [13]. The selected area diffraction (SAD) method uses a diffraction aperture to select the area producing the ED pattern and μD and convergent beam electron diffraction (CBED) techniques use the beam to select the area producing the pattern. The minimum area that can be selected on a 100kV TEM by the SAD method is 1 μ. [12]. Since μD uses the beam to select the area, the minimum size in the TEM mode is limited by the electron source. The finely diffracted beams, as opposed to CBED's discs, are produced by using a small (20-30 μ) second condenser aperture [14]. Since

the size of the NPs that we were looking to produce was less than 200 nm, μD was the method of choice.

Microdiffraction (μD) proved to be a reliable method of verifying the composition of individual NPs when there is not enough sample for x-ray diffraction (XRD) analysis. In the use of plasmid molds, the resulting materials could be the starting metal ion salts, the metal oxides, the target metal NPs, or combinations of these (e.g. nickel metal, NiO, Ni_2O_3, NiX_2). Similar analytical criteria are needed for the formation of inorganic materials such as ZnO and TiO_2. Morphology alone could not differentiate these NPs as the same NPs sometimes existed in more than one oxidation state. In other cases, similar morphologies proved to be two different materials. Identification of the NPs necessitated having to index individual diffraction patterns, a very time consuming and tedious procedure.

To simplify the identification of materials when one has an idea what the material might be (i.e. NiO or Ni_2O_3), and standards with which to compare them, we present two easily applied and straightforward methods for analysis of electron diffraction (ED) patterns. Identifying total unknowns will still require indexing individual diffraction patterns. An example shown in Figure 2.1 illustrates that this technique can be applied to inclusions in tissue samples as well as to particulate materials.

2.2 Materials and Methods

2.2.1 *Materials*

Me_3PAuCl and $Co(II)Cl_2$-$6H_2O$ were purchased from Sigma Aldrich, and $Ni(II)Cl_2$-$6H_2O$ was purchased from Fisher Scientific. The pcDNA3.1(+) plasmid was obtained from Invitrogen, amplified with Qiagen kit to a mother stock suspension of 1 μg/μl and diluted when mixed with

the cationic-containing solutions. The 12 mM stock solutions of metal chlorides were prepared in nanopure water. The gold solution was prepared by adding an equal portion of deionized water to 100 mL of a 24 mM stock solution of Me_3PAuCl dissolved in acetone. $Zn(NO_3)_2$ was purchased from Sigma Aldrich and dissolved in deionized water at a concentration of 50 mM. Tris (Sigma Aldrich) was prepared in deionized water at a concentration of 100 mM. Tris-EDTA (TE) buffer (10 mM Tris, 1 mM EDTA, pH 8) was included in the Qiagen kit.

2.2.2 *Instrumentation*

Samples for TEM observation and μD were dispersed onto carbon-coated copper grids (Electron Microscopy Sciences). The samples were imaged, and the μD patterns collected at 120 kV using a Tecnai G2 Biotwin (FEI). All images and μD patterns were collected with an AMT 2K CCD camera.

We obtained μD patterns of known standards and then, under the exact same conditions (kV and camera length), we obtained μD patterns of the unknowns. For both methods to work successfully, one must ensure that both the standard and the unknown are in the eucentric position for both imaging and diffraction pattern acquisition. This ensures accurate camera length comparisons. Images of the μD patterns were saved as TIFF files for data comparison in Adobe Photoshop, where the diffraction patterns were colorized and superimposed using the layer palette.

2.3 Results and Discussion

2.3.1 *Method 1*

After collecting the diffraction patterns, they were pseudo-colored in Adobe Photoshop and these colorized patterns were overlaid for direct comparison. This simple technique requires

only the superimposition of the μD pattern of the standard metal or non-metal with the experimental pattern of the analyzed sample of interest. In order to obtain an accurate and reproducible superimposition, the patterns have to be collected under the identical conditions discussed above and within relatively close time frames. By overlaying the patterns, we obtained instant and distinct matches or mismatches. Diffraction patterns considered as mismatches were patterns that contained extraneous d-spacings from those in the standards.

In Figure 2.1 three NPs of distinctly different known materials are compared (red: rutile TiO_2; green: mercury; blue: zinc). This illustrates non-overlapping mD patterns. There is the possibility, when using spot patterns, that such non-overlapping spot patterns could be from the same material, but the diffraction patterns were taken of differently oriented particles. In our case the particle differences were also confirmed by energy dispersive analysis (EDS). Ring patterns, which are usually produced from many differently oriented particles, eliminate this possibility. Indeed, when there are numerous particles, the discrete diffracted beams combine to form a continuous ring as shown in Figure 2.3A as compared to Figures 2.4 where fewer NPs are producing the mD patterns therefore individually diffracted beams are visible.

Overlaying these colorized diffraction patterns in Photoshop allows for rapid screening of samples, by matching diffraction patterns to known standards or seeing definitive differences. Figures 2.2C and 2.3C show matching diffraction patterns of an unknown and known material. This is an effective way to rapidly verify if the identity of your unknown matches your standard and may be applicable as an analytical tool for the quality control of production batches of nanomaterials and/or biological-related materials (see skin tattoos shown in Figure 2.1). Using this method, we have successfully identified the metal properties of plasmid DNA-molded nanodiscs of gold (Figure 2.2) and nickel nanoparticles (Figure 2.3). We

were able to vary conditions to fabricate size tunable gold and nickel, and ensure by this method, that we were producing the same material.

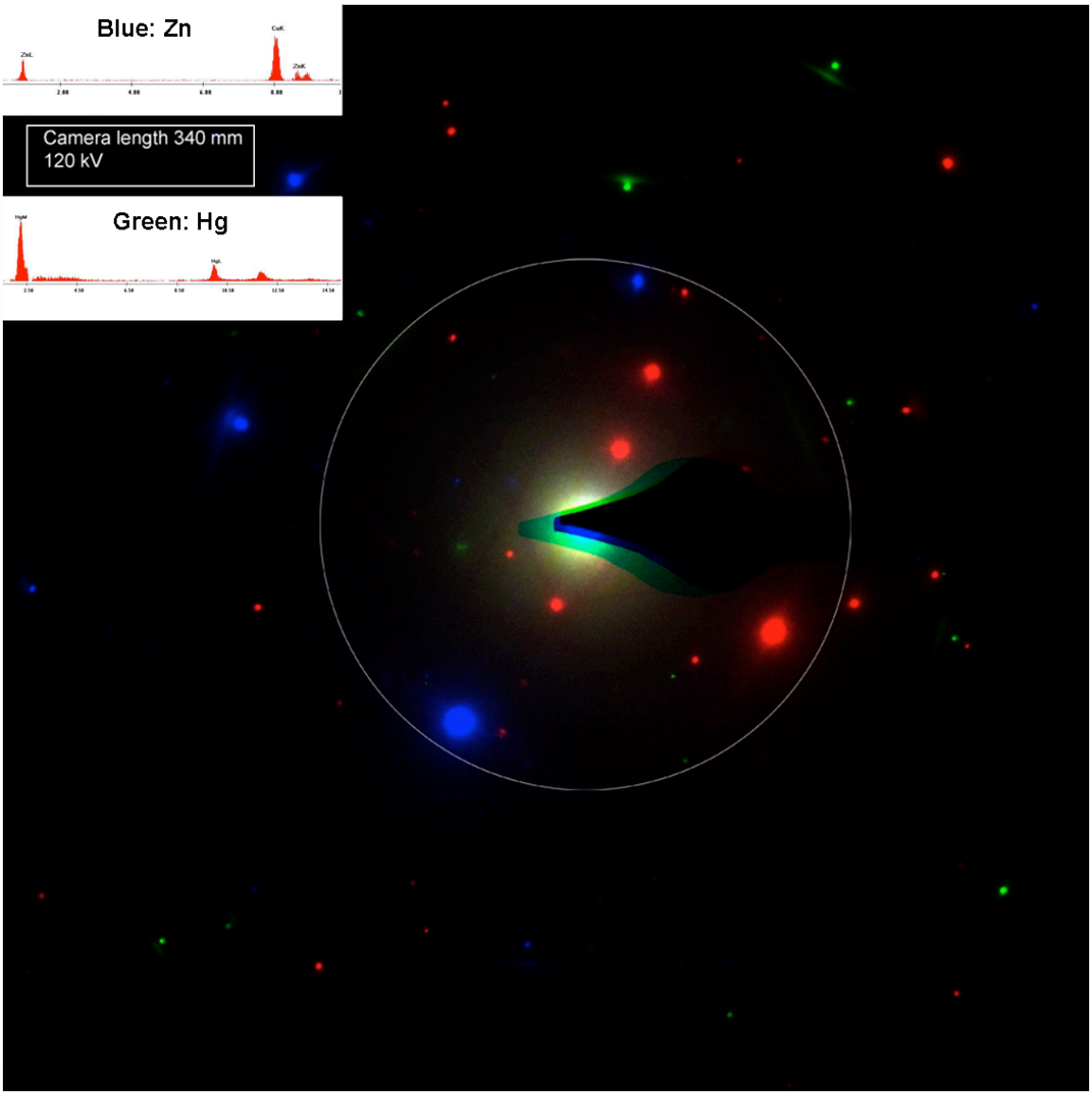

Figure 2.1. Microdiffraction (mD) patterns of a known material (TiO_2, red) and two unknown nanoparticles (NPs) from a colored tattoo (blue: Zn; green: Hg) collected at the same kV and camera length (120 kV and 340 mm). EDS spectra of Zn and Hg are shown in the inserts on the top left corner. Using the colorized image overlay method and rotating the images relative to one another, no matching patterns could be identified. The white circle was inscribed to help center the beam stop. The blue dots, representing two diffracted beams from the same diffraction ring, are equidistant from the central spot. When the beam stop is correctly positioned, then the two blue diffracted beams are equidistant from the white circle.

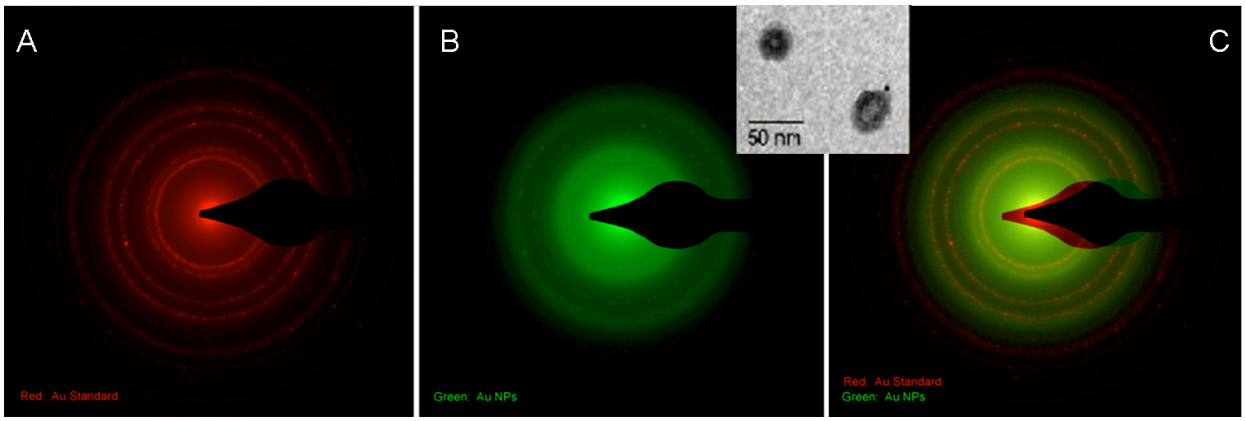

Figure 2.2. (A) A mD ring pattern from an evaporated gold standard. (B) A mD pattern of several gold particles prepared using toroidal DNA to control the size. (C) Superimposition of gold standard A and identified unknown B. The TEM image (insert) shows the toroidal DNA/gold formation. Note that the inner more intense rings, when superimposed, become yellow whereas the outer less intense rings maintain their original color.

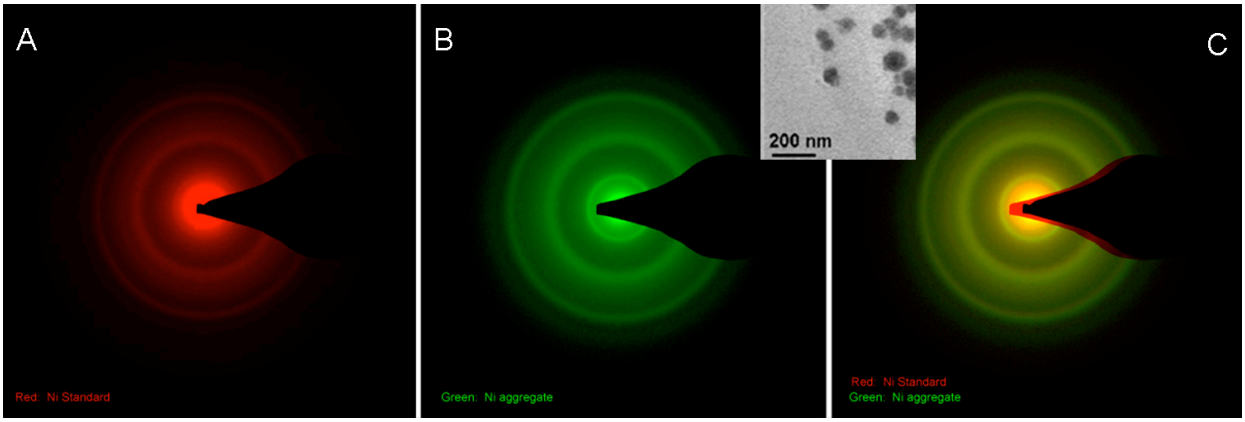

Figure 2.3. (A, red) A μD pattern from an evaporated nickel standard. (B, green) A μD pattern from an aggregate of Ni NPs. (C) Superimposition of nickel standard A and identified unknown B. The TEM image (insert) shows the Nickel NP formation upon DNA mold degradation. This color change of the μD pattern occurs only when the unknown μD pattern comes from a large number of NPs (i.e. the intensity of the μD pattern ring is strong). When there are numerous particles, the discrete diffracted beams combine to form a continuous ring as compared to Figure 2.4 where fewer NPs are producing the μD patterns.

2.3.2 *Method 2*

A μD pattern from a standard of ZnO powder on a carbon-coated grid was collected and printed on an overhead transparency. The transparency was then overlaid onto the standard μD pattern on the CCD monitor to check if any distortion of the μD pattern occurred when printing onto the transparency. To compare a μD pattern from an unknown to the standard, the transparency was overlaid on the unknown diffraction pattern directly on the CRT monitor of the AMT camera. Diffraction patterns considered as mismatches were patterns that contained extraneous d-spacings from those in the standards. Considered a match to the standard, the μD pattern on the CRT had to match with at least five of the standard's d-spacings.

As the synthesis processing was refined, and μD confirmed the homogeneous nature of the desired NPs, this method allowed us to check the results and make a rapid assessment and adjustment to our synthesis within the time frame of a couple of hours. This method is the easier of the two methods for comparison of standard selected area diffraction (SAD) patterns or large area μD patterns where ring patterns are formed.

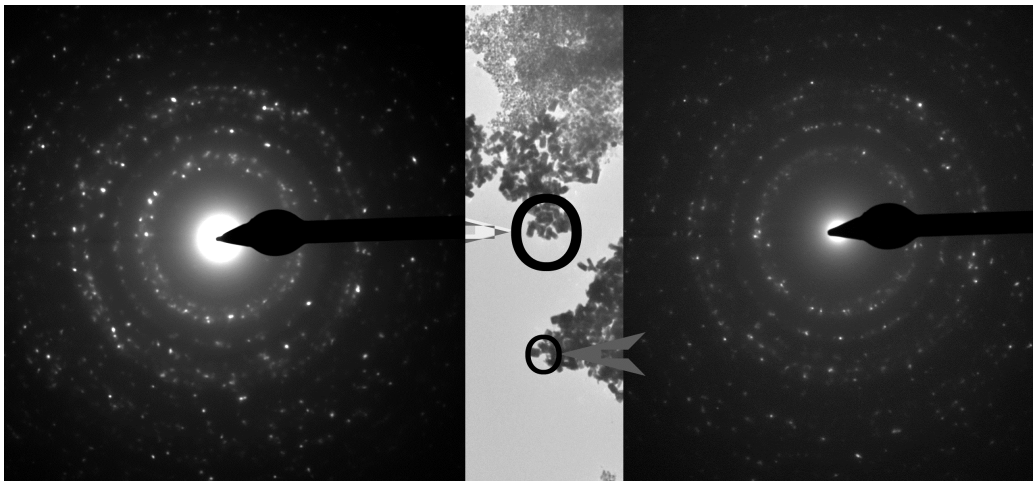

Figure 2.4. μD pattern images displayed on a monitor corresponding to unknown NP aggregates that were identified as ZnO by Method 2 (overhead transparency method).

2.4 Conclusions

A full match of the superimposed standard and experimental unknown μD patterns by both digital image overlay and overhead transparency methods allow us to obtain a swift and accurate determination of the nature of the material investigated without tedious indexing of individual diffraction patterns as long as standards are available. To ensure accuracy of these comparisons, it is essential that the same conditions are used to obtain the diffraction patterns to be compared (i.e. kV, camera length, and eucentric position for simultaneous imaging and collecting diffraction patterns). This ensures accurate comparisons.

Methods 1 and 2 will work even when only milligrams or micrograms of material is available, for example when analyzing NPs formed in microfluidic reactors [15]. The methods described herein (i.e. μD where the beam is used to select the area) can be used on any TEM, and is especially useful on those TEMs not equipped with a SAD aperture.

2.5 References

1. Alivisatos, A.P., *Semiconductor Clusters, Nanocrystals, and Quantum Dots.* Science, 1996. **271**(5251): p. 933-937.
2. Stellacci, F., *Nanoscale materials: A new season.* Nat Mater, 2005. **4**(2): p. 113-114.
3. Sharma, P., et al., *Gold-Speckled Multimodal Nanoparticles for Noninvasive Bioimaging.* Chem. Mater., 2008. **20**(19): p. 6087-6094.
4. A Wieckowski et al., *Catalysis and Electrocatalysis at Nanoparticle Surfaces*2003, New York: Marcel Dekker.
5. Grzelczak, M., et al., *Directed Self-Assembly of Nanoparticles.* ACS Nano, 2010. **4**(7): p. 3591-3605.
6. Song, Q. and Z.J. Zhang, *Shape Control and Associated Magnetic Properties of Spinel Cobalt Ferrite Nanocrystals.* J. Am. Chem. Soc., 2004. **126**(19): p. 6164-6168.
7. Cross, S.E., et al., *Human Skin Penetration of Sunscreen Nanoparticles: In-vitro Assessment of a Novel Micronized Zinc Oxide Formulation.* Skin Pharmacology and Physiology, 2007. **20**(3): p. 148-154.
8. Beek, W.J.E., M.M. Wienk, and R.A.J. Janssen, *Hybrid polymer solar cells based on zinc oxide.* J. Mater. Chem., 2005. **15**(29): p. 2985-2988.
9. Samson, J., et al., *Fabrication of Metal Nanoparticles Using Toroidal Plasmid DNA as a Sacrificial Mold.* ACS Nano, 2009. **3**(2): p. 339-344.
10. Masala, O. and R. Seshadri, *SYNTHESIS ROUTES FOR LARGE VOLUMES OF NANOPARTICLES.* Annual Review of Materials Research, 2004. **34**(1): p. 41-81.
11. Russell, J.J.B.a.L.D., *Electron Microscopy*1992, Boston: Jones and Bartlett Publishers.
12. B.E.P. Beeston, R.W.H.a.R.M., *Electron Diffraction and Optical Diffraction Techniques.* : Elsevier Science Ltd.
13. Eades, A., *One of my Failures: Diffraction in the TEM.* Microscopy Today, 2011. **19**(01).
14. Steeds, J.W., *Introduction to Analytical Electron Microscopy*1979.
15. Song, Y., et al., *Microfluidic Synthesis of Cobalt Nanoparticles.* Chem. of Mater., 2006. **18**(12): p. 2817-2827.

Chapter 3

FABRICATION OF METAL NANOPARTICLES USING TOROIDAL PLASMID DNA AS A SACRIFICIAL MOLD*

3.1 Introduction

Nanomaterials of metals, ceramics, inorganics, and organic dyes have shown atypical or unanticipated properties, which have been exploited for a wide variety of applications.[1-4] Metal nanoparticles are fabricated using a variety of methods, including reduction of the metal salts with reducing agents, [5] pyrolysis, [6-8] laser ablation, [9, 10] and photoreduction. [11, 12] The average nanoparticle size ranges from a few nanometers to more than 100 nm. The size, shape, and dispersity depend on the synthetic methods and can be controlled by modifying both the thermodynamic and kinetic parameters. [6] Several templates can be used in the preparation of nanoparticles to control their size. A great number of platforms have been used to template nanomaterial fabrication: carbon nanotubes, [13] aggregates, [14] organic polymers, biopolymers, [15-17] and biological systems, e.g., viruses. [18] The above mentioned molecules

* This work was published on *ACSNano* with the same title. *Note: This publication was featured in the Editorial of ACS Nano magazine (February 2009) and in the National Science Foundation bulletin entitled "Proposed Realignment of the Division of Chemistry Programs: Nanochemistry."*

can be used as a platform on which nanoparticles can be adsorbed or synthesized as a method to order the nanoparticles in two or three dimensions. Furthermore, nanoparticles can be formed in a variety of matrixes such as gels, [19, 20] polymers, [21] and biopolymers, [22] which can control the stability and induce a specific shape.

Self-organized biomolecules can be used to drive the formation of the nanoparticle within their cavities and control the growth of the nanoparticle. However, these products are formed in low yields. [23] When nanoparticles are molded in nanocavities or templates, the ideal mold is monodispersed, topologically well-defined and can be formed in high yield. Plasmid are a circular segment of DNA capable of replicating autonomously in bacterial hosts, [24] and can be produced in kilo-quantities following standard molecular biology procedures. [25] In addition to being a narrowly/mono dispersed biopolymer, plasmid DNA assumes a variety of topologies, including relaxed, linear supercoiled, and toroidal, depending on environmental conditions like temperature, pH, and ionic strength.

A recent report illustrated that ionic strength can maximize the toroidal topology of plasmid DNA. [26] According to the report, toroid thickness is a salt-dependent phenomenon which can be controlled by ionic strength. Under the same conditions, a given plasmid will always form the same size toroids. [26] Toroid size depends on a variety of factors, such as the sequence of the plasmid, the number of base pairs, and environmental factors. We present herein the use of the toroidal form of pcDNA 3.1(+) plasmid DNA (Figure 3.1) as a rigid narrowly dispersed bio-polymeric nanocavity, which mold the formation of disc-shaped nanoparticles of several types of metals. This approach exploits several properties of plasmid DNA:

(1) DNA affinity for metal cations [27]

(2) Toroidal plasmid DNA structures are favored by metal ionic binding [26]

(3) The plasmid size and therefore toroid cavity size is easy to vary [18, 19]

(4) The UV light initiated oxidation of DNA is well-established. [28-30]

3.2 Experimental Procedure

Materials. Me_3PAuCl and $Co(II)Cl_2 \cdot 6H_2O$ were purchased from Sigma Aldrich, and $Ni(II)Cl_2 \cdot 6H_2O$ was purchased from Fisher Scientific. The pcDNA3.1(+) plasmid was obtained from Invitrogen and stored in TE buffer (10 mM Tris and 1 mM EDTA). The 12 mM stock solutions of metal chlorides were prepared in nanopure water. The gold solution was prepared by adding an equal portion of deionized water to 100 mL of a 24 mM stock solution of Me_3PAuCl dissolved in acetone.

Instrumentation. *Atomic force microscopy* (AFM) was conducted using a Veeco Multimode SPM. Images were acquired in tapping mode using a rectangular cantilever from Mikromasch NSC15 series AlBS (nominal radius of curvature, RC = 10 nm, 325 kHz, and a spring constant = 40 nN/nm); with an aluminum-coated backside.

The Veeco SPM is equipped with software for processing the data which has been used together with Nanotech WSxM 4.0 Develop 12. Although the height measurements are accurate and reproducible from AFM experiments, the effect of the tip convolution (10 nm RC) is known to alter the lateral dimensions of the objects scanned [31]. *Transmission electron microscopy* (TEM) was performed using carbon-coated copper grids (EMS). The samples were imaged at 80 and 120 kV using a Tecnai G2 Biotwin (FEI). *ED* patterns were collected at 120 kV. The TEM images have been processed using Image J.

Synthesis of the Nanoparticles. Three 1mL Eppendorf tubes containing 10 μL of a suspension of plasmid pcDNA 3.1(+) (5428 base pairs, stored in TE buffer at -20 °C,

concentration: 1 μg/μL) were incubated overnight at 4 °C in the dark after adding 50 μL of a 12 mM solution of Me_3PAuCl, $Ni(II)Cl_2$, or $Co(II)Cl_2$, respectively, with a final salt concentration of 10 mM. The solutions were then irradiated by UV light for a total of 60 min (λ= 254 nm, 10 $\mu W/cm^2$ using a UVGL-25 compact UV lamp by UVP). The solutions were finally filtered through a 0.2 μm syringe filter (Nalgene). The samples for AFM experiments were prepared by slow evaporation of 5 μL of solution on mica or highly ordered pyrolytic graphite (HOPG, SPI supplies). Images were collected from several different batches, and the distribution of diameters and heights was averaged between them. Samples for TEM were prepared similarly on the carbon-coated copper grids. We have observed that TEM analysis can transform metal salts deposited on the TEM grid into metallic materials. The standard reduction potentials (at RT = 25°C) of the three metal ions used are: +1.69 V for $Au_{(s)}$ (from $Au^{1+}_{(aq)}+1e^{-1}$), -0.25V for $Ni_{(s)}$ (from $Ni^{2+}_{(aq)}+2e^{-1}$), and -0.28V for $Co_{(s)}$ ($Co^{2+}_{(aq)}+2e^{-1}$). [32]

3.3 Results and Discussion

3.3.1 Fabrication of Nanoparticles

Incubation of low concentrations of Me_3PAuCl, $NiCl_2 \cdot (H2O)_6$, or $CoCl_2 \cdot (H2O)_6$ with pcDNA 3.1(+) plasmid DNA, which has 5428 base pairs, does not affect the distribution of the three main topologies significantly (Figure 3.6). UV irradiation (254 nm) of the plasmid shows a redistribution of the conformations and degradation in the presence of the three metal ions. Photo-oxidation and degradation of the DNA mold upon exposure of the sample to 254 nm UV light results in reduction of the metal ions such that the plasmid DNA acts as a sacrificial mold and drives the formation of the nanoparticles. After incubation of the plasmid DNA suspension (10 μL of a 1 μg/μL original solution) with the gold, nickel, or cobalt salts (12 mM) overnight in the dark at 4 °C, the nanoparticles were prepared by irradiating the solution for one hour with

UV light (λ = 254 nm, 10 $\mu W/cm^2$ using a UVGL-25 compact UV lamp by UVP). The solutions were then cast onto AFM or TEM substrates through a 0.2 μm syringe filter. See Figure 3.15 for controls without the plasmid.

3.3.2 Characterization of the Nanoparticles

Atomic Force Microscopy (Figure 3.3) and Transmission Electron Microscopy (Figure 3.4) were used to characterize the heights and widths of the metal nanoparticles, respectively. The histograms of the AFM-measured heights and the TEM-measured horizontal dimensions are presented in Figure 3.2. The vertical and horizontal dimensions of the metal nanoparticles reveal that these nanoparticles are disc-shaped. The average height of the nickel and cobalt nanodiscs obtained from pcDNA 3.1(+) templates is 13±2 nm, while for gold the average height is 8±2 nm. These nanoparticle heights correspond with the 12-14 nm vertical dimension of the plasmid. The 40-60 nm diameters of the metallic nanodiscs correspond to the inner diameter of the toroidal plasmid (Figure 3.1), and the differences are discussed below.

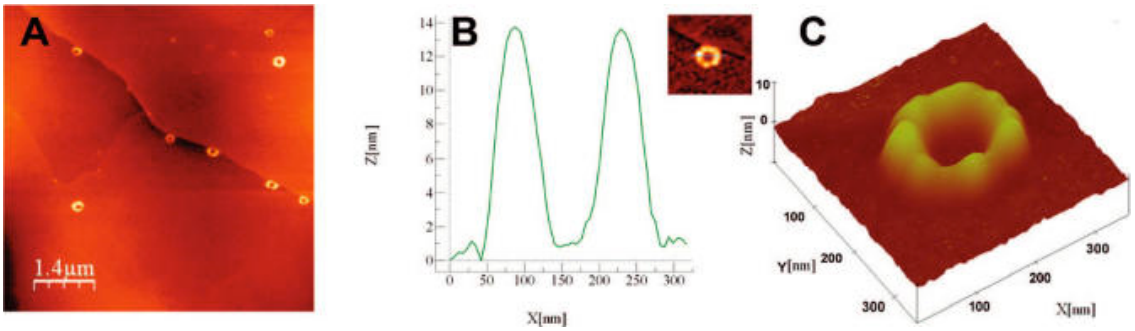

Figure 3.1. (A) AFM height image of the toroidal topology of plasmid pcDNA 3.1(+) on a HOPG substrate. (B) Height analysis of inset (top right corner). (C) 3-Dimensional AFM image of the plasmid shown in B.

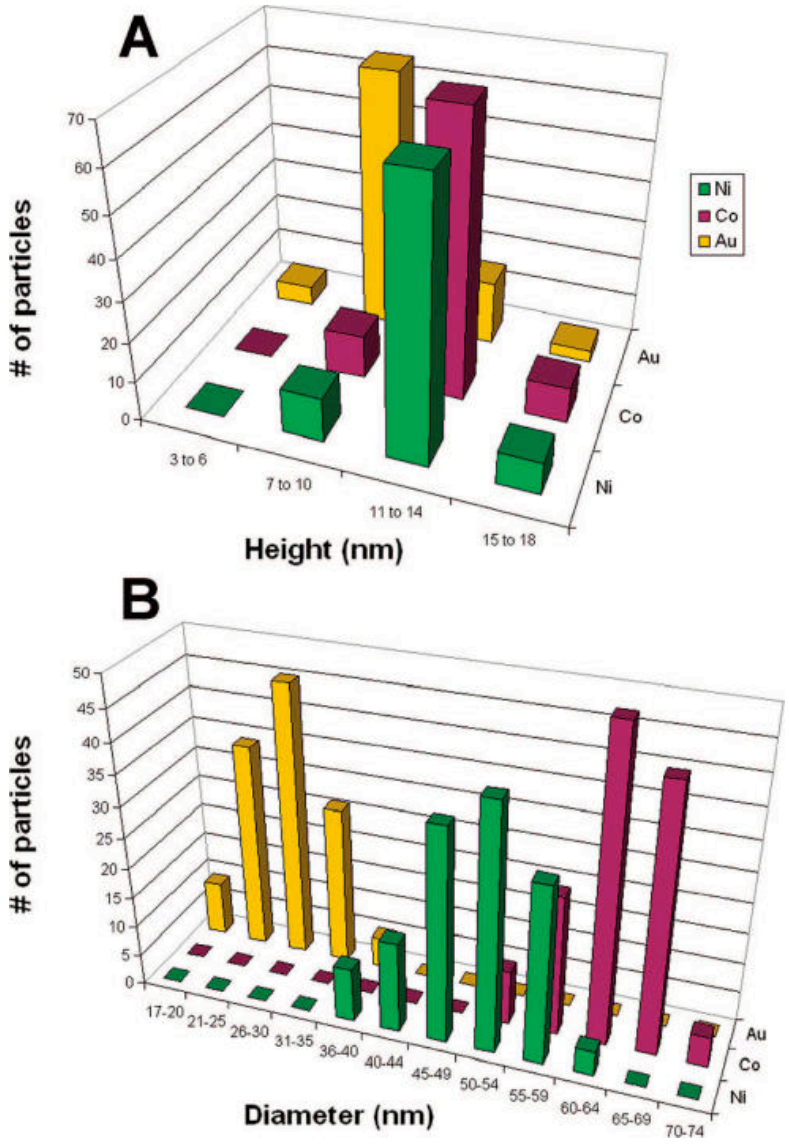

Figure 3.2. (A) Histograms of the height distribution determined by AFM and (B) histograms of the diameter distribution determined by TEM: nickel (green), cobalt (purple), and gold (yellow) nanoparticles obtained using a pcDNA 3.1(+) template**.**

The small differences in the nanoparticle heights and widths for the three metals can be attributed to several factors. As mentioned before, the relative distribution of the toroidal/supercoiled condensation state *versus* the linear and relaxed forms does not significantly change upon binding of low concentrations of these metals (Figure 3.6) and is in agreement with a previous study. [26] However, the dimensions of the toroidal condensation state of the plasmid

are sensitive to the binding of the different metal ions, [33-35] and the morphology of the plasmid changes during the formation of the nanoparticles as it is degraded under UV irradiation. Photoinduced metal coating of linear DNA with concomitant photo-oxidation of DNA to yield nanowires has been reported. [36, 37]

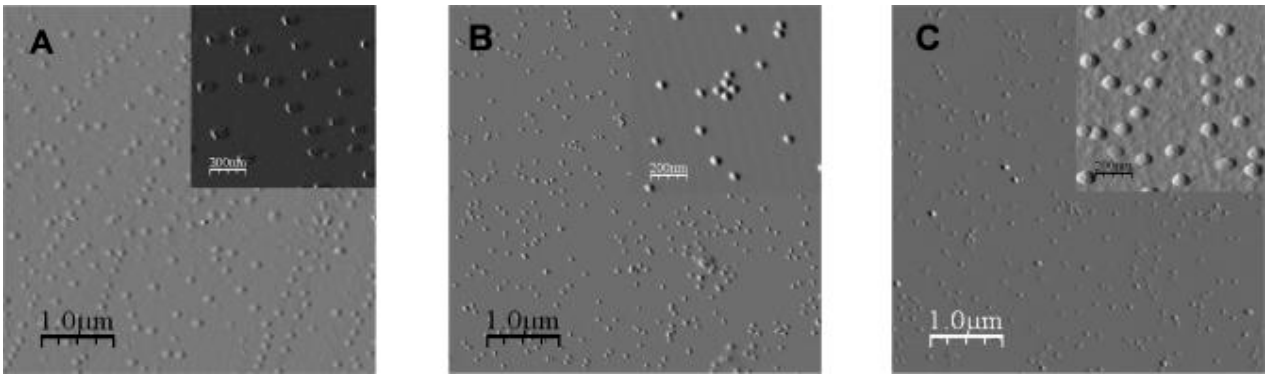

Figure 3.3. AFM amplitude images of metal nanoparticles obtained from photo-initiated reduction of metal ions bound to plasmid pcDNA 3.1(+) sacrificial mold: (A) gold; (B) nickel; (C) cobalt particles.

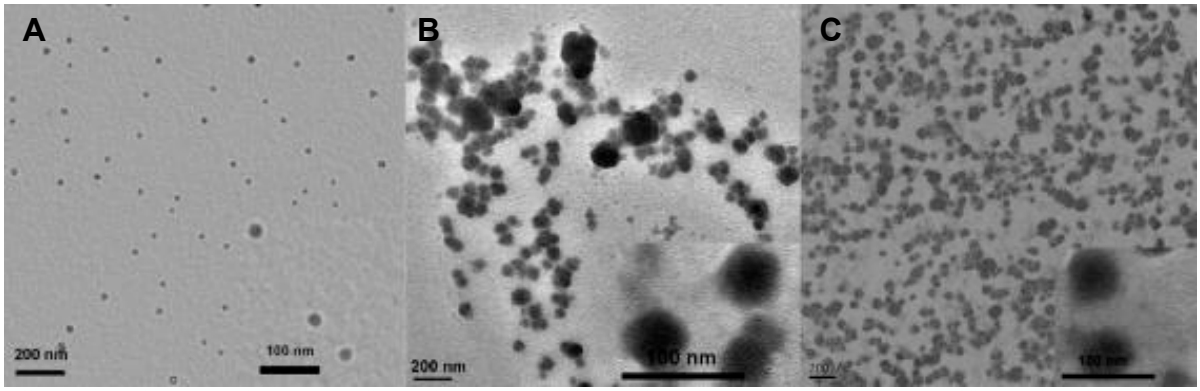

Figure 3.4. TEM images were used to assay the diameters of metal nanodiscs obtained from photoinitiated reduction of metal ions bound to plasmid pcDNA 3.1(+) sacrificial mold: (A) gold nanoparticles, (B) nickel nanoparticles, and (C) cobalt nanoparticles.

In our study, even though the mechanism of photoreduction of the metal may occur in a similar fashion, the circular morphology of the toroidal DNA clearly drives the formation of

nanodisc topologies. The size of the nanodisc is correlated to the inner diameter of the plasmid and circular DNA but is not exactly the same. When the plasmid is incubated with the gold salt or nickel salt and irradiated for 5-20 min with the UV light, there is a significant contraction in the plasmid height (Figure 3.8, B). After UV irradiating for 20 min, the forming particle is still surrounded by filaments of DNA (Figure 3.11). To probe the possible mechanism(s) for the formation of nanoparticles, we used AFM scans of a drop of solution containing pcDNA and $NiCl_2$ on HOPG after UV irradiation for 20, 40, and 60 min. The images suggest that there is a contraction of the plasmid soon after irradiation. After 20 and 40 min, filaments of DNA are still visible, whereas after 60 min the photodegradation process is complete, and only nanoparticles are visible (Figure 3.10). Electron diffraction analysis (Figure 3.5) suggests that most of the nanodiscs are composed only of the metal atoms. Some DNA fragments adsorbed to the outside of the nanoparticle are occasionally observed in both AFM and TEM images.

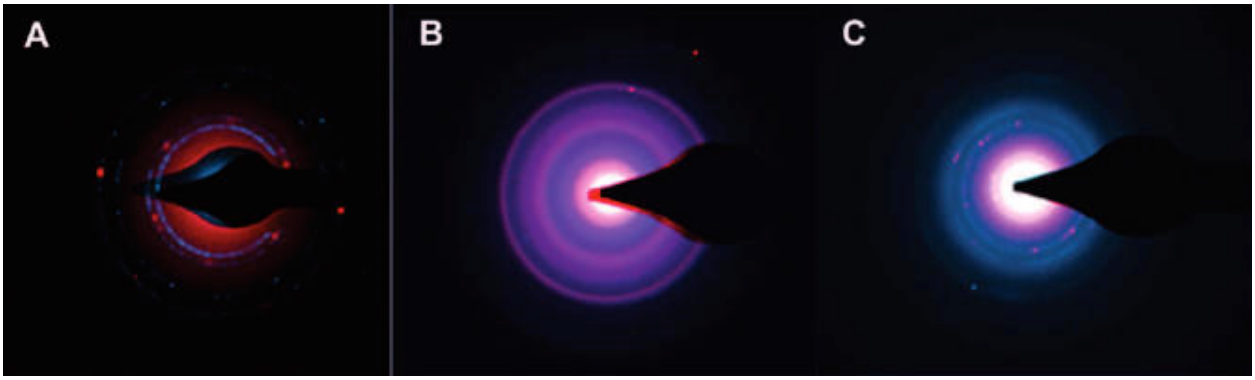

Figure 3.5. ED patterns in red of the prepared nanodiscs of (A) gold, (B) nickel, and (C) cobalt. The corresponding standards are superimposed and are in blue.

As noted above, incomplete degradation of the plasmid DNA and DNA decorated with small metal nanoparticles are observed in experiments with shorter UV irradiation times. Only

amorphous clusters of various sizes are observed in control experiments with no plasmid DNA. Chemical reduction of these metal ions with hydrazine anhydrous results in similar nanodiscs with similar shapes, but the plasmid DNA surrounds the nanoparticles or is entrained in the nanoparticles depending on growth conditions (Figure 3.10 & 3.11). Taken together, these data suggest that small changes in the toroid dimensions of the plasmid DNA can be induced by the binding of different metal ions [19-22] and that the detailed mechanism and kinetics of nanodisc formation may be somewhat metal ion dependent. As with other template methods [23] it is likely that the increased concentration of the metal ion inside the toroid relative to the outside drives the formation of the nanodiscs. In the case of a sacrificial mold, the competing rates of nanoparticle formation *versus* mold degradation, which also may be metal ion dependent, will also influence the size and morphology of the products.

3.3.3 Use of Different Plasmids

Other plasmids with different numbers of base pairs and sequences can adopt similar structures but with different sizes, though the size of the toroidal condensation state does not linearly scale with the number of base pairs. The plasmid pRc/CMV-(HA)-pVHL, abbreviated as pVHL, has *ca.* 8000bp and also adopts toroidal conformations (Figure 3.8). The same procedures as above using the larger pVHL plasmid result in larger gold, nickel, and cobalt nanodiscs with different heights (Figure 3.9). A much smaller circular DNA containing 70 base pairs is able to mold the formation of 3 ± 0.5 nm high by 13 ± 5 nm wide nanoparticles of nickel (Figure 3.14). Note that the AFM error for these smallest nanoparticles is greater due to convolution with the 10 nm tip curvature, so that the actual diameter is less than observed. Figure 3.7 shows the

histogram of the height as well as the diameter distribution of nanoparticles using the two different plasmids and p70.

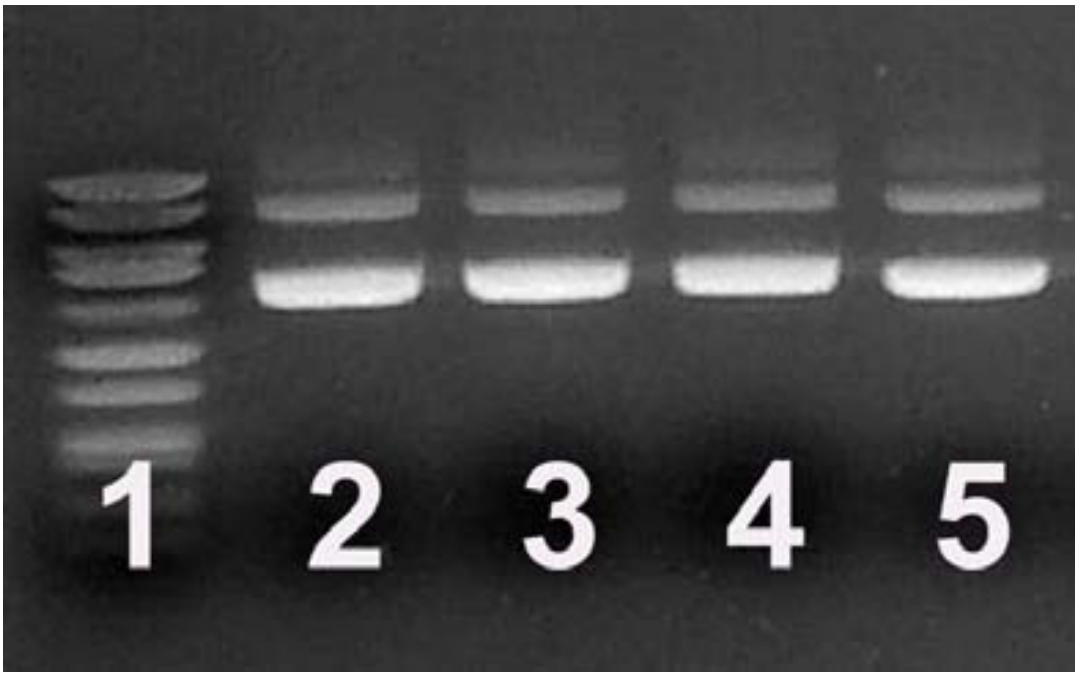

Figure 3.6. Gel electrophoresis (0.8% agarose) of pcDNA 3.1(+). Lanes: [1] 1kb ladder; [2] naked pcDNA; [3] pcDNA + 10 mM Me_3PAuCl; [4] pcDNA + 10 mM $NiCl_2$; [5] pcDNA + 10 mM $CoCl_2$, incubated overnight before analysis. The lowest band is the toroidal/supercoiled condensation state of the plasmid while the middle is a linear supercoiled, and the top band has a relaxed topology.

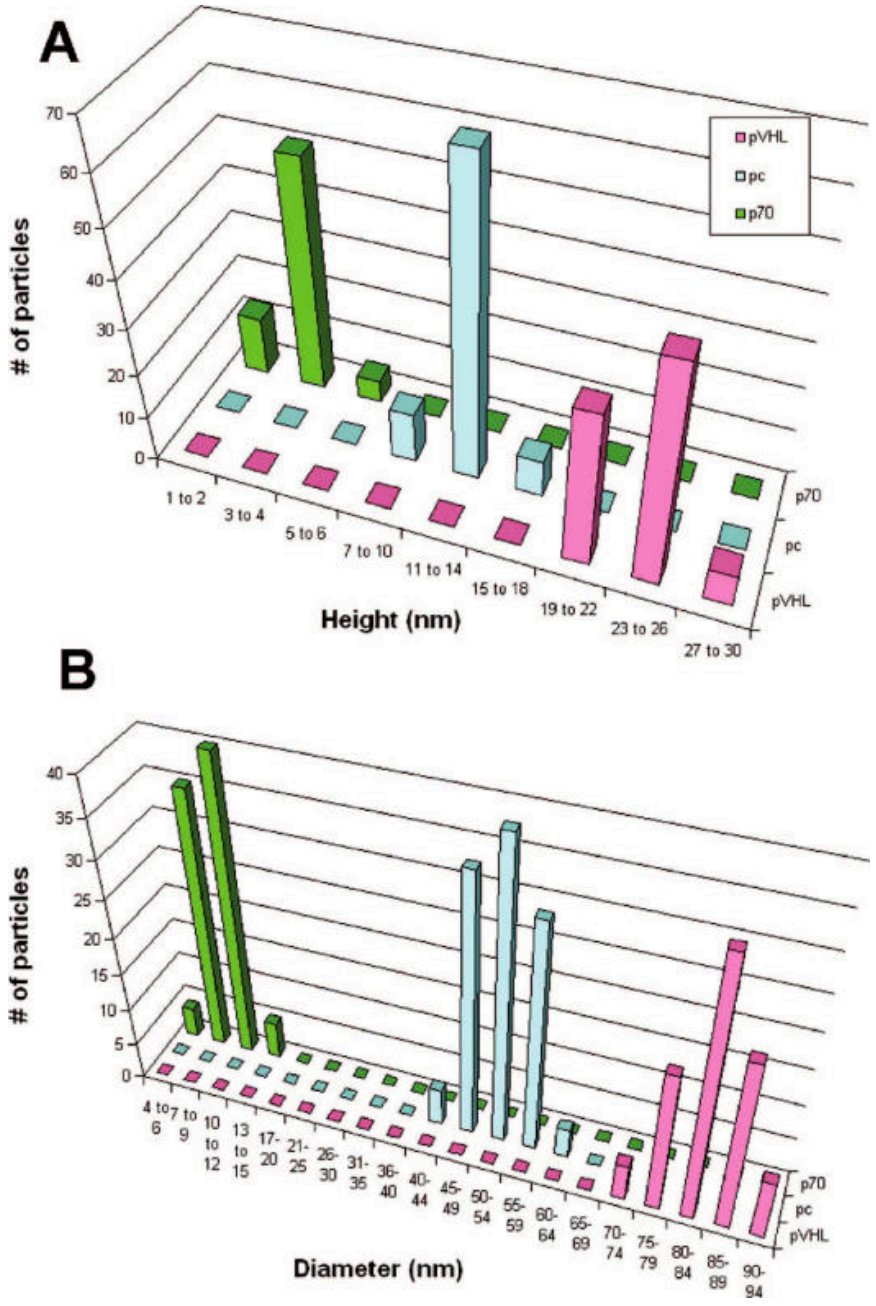

Figure 3.7. (A) Histograms of the height and (B) histogram of the diameter distribution determined by AFM of nickel nanoparticles using p70 (olive green), pcDNA (light blue), and pVHL (pink) as molds. The diameter measurements were estimated from the AFM height images; a 10 nm ultra-sharp tip was utilized to minimize the error due to the tip convolution effect.

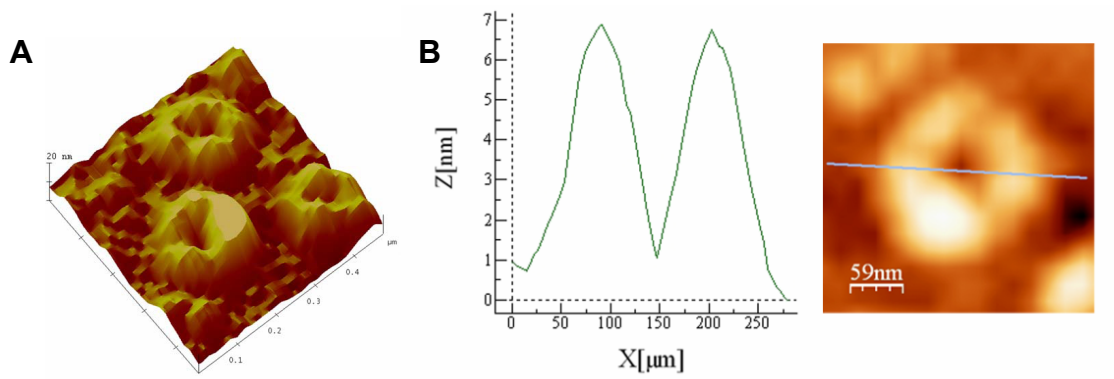

Figure 3.8. (A) 3-dimensional AFM image of toroidal topology of pVHL (B) AFM analysis with corresponding AFM image of a plasmid pcDNA 3.1(+) incubated with 12 mM water/acetone solution of Me_3PAuCl and UV irradiated for 5 minutes.

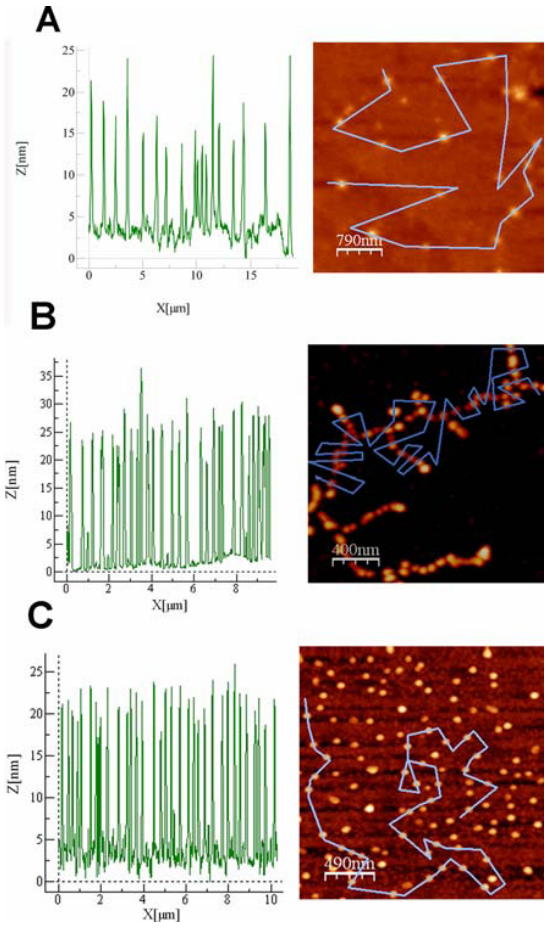

Figure 3.9. The three panels show the average heights of gold (A), nickel (B) and cobalt (C) nanoparticles synthesized using plasmid pVHL with corresponding AFM image [38]. The average height of the gold nanoparticles is 18 ± 3 nm, of the nickel nanoparticles is 25 ± 2 nm and of the cobalt nanoparticles is 20 ± 3 nm.

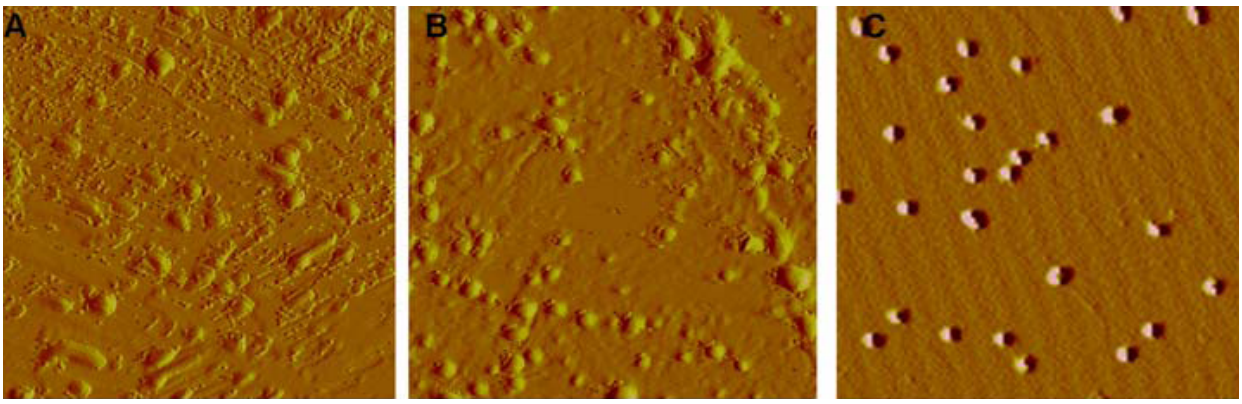

Figure 3.10. AFM images (1.5x1.5 μm) of plasmid DNA/$NiCl_2$ on HOPG after different times of exposure to UV light: (A) 20, (B) 40, and (C) 60 minutes. Figure A and B suggest that after UV irradiation the plasmids undergo a contraction with concomitant formation of the nanoparticles of nickel. Only after some time (60 minutes, figure C) the process is complete and the plasmids have been degraded and the particles formed.

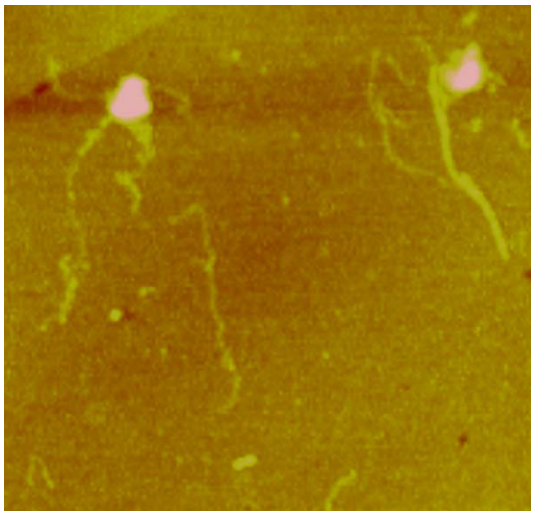

Figure 3.11. AFM image of plasmid DNA/Me_3PAuCl on HOPG after exposure to UV light (20 minutes) (0.75X0.75 μm). Filaments of DNA are still visible. The morphology of the particle is driven by the degrading plasmid which wraps around the forming particle (see Figure 3.10 lane 8).

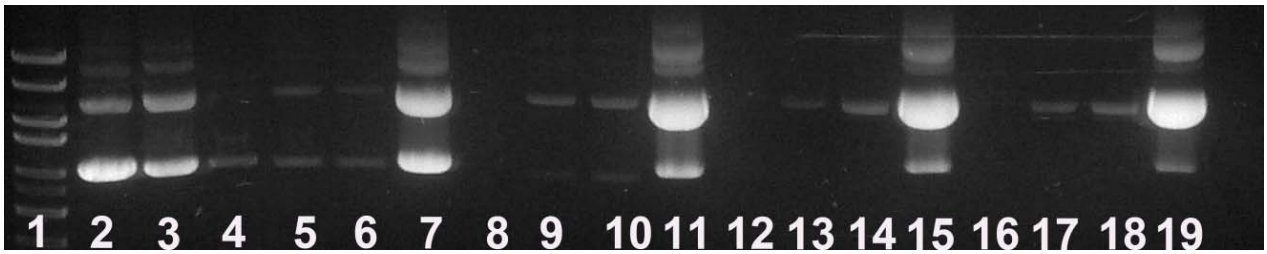

Figure 3.12. Gel electrophoresis (GE, 0.8% agarose) of pcDNA 3.1(+). Lanes: [1] 1kb ladder; [2] naked pcDNA 3.1(+); [3] naked pcDNA 3.1(+) + UV (5 min); [4] pcDNA + Me_3PAuCl + UV (5min); [5] pcDNA + $NiCl_2$ +UV (5 min); [6] pcDNA + $CoCl_2$ +UV (5 min); [7] naked pcDNA 3.1(+) + UV (20 min); [8] pcDNA(+) + Me_3PAuCl + UV (20 min); [9] pcDNA(+) + $NiCl_2$ +UV (20 min); [10] pcDNA(+) + $CoCl_2$ + UV (20 min); [11] naked pcDNA 3.1(+) + UV (40 min); [12] pcDNA(+) + Me_3PAuCl + UV (40 min); [13] pcDNA(+) + $NiCl_2$ +UV(40 min); [14] pcDNA(+) + $CoCl_2$ +UV (40 min); [15] naked pcDNA(+) 3.1(+) + UV (60 min); [16] pcDNA(+) + Me_3PAuCl + UV (60 min); [17] pcDNA(+) + $NiCl_2$ + UV (60 min); [18] pcDNA(+) + $CoCl_2$ +UV (60 min); [19] naked pcDNA 3.1(+) + UV (90 min).

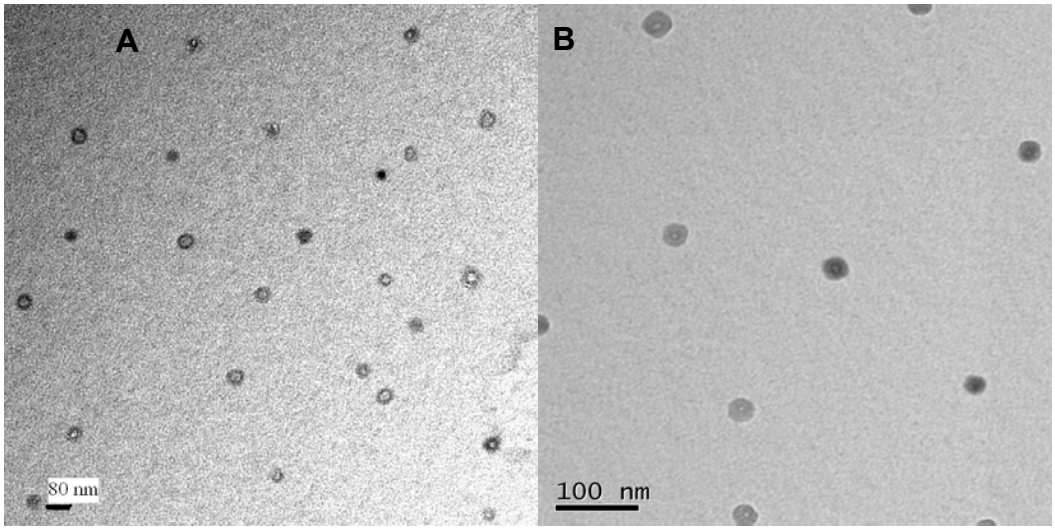

Figure 3.13. TEM images of (A) toroidal DNA topologies after incubating pcDNA 3.1(+) with 12 mM water/acetone solution of Me_3PAuCl, and (B) gold particles resulting after UV irradiating for 5 minutes. The presence of toroids and gold particles of different electron densities suggests a mechanism for the formation of the nanodiscs. While the rearrangement of the plasmid dimensions occurs upon irradiation, the particle is ejected from the degrading template after further DNA oxidation (see also Figure 3.10).

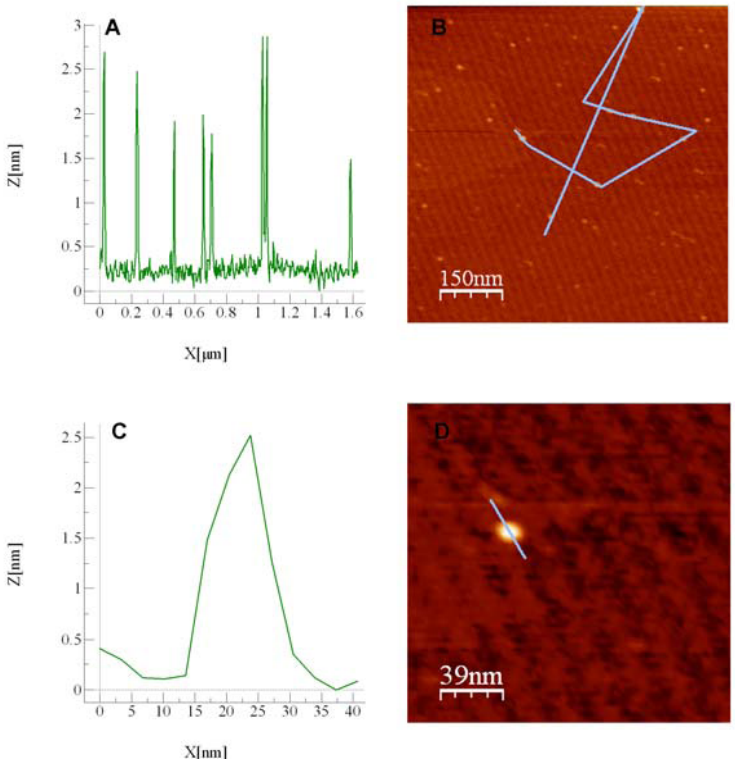

Figure 3.14. (A) Height analysis of (B) AFM image of nickel nanoparticles fabricated using a 70bp circular DNA as a template. (C) Height analysis of (D) AFM height image single nickel nanoparticle.

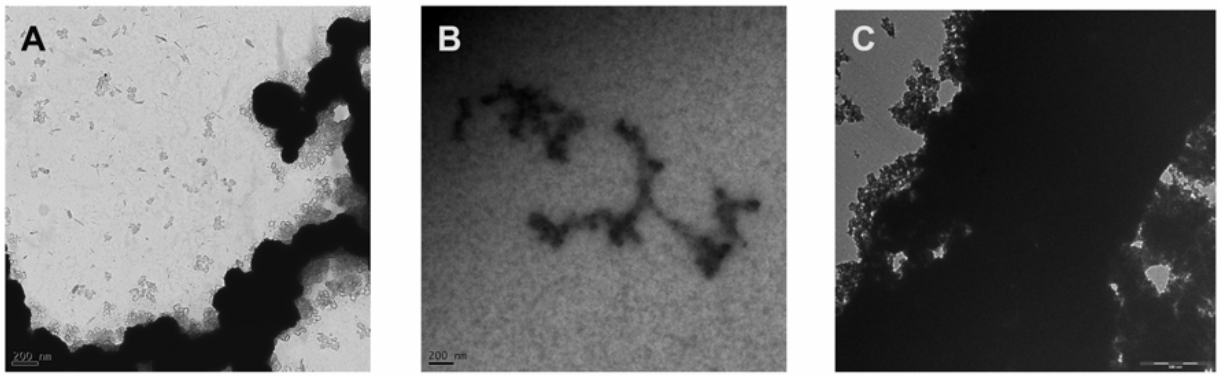

Figure 3.15. TEM images of the control experiments without the employment of plasmid DNA as a template. Aqueous solutions of (A) Me_3PAuCl, (B) $NiCl_2$, and (C) $CoCl_2$ were irradiated with UV light. Neither narrowly dispersed sizes nor disc-like shapes are observed

3.4 Conclusions

Narrowly dispersed nanodiscs were synthesized at room temperature using UV light and a biomolecular toroidal plasmid DNA mold. Toroidal plasmids are readily available in large quantities, easy to purify, rigid, and monodispersed. The size of the nanoparticle is directly related to the topology of the template, metal ion binding, and the mechanism of formation. The general feasibility of this methodology allows it to be applicable to DNA/RNA structures carrying more complex topologies. Finally, this method uses materials and equipment found in most undergraduate teaching laboratories. In Chapter 5, it will be shown that the fabrication of metal oxides, such as zinc oxide nanoparticle, is possible by tuning the procedural steps of this methodology.

3.5 Advantages and Drawbacks for this Approach

The experimental outcome for Ni, Co, and Au NPs is unified despite the large differences of REDOX potentials of Ni & Co Vs. Au. On the other hand, the power of UV light which initiates the reduction of Ni, Co, and Au cations into metal must have a constant flux for reproducibility. The flux of energy that is emitted by the UV lamp used in our experiments decreases with time. The reason is related to the overheating of the lamp itself, which consequently results in a decreasing power outcome. The following chapters will present similar methodologies which do not involve UV irradiation because of the above-mentioned systematic error and will also show how the minimization of parameters and precursors efficiently still yield the desired products.

3.6 References

1. Lu, A.-H., E.L. Salabas, and F. Schüth, *Magnetic Nanoparticles: Synthesis, Protection, Functionalization, and Application.* Angew. Chem. Inter. Ed., 2007. **46**(8): p. 1222-1244.
2. Feldheim, D.L.F., C. A., Jr., *Metal Nanoparticles: Synthesis, Characterization, and Applications;*2002, Ne York: Marcel Dekker.
3. Drain, C.M., et al., *Porphyrin nanoparticles as supramolecular systems.* New J. Chem., 2006. **30**(12): p. 1834-1843.
4. Frenkel, J.D., J., *Spontaneous and Induced Magnetization in Ferromagnetic Bodies.* Nature, 2003: p. 274–275.
5. Guo, F., et al., *Synthesis of cobalt nanoparticles in ethanol hydrazine alkaline system (EHAS) at room temperature.* Mater. Lett., 2002. **56**(6): p. 906-909.
6. Puntes, V.F., K. Krishnan, and A.P. Alivisatos, *Synthesis of Colloidal Cobalt Nanoparticles with Controlled Size and Shapes.* Topics in Catalysis, 2002. **19**(2): p. 145-148.
7. Puntes, V.F., K.M. Krishnan, and P. Alivisatos, *Synthesis, self-assembly, and magnetic behavior of a two-dimensional superlattice of single-crystal ?Co nanoparticles*. Vol. 78. 2001: AIP. 2187-2189.
8. Kim, S.-W., et al., *Synthesis of Monodisperse Palladium Nanoparticles.* Nano Lett., 2003. **3**(9): p. 1289-1291.
9. Takami, A., H. Kurita, and S. Koda, *Laser-Induced Size Reduction of Noble Metal Particles.* J. Phys. Chem. B, 1999. **103**(8): p. 1226-1232.
10. Kazakevich, P.V., et al., *Laser induced synthesis of nanoparticles in liquids.* Applied Surface Science, 2006. **252**(13): p. 4373-4380.
11. Vesperinas, A., et al., *Light-induced flocculation of gold nanoparticles.* Chem. Commun., 2007(38): p. 3912-3914.
12. Fang, Q., et al., *Palladium nanoparticles on silicon by photo-reduction using 172 nm excimer UV lamps.* Appl. Surf. Sci., 2004. **226**(1-3): p. 7-11.
13. Chen, P., et al., *Synthesis of Cu Nanoparticles and Microsized Fibers by Using Carbon Nanotubes as a Template.* J. Phys. Chem. B, 1999. **103**(22): p. 4559-4561.
14. Banerjee, I.A., L. Yu, and H. Matsui, *Cu nanocrystal growth on peptide nanotubes by biomineralization: Size control of Cu nanocrystals by tuning peptide conformation.* P. Natl. A. Sci., 2003. **100**(25): p. 14678-14682.
15. Sun, L., et al., *Fabrication of silver nanoparticles ring templated by plasmid DNA.* Appl. Surf. Sci., 2006. **252**(14): p. 4969-4974.
16. Aldaye, F.A., A.L. Palmer, and H.F. Sleiman, *Assembling Materials with DNA as the Guide.* Science, 2008. **321**(5897): p. 1795-1799.
17. Coffer, J.L., et al., *Dictation of the shape of mesoscale semiconductor nanoparticle assemblies by plasmid DNA*. Vol. 69. 1996: AIP. 3851-3853.
18. Flynn, C.E., et al., *Viruses as vehicles for growth, organization and assembly of materials.* Acta Mater., 2003. **51**(19): p. 5867-5880.
19. Maruszewski, K., et al., *Raman Spectra of Molecules Adsorbed on Ag Centers in Sol-Gel Matrices.* J. Sol-Gel Sci. Techn., 2003. **26**(1): p. 83-88.
20. Antonietti, M. and G.A. Ozin, *Promises and Problems of Mesoscale Materials Chemistry or Why Meso?* Chemistry – A European Journal, 2004. **10**(1): p. 28-41.

21. Zhong, Z., et al., *d-Glucose-Derived Polymer Intermediates as Templates for the Synthesis of Ultrastable and Redispersible Gold Colloids.* Langmuir, 2008. **24**(9): p. 4655-4660.
22. Ganesan, R.G., Aharon, *Synthesis of WO3 nanoparticles using a biopolymer as a template for electrocatalytic hydrogen evolution.* Nanotechnology, 2008. **19**(2).
23. Djalali, R., J. Samson, and H. Matsui, *Doughnut-Shaped Peptide Nano-Assemblies and Their Applications as Nanoreactors.* J. Am. Chem. Soc., 2004. **126**(25): p. 7935-7939.
24. Lipps, G., *Plasmids: Current Research and Future Trends;*2008, Norfolk, U.K.,: Caister Academic Press:.
25. *QIAGEN PlasmidAmp Kit-For direct amplification of plasmid DNA from bacterial colonies*.
26. Conwell, C.C., I.D. Vilfan, and N.V. Hud, *Controlling the size of nanoscale toroidal DNA condensates with static curvature and ionic strength.* Proceedings of the National Academy of Sciences, 2003. **100**(16): p. 9296-9301.
27. Bloomfield, V.A., *Condensation of DNA by multivalent cations: Considerations on mechanism.* Biopolymers, 1991. **31**(13): p. 1471-1481.
28. Bartolini, W.P. and M.V. Johnston, *Characterizing DNA photo-oxidation reactions by high-resolution mass measurements with matrix-assisted laser desorption/ionization time-of-flight mass spectrometry.* J. Mass. Spectrom., 2000. **35**(3): p. 408-416.
29. Boerner, L.J.K. and J.M. Zaleski, *Metal complex-DNA interactions: from transcription inhibition to photoactivated cleavage.* Curr. Opin. Chem. Biol., 2005. **9**(2): p. 135-144.
30. Sinha, R.P. and D.-P. Hader, *UV-induced DNA damage and repair: a review.* Photoch Photobio. Sci., 2002. **1**(4): p. 225-236.
31. Wong, C.; West, P. E.; Olson, K. S.; Mecartney, M. L.; Starostina, *N. Tip Dilation and AFM Capabilities in the Characterization of Nanoparticles*. J. Met. **2007**, *59*, 12–16.
32. web.archive.org/web/20070518092613/http://www.northland.cc.mn.us/Chemistry /standard/standard_reduction_potentials.htm. Standard reduction potentials
33. Schnell, J. R.; Berman, J.; Bloomfield, V. A. *Insertion of Telomere Repeat Sequence Decreases Plasmid DNA Condensation by Cobalt (III) Hexaammine.* Biophys. J. **1998**, *74*, 1484–1491.
34. Davey, C. A.; Richmond, T. J. *DNA-Dependent Divalent Cation Binding in the Nucleosome Core Particle.* Proc. Natl. Acad. Sci. U.S.A. **2002**, *99*, 11169–11174.
35. Liu, C.; Wang, M.; Zhang, T.; Sun, H. *DNA Hydrolysis Promoted by Di- and Multi Nuclear Metal Complexes.* Coord. Chem. Rev. **2004**, *248*, 147–168.
36. Berti, L.; Alessandrini, A.; Facci, P. *DNA-Templated Photoinduced Silver Deposition.* J. Am. Chem. Soc. **2005**, *127*, 11216–11217.
37. Burley, G. A.; Gierlich, J.; Mofid, M. R.; Nir, H.; Tal, S.; Eichen, Y.; Carell, T. *Directed DNA Metallization.* J. Am. Chem. Soc. **2006**, *128*, 1398–1399.
38. Horcas, I.; Fernandez, R.; Gomez-Rodriguez, J. M.; Colchero, J. *WSXM: A Software for Scanning Probe Microscopy and a Tool for Nanotechnology.* Rev. Sci. Instrum. **2007**, *78*,013705.

Chapter 4

FABRICATION OF SIZE-TUNABLE METALLIC NANOPARTICLES USING PLASMID DNA AS A BIOMOLECULAR REACTOR*

4.1 Introduction

Gold nanoparticles (Au NPs) and other metallic based nanoparticles (e.g. nickel, silver, palladium, chromium) are synthesized by a variety of methods because of their wide range of potential applications, e.g. drug delivery systems, catalysts, optical sensors, and antimicrobial agents [1-7]. However, the harsh conditions employed in several synthetic approaches has motivated researchers to investigate milder routes to obtain NP [8]. Biological macromolecules such as proteins [9], viruses [10], and plasmid DNA [11] were shown to be successful templates enabling milder pathways for the formation of NPs. To date, the methodologies employing biological reagents present other drawbacks such as lack of size tunability, broad dispersity, and poor shape control; partially due to the tendency of cationic gold to disproportionate in aqueous solutions [12] and issues centered on stabilizing metallic NPs.

We previously demonstrated that the toroidal topology of plasmid DNA is a viable

* This work was submitted to the journal *Nanomaterials*

template or mold for the formation of gold (Au), nickel (Ni) and cobalt (Co) NP. Plasmid DNA it is readily available, inexpensive, and the size of the NP is tunable based on length of the biopolymer and the inner diameter of the toroid [11]. The size of the NP formed also is dictated by several varying parameters that influence the particle formation mechanism, e.g. G-C versus A-T content, and different degrees of topological purity of the plasmid suspensions. The previous report used UV light to catalyze photo-oxidative degradation of the plasmid DNA with the concomitant reduction of the metal ions. Thus, the reproducibility is also dependent on maintaining a specific energy flux during the irradiation time [11].

Herein, we present a complementary synthetic method based on a kinetic approach wherein the plasmid DNA (pcDNA 3.1(+)/GFP, approx. 6 kbps) acts as a template to initiate and control the formation of Au and other metallic NPs by incubation at elevated temperatures. This is an easy to follow procedure that requires less energy, time, and reagents. The size of the Au NPs can be controlled by varying the incubation times (Figure 4.1). Similar procedures allow the preparation of other NP including silver (Ag), palladium (Pd), and chromium (Cr). In this method the metal ions are reduced by oxidative degradation of the amine buffer and/or the DNA at elevated temperatures, and disproportionation reactions for Au, thereby obviating the need for auxiliary reducing agents such as hydrazine and sodium borohydride.

4.2 Experimental Section

4.2.1 Instrumentation and material

UV-Visible. A Beckman Coulter DU800 spectrophotometer was used to collect the UV-visible spectra where 50 μL of each sample was loaded into the cell (8 mm path length). PCR

Eppendorf tubes were used. Silver acetate, cadmium acetonalacetonate, palladium acetate, and tris(hydroxymethyl)-aminomethane (Tris) buffers were from Sigma Aldrich. TE buffer from Quiagen and made of Tris (10 mM) and ethylenediaminetetraacetic acid (EDTA, 1 mM) at pH 8. Tris buffer were 10 mM, adjusted to pH 8. A Lab-Line Multi block heater was used and sample incubated in the dark under an aluminum foil sheet.

Transmission Electron Microscopy (TEM). All data were collected at 120 kV on a Tecnai TEM at the eucentric position ensuring that all measurements and electron diffraction data were accurate for both collection and comparison. The electron diffraction patterns were collected in the microprobe or nanoprobe mode depending on the size of the area to be analyzed. A 7 µL drop of DNA suspension was placed on a 300 mesh carbon coated copper grids, purchased from TED Pella, and allowed to dry for 5 minutes in the dark. The remaining liquid was "whisked" away using a filter paper. The control samples were prepared in the same way with the absence of DNA. The spherical shape of particles was determined by eucentric tilting (over at least an 80 degree range) over the particles from sample 12 h and 15 h. Average particle size was determined by manually counting 50 particles from the TEM images for the gold samples using "imageJ" software.

Gel electrophoresis. 0.8% agarose gels were freshly prepared by dissolving 0.4 g of agarose, purchased from Sigma, in TAE buffer (1x). 2.5 mL of ethidium bromide were added when the mixture was still liquid. After solidification, 10 µL of specific samples were loaded in each of the 10 wells and the gel was run at 85-90 V for the course of 75 minutes.

Plasmid DNA. pcDNA 3.1(+)/GFP was amplified following Quiagen protocols. In order to determine its size as well as the other two plasmids DNA utilized, a sample of each circular plasmid DNA was incubated with ECORI restriction enzyme and linearized. After

running a 0.8% agarose gel, the following sizes were deduced from 1kb standard ladder (purchased from Biolabs): GFP: approx. 6 kbp; pMSCV: approx 7 kbp; pBABEc: approx 6 kbp.

Metal nanoparticles. In a 200 µL PCR Eppendorf tube, 60 µL of a DNA suspension (35 ng/µL in TE buffer, pH 8) was incubated with 10 µL of a solution containing 0.5 wt. % chloro trimethylphosphine-gold (I) in acetone (referred as the gold phosphine solution) in the dark at 70 ^{o}C in a programmable block heater. This method yielded the formation of 6, 8, 9, 11, 18, and 21 nm diameter Au NPs after 1, 2, 4, 7, 12, and 15 hours of DNA/metal cations incubation, respectively (Figures 4.1-4.3). When the incubation time was extended to 21 hours, the water of the DNA suspension evaporated and condensed on the lid of the PCR Eppendorf tube, causing the DNA, as well as other randomly shaped gold structures present

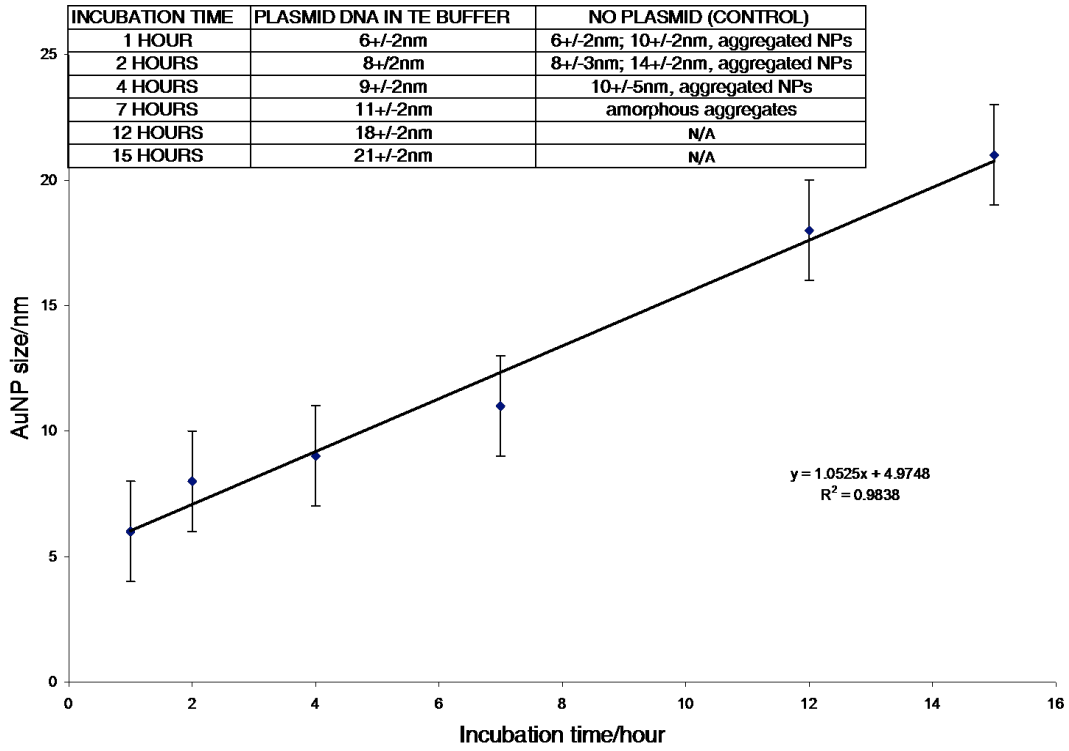

Figure 4.1. Incubation time of the gold phosphine precursor with plasmid DNA versus NP size determined by TEM analysis.

in solution, to aggregate at the bottom of the tube. This aggregation of amorphous DNA and Au material was confirmed by UV-visible spectroscopy [13] (appendix). Control experiments with TE buffer and gold phosphine solution were run in the absence of DNA for 1, 2, 4, and 7 h at 70 ^{o}C, respectively (Figure 2 and 3) and result in randomly sized aggregates. A product yield of 69 % was found for the Au NP formed in the presence of the plasmid, and was calculated via equation 1 below (also see Figure SM-8 for detailed calculations [14]). For formation of the other metallic NP, ethanol solutions containing 0.5 wt % of palladium acetate, chromium acetylacetonate, or silver acetate were used.

4.3 Results and Discussion

The synthetic parameters and trends in NP formation were evaluated with the plasmid DNA and the gold phosphine, and these data were used as a guide to fabricate NP of Ag, Pd, and Cr. UV-visible spetra of the solution from control experiments with only the gold phosphine and the Tris buffer incubated for 1 hour at 70 ^{o}C showed the presence of Au NP (Figure A-4.1), and was similar to those with the plasmid DNA under the same conditions, suggesting that Tris may act as an initial seeding entity. Other amines are known to serve as reducing agent [15-18], and the DNA can serve as a source of electrons at elevated temperatures. Preparations with non-amine buffers such as phosphate do not yield Au NP. UV-visible spectra from the 2 hour and the 4 hour control experiments showed a progressive deminishment of the peak corresponding to the gold absorption as well as an increasing red shift, indicating the formation of larger and more amporphous Au materials. These latter controls confirm that the plasmid DNA is responsible for both the size control and the narrow distribution of the fabricated Au NPs (Figure 4.2 & 4.3). Furthermore, in the absence

of DNA, amorphous gold aggregates were observed after 7 hours of incubation (Figure 4.3). The templating role of the DNA also was deduced from comparing the UV-visible spectra with an analysis of the fate of the DNA by gel electrophoresis (Figure 4.2, 4.3 and A-4.2). After a four hour incubation, the DNAS gels showed a substantial modification of the initial plasmid topology and eventually the DNA is not observed (Figure A-4.2, compare lanes 2 and 10). The UV-visible spectra indicates increased formation of the NP with time, but not an increase in NP size (Figure A-4.8).

The ratio of initial DNA condensation states, supercoiled versus relaxed, dictates the dispersity of the NP products (Figure A-4.2, lanes 2 and 5). Fabrication of narrowly dispersed particles was obtained as the degradation of the DNA progresses, as observed starting around two hours of incubation time with the gold phosphine (Figure A-4.2, lanes 2 and 5). The degraded DNA segments maintain particle dispersion by inhibiting aggregation during incubation, and we cannot exclude the possibility that the DNA from the plasmid surrounds the particle (Figures A-4.7 and A-4.9). The maximum amount of Au NP is reached by seven hours of incubation as revealed by comparison of the UV-visible absorption peaks shown in Figure 4.3A and 4.3B and the TEM (12 h and 15 h). The size tunability of the Au NP versus incubation time was verified by TEM measurements, corresponding to the UV-visible spectra (Figures 4.2 and 4.3).

The metallic nature of the Au NPs was confirmed by superimposing the ED pattern obtained from the experimental samples with that of a gold standard (Figure 4.4). The spherical shape of the Au NPs was determined by eucentric tilting (see experimental and appendix). In order to ensure reproducibility, the concentration of DNA used to yield the Au NPs was kept constant. This was necessary since dilution of the DNA concentration by up to

50-fold, a progressive broadening of the UV-visble spectra of the Au NP was observed. Conversely, a 5-fold increase of DNA concentration yielded less particles (Figure A-4.5). Furthermore, the UV-visible spectra of Au NP from the 50 fold diluted sample containing plasmid DNA, was nearly identical to the spectra of the TE buffer/Au controls, suggesting that a stoichiometric balance between metal salts and DNA substrate is necessary to ensure the narrow dispersity of the NP. After about two hours, the size of the NP increases but the dipersity of the NP narrows, and this is reflected in the UV- visible spectra as a progressive red shift without broadening. This observation is consistent with previous studies corrolating UV-visible spectra with NP size [13]. Nucleation of the nanoparticles initiating inside the toroid in the minor and major grooves of DNA, where cationic binding is often observed [19], may explain the size control of the Au NPs (appendix).

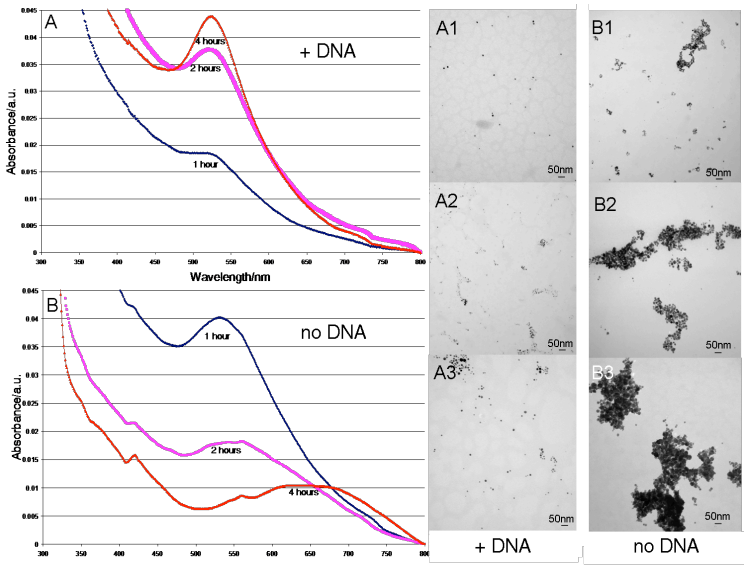

Figure 4.2. A. UV-visible spectra and transmission electron microscopy (TEM) images of DNA-containing samples incubated at 70 ^{o}C in the dark with gold phosphine solution for 1 h (A1), 2 h (A2) and 4 h (A3), respectively. B. UV-visible spectra and corresponding TEM images of TE buffer controls incubated at 70 ^{o}C in the dark with gold phosphine solution for 1 h (B1), 2 h (B2), and 4 h (B3), respectively.

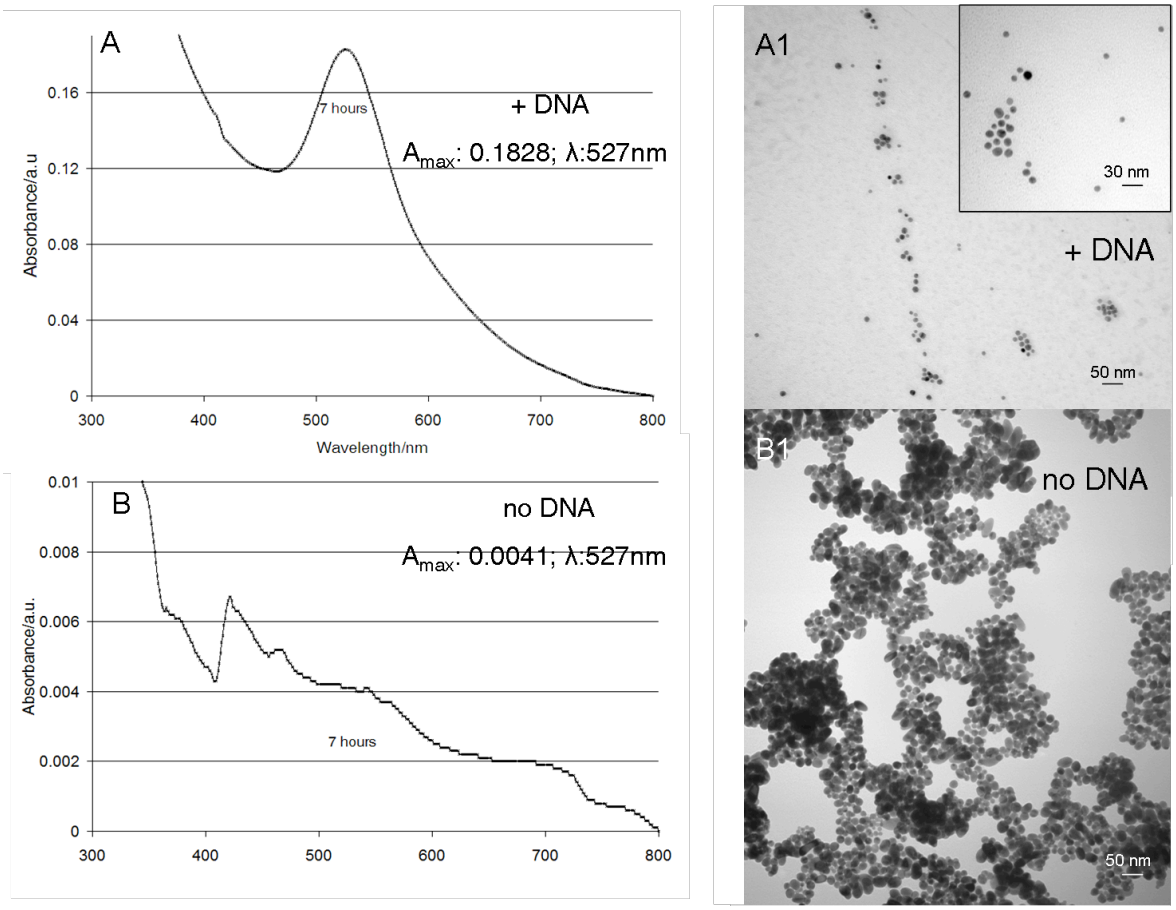

Figure 4.3. A. UV-visible spectrum and corresponding TEM image (A1) of DNA samples incubated with gold phosphine solution for 7 h at 70 ^{o}C in the dark; Inset panel: higher magnification of sample in A1. B. UV-visible spectrum and corresponding TEM image (B1) of TE buffer control incubated with gold phosphine solution under the same conditions

The overall yield of the NP formed can be estimated from equation 1. After a typical 4 h incubation time at 70 ^{o}C, the yield is about 8%, but the yield increases to about 70% after two weeks at room temperature (Figure A-4.8). This indicates that incubation at elevated temperatures initiates the NP formation process. Histograms of the size distribution of the Au NP under several conditions, and the control Tris buffer are shown in Figure 4.8 and 4.9.

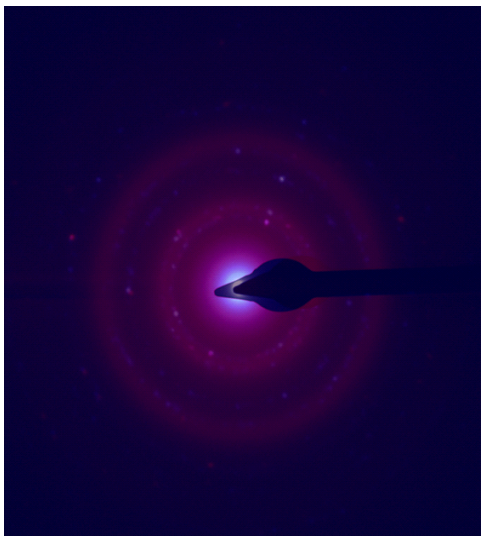

Figure 4.4. ED pattern of gold standard (blue) superimposed on the experimental ED pattern obtained from Au NPs analysis (red) where the overlap indicates the DNA template prepared sample is metallic Au [11].

$$\text{Yield NP: } C_{\text{initial NP}}/C_{\text{synthesized NP}}\ \%$$
$$C_{\text{initial NP}} = N_{\text{tot}}/N_A\ V\ N \qquad (1)$$
$$C_{\text{synthesized NP}} = A/\varepsilon$$

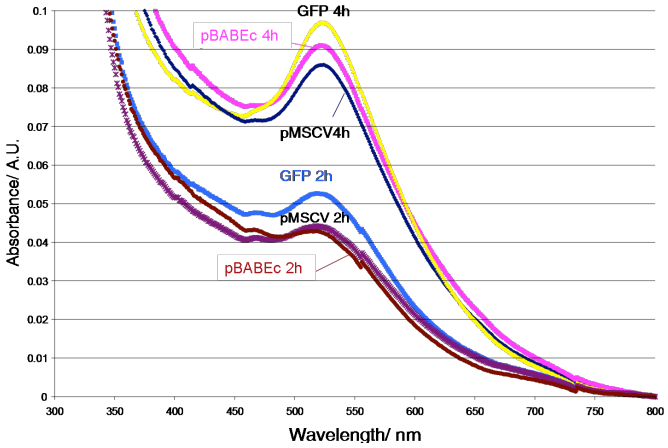

Figure 4.5. UV-visible spectra of three different plasmid DNA samples incubated in the dark at 70 ^{o}C for 2 and 4 hours. The λ_{max} and half-width of the peaks indicate that these plasmids yield Au NPs with similar size and distribution. The spikes at ~550 nm and 740 nm are instrumental artifacts.

4.4 Ag, Pd, and Cr nanoparticles

Metallic nanoparticles of Pd are widely used as catalysts for organic transformations and coupling reactions [20-22]. Silver nanoparticles are exploited as sensors in surface enhanced Raman, and other methods [23-27]. Chromium nanoparticles are proposed for a variety of photonics applications, including in solar energy harvesting [28]. Therefore, facile and greener synthetic methods resulting in narrowly dispersed nanoparticles of these metals are of significant interest. The same procedures and considerations are used to make metallic nanoparticles of Pd, Ag, and Cr. Using our optimized conditions, the plasmid DNA is incubated at 70 ^{o}C between 10 and 17 h depending on the metal ion used. These systems are characterized by, UV-visible spectroscopy TEM, and EDAX (Figures 4.6 and 4.7). These data are consistent with those reported in the aforementioned literature.

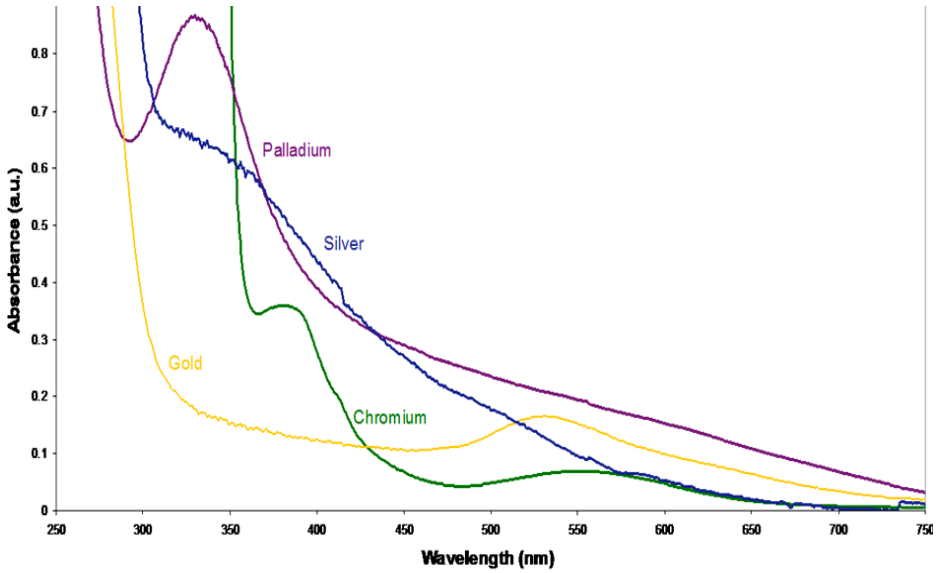

Figure 4.6. The UV-visible spectra of nanoparticles of palladium (purple), silver (blue), and chromium (green) compared to that of gold (yellow) are consistent with date reported previously.

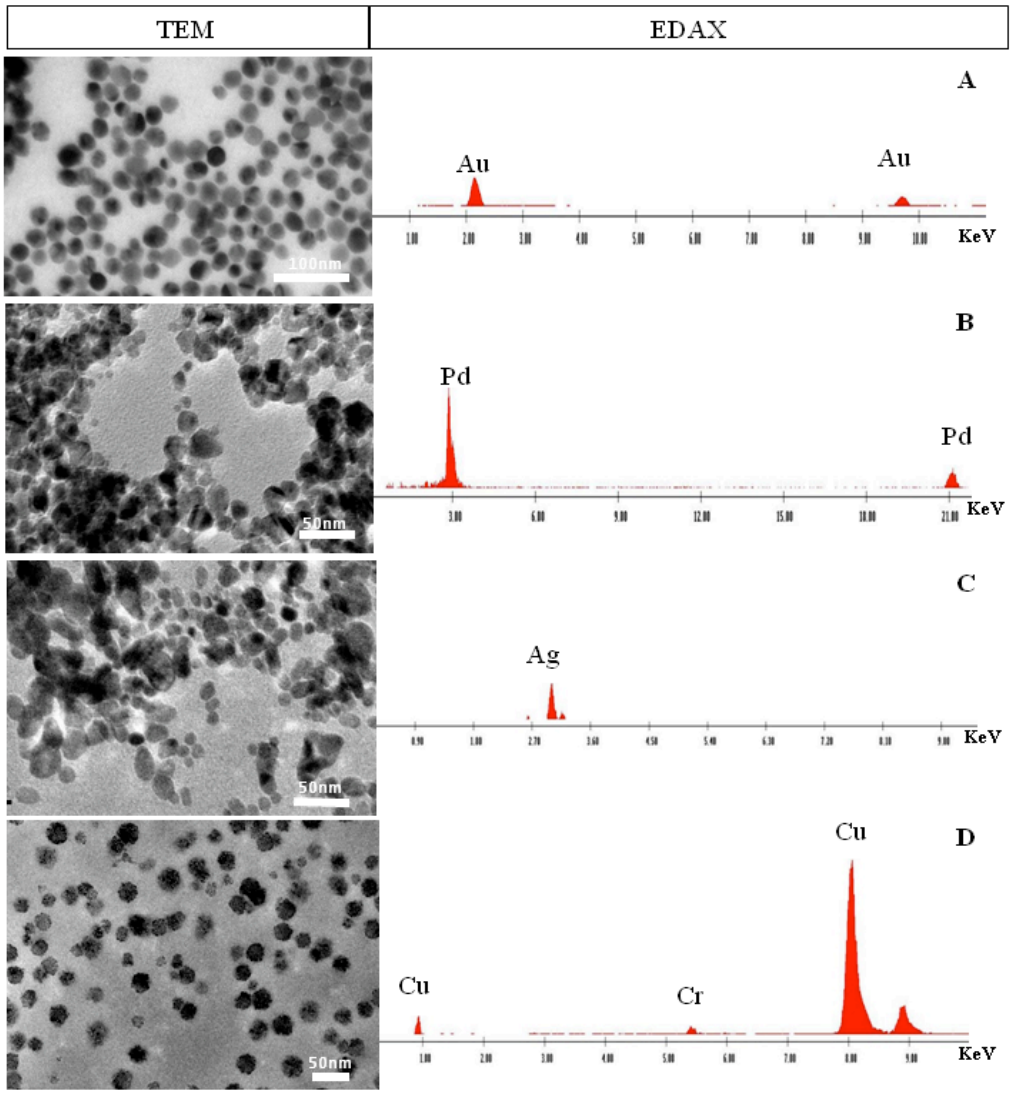

Figure 4.7. (Left) TEM representative images of from top, Au, Pd, Ag, and Cr nanoparticles that were formed by incubation with the plasmid DNA in Tris buffer for 12 h, 17 h, 10 h, and 10 h, respectively. (Right) EDAX Netcounts spectra of the metallic nanoparticles shown (A-C) indicate the composition of the NP. (D) The Cu lines from the carbon coated copper grid shows up in the Cr sample at bottom.

4.5 Conclusions

The results demonstrate the ease of synthesis of size tunable spherical nanoparticles of Au, and narrowly dispersed NP of several types of metals, that exploits the toroid topology of plasmid DNA as a template in concert with the slow oxidation of an amine buffer. While

our previous report used UV light to catalyze the oxidation of the DNA and concomitant reduction of the metal cations [11] herein we employ the application of direct heat to initiate oxidation of the TE buffer to reduce the metal cations. The multi block heater ensures exact temperature control over a predetermined amount of time while using minimal energy. The stabilization of the metallic NP is mediated by the plasmid DNA fragments. These mild synthetic conditions makes this method environmentally more sustainable, while the minimal steps and the variety of possible plasmids with differences in topology and size enables widespread applications and feasibility for the synthesis of metallic NPs.

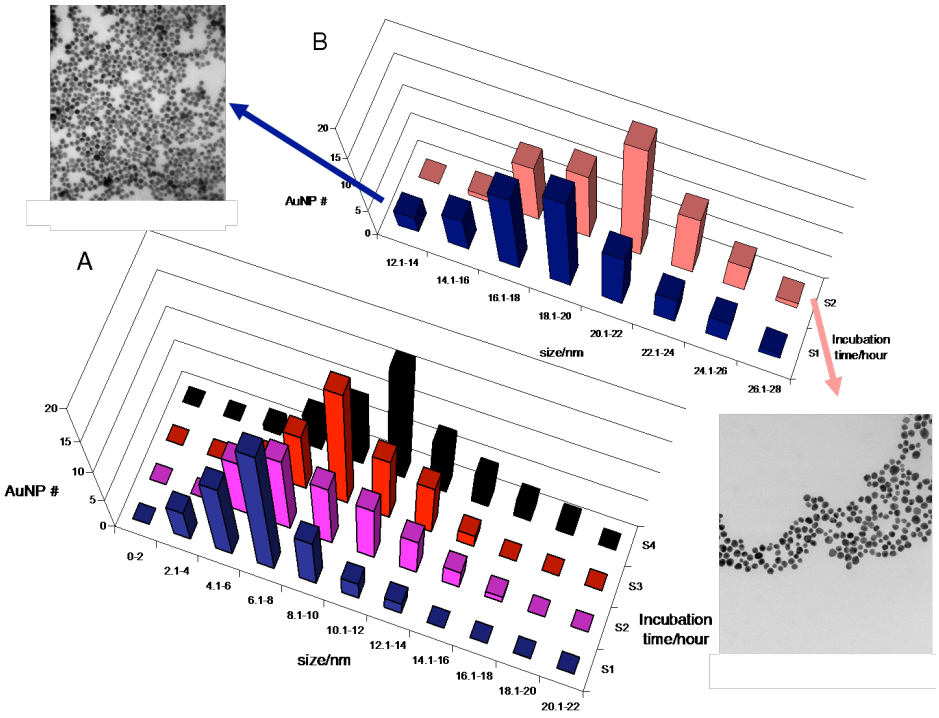

Figure 4.8. Panel A. Histogram of Au nanoparticle sizes corresponding to samples incubated with plasmid DNA in TE buffer for 1 h (S1, blue), 2 h (S2, purple), 4 h (S3, red), and 7 h (S4, black). After 4 h there is a progressive narrowing of the distribution and an increase in particle size that is in agreement with the red shifts observed in the UV-visible spectra (Figures 4.1 and 4.2). Panel B. Histogram of Au nanoparticle sizes corresponding to samples incubated with plasmid DNA for 12 h (S1, dark blue) and 15 h (S2, pink). TEM images of the Au samples from 12 h (dark blue) and 15 h (pink) incubations at 70 ^{o}C.

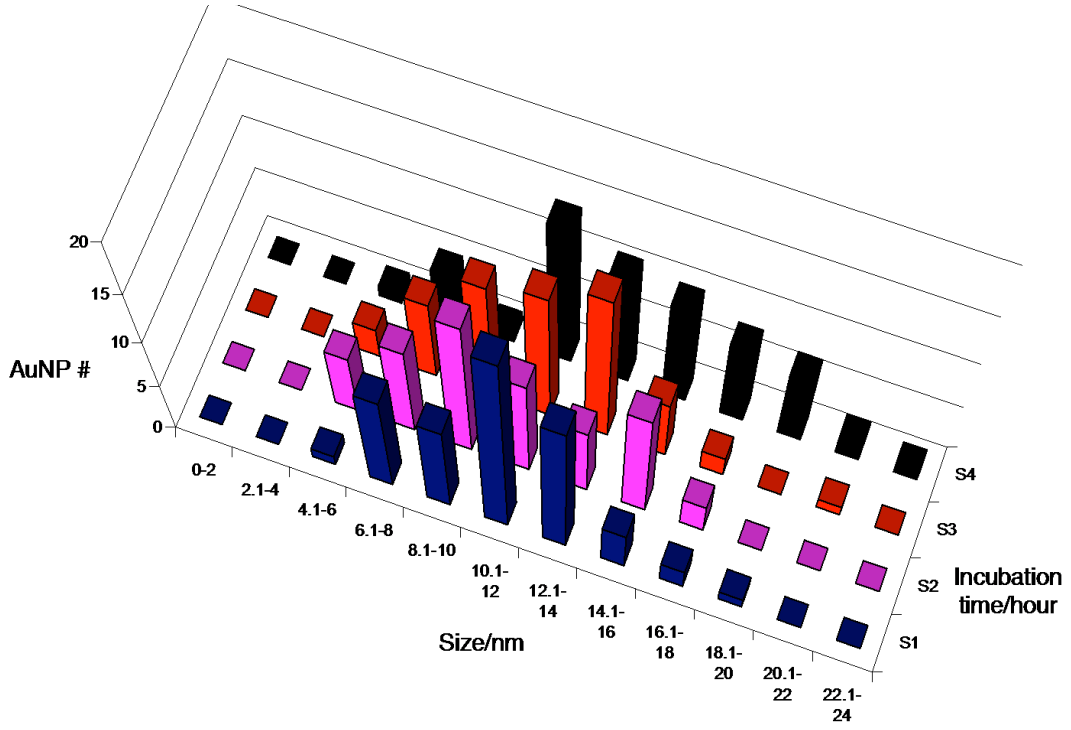

Figure 4.9. Histogram of particle size distributions corresponding to control samples in TE buffer without plasmid DNA incubated for 1 h (S1, blue), 2 h (S2, purple), 4 h (S3, red), and 7 h (S4, black). Despite the high level of aggregation, the particles were still counted individually. The level of particle aggregation was greatest in the 7 h sample (Figure 4.3). No correlation between the NP size and the incubation time was observed.

4.6 References

1. Sun, Y.; Xia, Y. Shape-Controlled Synthesis of Gold and Silver Nanoparticles. *Science* **2002,** *298*, 2176-2179.
2. Wagner, J.; Köhler, J. M. Continuous Synthesis of Gold Nanoparticles in a Microreactor. *Nano Lett.* **2005,** *5*, 685-691.
3. Jana, N. R.; Gearheart, L.; Murphy, C. J. Seeding Growth for Size Control of 5−40 nm Diameter Gold Nanoparticles. *Langmuir* **2001,** *17*, 6782-6786.
4. Shanmugam, S.; Viswanathan, B.; Varadarajan, T. K. A novel single step chemical route for noble metal nanoparticles embedded organic-inorganic composite films. *Mater. Chem. Phys.* **2006,** *95*, 51-55.
5. Hiramatsu, H.; Osterloh, F. E. A Simple Large-Scale Synthesis of Nearly Monodisperse Gold and Silver Nanoparticles with Adjustable Sizes and with Exchangeable Surfactants. *Chem. Mater.* **2004,** *16*, 2509-2511.
6. Martinez-Hurtado, J. L. Metallic Nanoparticle Block Copoloymer Vesicles with Enhanced Optical Properties. *Nanomaterials* **2011,** *1*, 20-30.
7. Tiwari, P.; Vig, K.; Dennis, V.; Singh, S. Functionalized Gold Nanoparticles and Their Biomedical Applications. *Nanomaterials* **2011,** *1*, 31-63.
8. Campelo, J. M.; Conesa, T. D.; Gracia, M. J.; Jurado, M. J.; Luque, R.; Marinas, J. M.; Romero, A. A. Microwave facile preparation of highly active and dispersed SBA-12 supported metal nanoparticles. *Green Chem.* **2008,** *10*, 853-858.
9. Ravindra, P. Protein-mediated synthesis of gold nanoparticles. *Mater. Sci. Eng B-Solid* **2009,** *163*, 93-98.
10. Slocik, J. M.; Naik, R. R.; Stone, M. O.; Wright, D. W. Viral templates for gold nanoparticle synthesis. *J. Mater. Chem.* **2005,** *15*, 749-753.
11. Samson, J.; Varotto, A.; Nahirney, P. C.; Toschi, A.; Piscopo, I.; Drain, C. M. Fabrication of Metal Nanoparticles Using Toroidal Plasmid DNA as a Sacrificial Mold. *ACS Nano* **2009,** *3*, 339-344.
12. Kimling, J.; Maier, M.; Okenve, B.; Kotaidis, V.; Ballot, H.; Plech, A. Turkevich Method for Gold Nanoparticle Synthesis Revisited. *J. Phys.Chem. B* **2006,** *110*, 15700-15707.
13. Haiss, W.; Thanh, N. T. K.; Aveyard, J.; Fernig, D. G. Determination of Size and Concentration of Gold Nanoparticles from UV−Vis Spectra. *Anal. Chem.* **2007,** *79*, 4215-4221.
14. Liu, X.; Atwater, M.; Wang, J.; Huo, Q. Extinction coefficient of gold nanoparticles with different sizes and different capping ligands. *Colloid Surface B* **2007,** *58*, 3-7.
15. Aslam, M.; Fu, L.; Su, M.; Vijayamohanan, K.; Dravid, V. P. Novel one-step synthesis of amine-stabilized aqueous colloidal gold nanoparticles. *J. Mater. Chem.* **2004,** *14*, 1795-1797.
16. Leff, D. V.; Brandt, L.; Heath, J. R. Synthesis and Characterization of Hydrophobic, Organically-Soluble Gold Nanocrystals Functionalized with Primary Amines. *Langmuir* **1996,** *12*, 4723-4730.
17. Newman, J. D. S.; Blanchard, G. J. Formation of Gold Nanoparticles Using Amine Reducing Agents. *Langmuir* **2006,** *22*, 5882-5887.

18. Subramaniam, C.; Tom, R. T.; Pradeep, T. On the formation of protected gold nanoparticles from $AuCl_4^-$ by the reduction using aromatic amine. *J. Nanoparticle Res.* **2005,** *7*, 209-217.
19. Hud, N.; Polak, M. DNA-cation interactions: the major and minor grooves are flexible ionophores. *Curr. Opin. Struct. Biol.* **2001,** *11*, 293-301.
20. Hu, J.; Liu, Y. Pd Nanoparticle Aging and Its Implications in the Suzuki Cross-Coupling Reaction. *Langmuir* **2005,** *21*, 2121-2123.
21. Chandrasekhar, V.; Suriya Narayanan, R.; Thilagar, P. Organostannoxane-Supported Palladium Nanoparticles. Highly Efficient Catalysts for Suzuki-Coupling Reactions. *Organometallics* **2009,** *28*, 5883-5888.
22. Watt, J.; Cheong, S.; Toney, M. F.; Ingham, B.; Cookson, J.; Bishop, P. T.; Tilley, R. D. Ultrafast Growth of Highly Branched Palladium Nanostructures for Catalysis. *ACS Nano* **2009,** *4*, 396-402.
23. Maduraiveeran, G.; Ramaraj, R. Potential Sensing Platform of Silver Nanoparticles Embedded in Functionalized Silicate Shell for Nitroaromatic Compounds. *Anal. Chem.* **2009,** *81*, 7552-7560.
24. Encina, E. R.; Coronado, E. A. Plasmon Coupling in Silver Nanosphere Pairs. *J Phys. Chem. C* **2010,** *114*, 3918-3923.
25. Mitsuishi, M.; Tanaka, H.; Obata, M.; Miyashita, T. Plasmon-Enhanced Luminescence from Ultrathin Hybrid Polymer Nanoassemblies for Microscopic Oxygen Sensor Application. *Langmuir* **2010,** *26*, 15117-15120.
26. Ramesh, G. V.; Radhakrishnan, T. P. A Universal Sensor for Mercury (Hg, HgI, HgII) Based on Silver Nanoparticle-Embedded Polymer Thin Film. *ACS Appl. Mat. Interfaces* **2011,** *3*, 988-994.
27. Wang, W.; Shi, X.; Kariuki, N. N.; Schadt, M.; Wang, G. R.; Rendeng, Q.; Choi, J.; Luo, J.; Lu, S.; Zhong, C.-J. Array of Molecularly Mediated Thin Film Assemblies of Nanoparticles: Correlation of Vapor Sensing with Interparticle Spatial Properties. *J. Am. Chem. Soc.* **2007,** *129*, 2161-2170.
28. Pribik, R.; Aslan, K.; Zhang, Y.; Geddes, C. D. Metal-Enhanced Fluorescence from Chromium Nanodeposits. *J. Phys. Chem. C* **2008,** *112*, 17969-17973.

4.7 Appendix

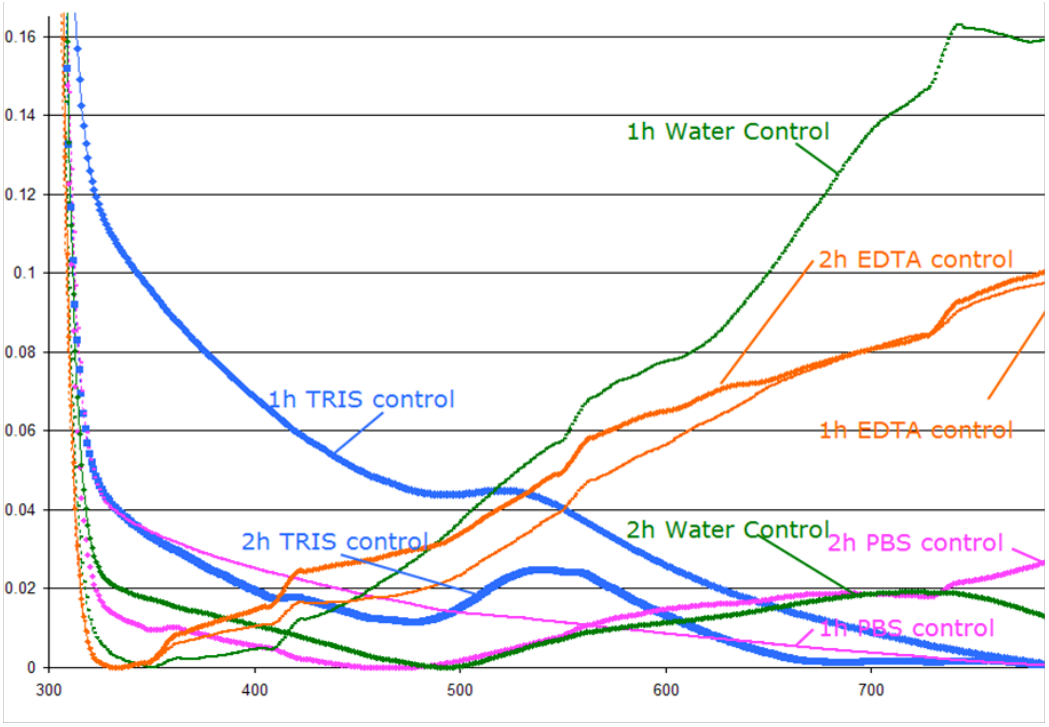

Figure A-4.1. UV-visible spectra of control experiments incubated for 1 h and 2 h at 70 ^{o}C in the dark (water: green; TRIS: light blue; PBS: purple; EDTA: orange). The UV-visible spectra of the Tris controls (corresponding to the incubation times of 1 h and 2 h) resemble the spectra of the TE buffer controls corresponding to the same incubation times (Figure 4.2B) as well as the 1 h incubation DNA/gold (Figure 4.2A).

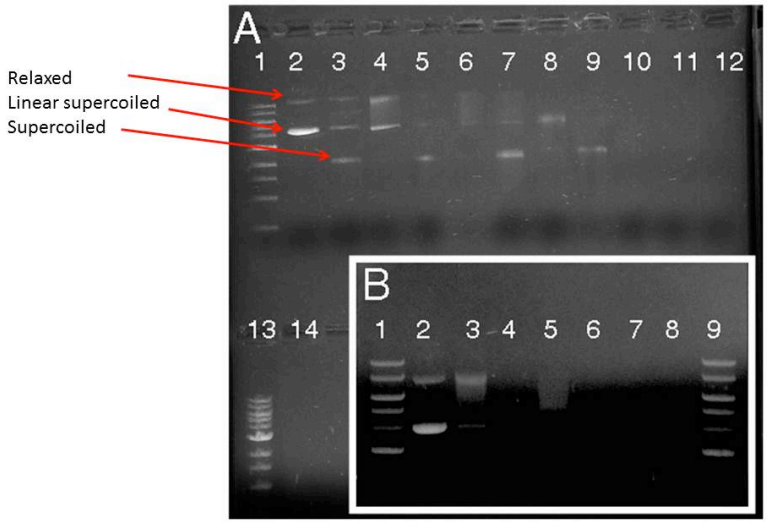

Figure A-4.2. 0.8% agarose gel electrophoresis (GE) of plasmid DNA incubated with gold phosphine solution at different times. The gels were taken on different days (Panel A: same day; Panel B: the next day).

Panel A→ Lane 1: 1 kb ladder; Lane 2: naked pCDNA 3.1 (+)/GFP (GFP); Lane 3: naked pCDNA 3.1 (+)/GFP with rearranged initial topologies (GFPr); Lane 4: GFP after 30 min incubation time; Lane 5: GFPr after 30 min incubation time; Lane 6: GFP after 1 hour incubation time; Lane 7: GFPr after 1 hour incubation time; Lane 8: GFP after 2 hour incubation time. Lane 9: GFPr after 2 hour incubation time; Lane 10: GFP after 4 hour incubation time; Lane 11: GFPr after 4 hour incubation time; Lane 12: GFP after 7 hour incubation time; Lane 13: 1 kb ladder; Lane 14: GFPr after 7 hour incubation time.

Panel B→ 1: 1 kb ladder; Lane 2: Naked pCDNA 3.1 (+)/GFP (GFP); Lane 3: GFP after 30 min incubation time; Lane 4: GFPr after 30 min incubation time; Lane 5: GFP after 1 hour incubation time; Lane 6: GFPr after 1 hour incubation time; Lane 7: GFP after 2 hour incubation time. Lane 8: GFPr after 2 hour incubation time; Lane 9: 1 kb ladder.

Starting from the fourth hour of incubation, either total degradation into DNA segments, or wrapping of DNA template around NP occurs thereby quenching the ethidium bromide, (undetectable by GE: lane 10, 11, 12, and 14). This shows a narrower particle distribution when GFP is the starting templating agent (see UV-visible spectra from Figures 4.2 and 4.3). The presence of the small DNA segments act as an anti-aggregating agent (Figure A-4.8). Furthermore from lanes 8 and 9 (Panel A) we observed the presence of two different main DNA topologies (after 2 hour incubation time) in solution which yielded nanoparticles of similar size

and distribution (compare UV-Vis spectra of GFP 2 h Vs GFPr 2 h from Figure A-4.4). This confirms that DNA acts as a nucleation site and the presence of a specific topology (e.g. toroidal or highly condensed), is not a priori necessary to drive the particle formation under these conditions. On the other hand there are two great advantages in having a well defined initial DNA topological ratio of X to Y: 1) the particles are more stable in solution and do not tend to re-aggregate (GFP 2 h + overnight vs. GFPr 2 h + overnight, Figure A-4.3); 2) Narrowly distributed NP formation is ensured throughout longer incubation times of 4 and 7. The size dispersity is much narrower with the forward topology (Figure A-4.4).

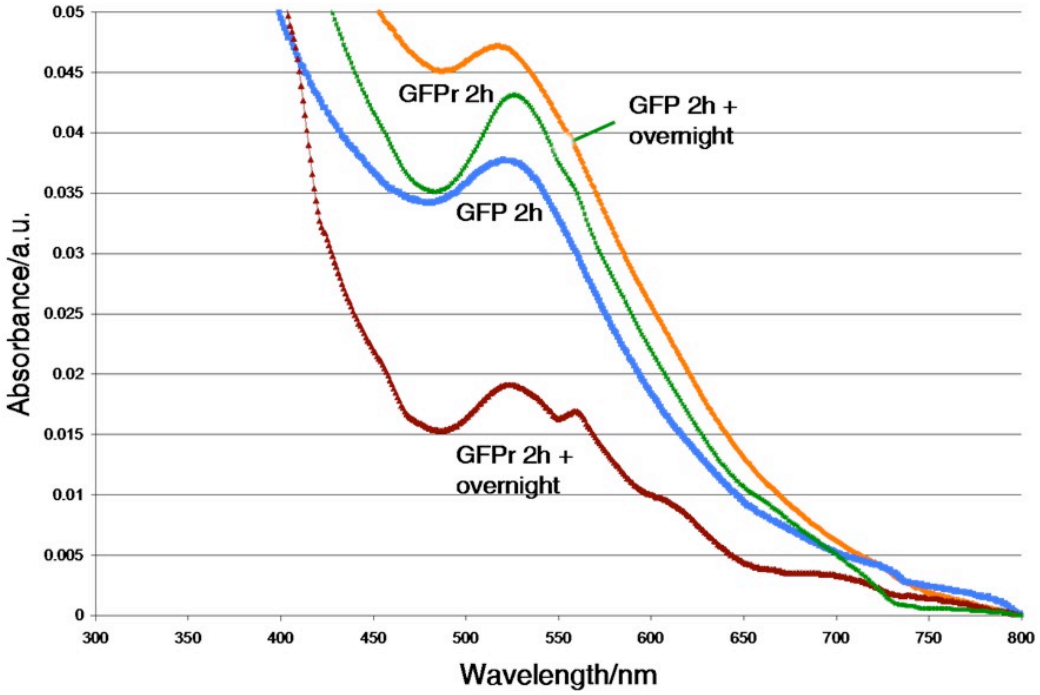

Figure A-4.3. Samples from Figure A-4.2 lane 8 (GFP 2 h) and lane 9 (GFPr 2 h) incubated with gold phosphine at 70 ^{o}C for 2 hours. Spectra "GFP 2 h + overnight" and "GFPr 2 h + overnight" were taken the day after to investigate the effect of initial topologies on the particle formation. Changes in initial topologies (Figure A-4.2, Panel A, lanes 2 & 3) resulted in no significant variation in particle size observed by no red shift. The size distribution is narrower when there is less of the supercoiled GFPr (brown and green lines), was utilized as initial template. This trend continues to be exhibited through longer incubation times (Figure A-4.4).

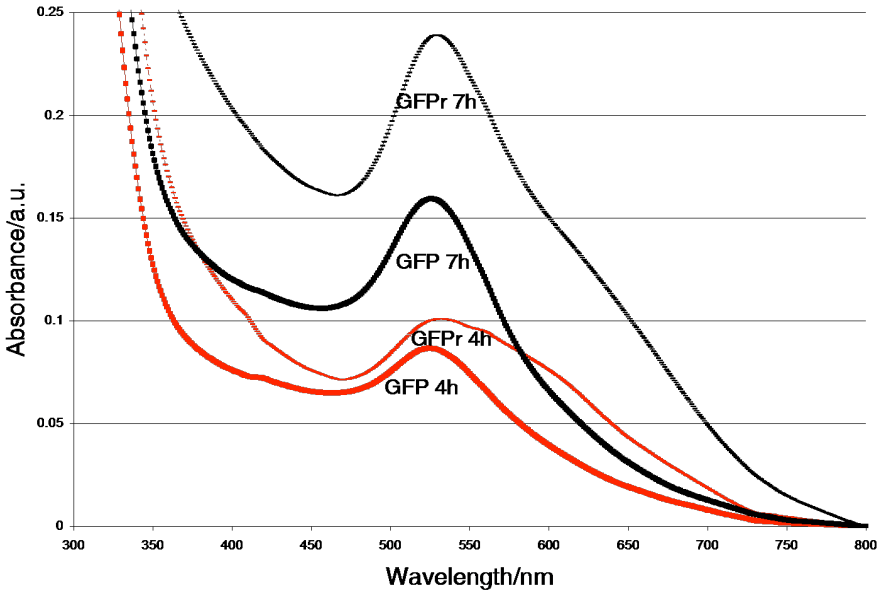

Figure A-4.4. UV-Visible spectra of samples from Figure A-4.2 (Panel A): lane 10 (GFP, 4 h incubation time), lane 11 (GFPr, 4 h), lane 12 (GFP, 7 h), and lane 14 (GFPr 7 h) incubated with gold phosphine at 70 ^{o}C. The emergence of spectral shoulders of GFPr 4 h and GFPr 7 h confirms the necessity of a specific initial DNA topological distribution to ensure narrow size-dispersity of the Au NP.

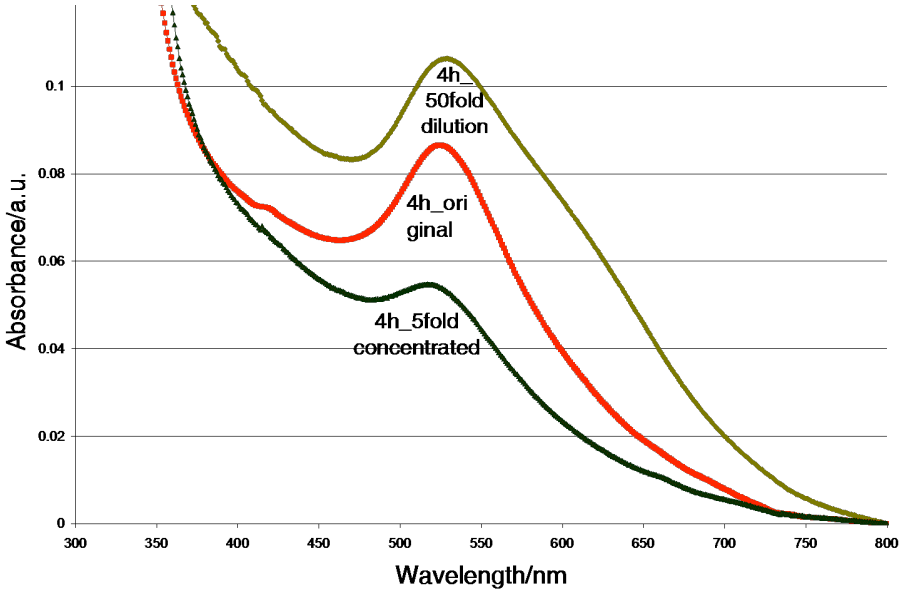

Figure A-4.5. UV-Visible spectra of Au NP prepared from 50-fold diluted, and 5-fold more concentrated GFP suspensions, incubated with gold phosphine for 4 h at 70 ^{o}C. The broadening of the spectra as well as the lower absorbance of the 5-fold more concentrated sample confirms that narrow distribution is dependent on the initial DNA concentration; a stoichiometric balance between gold ions and DNA is therefore necessary for optimized size-control.

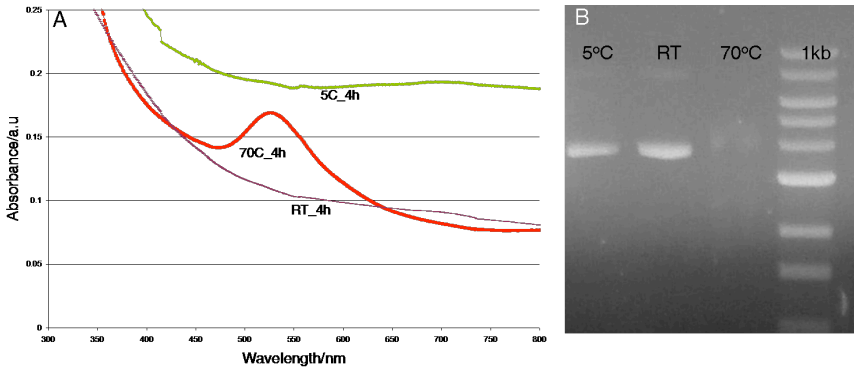

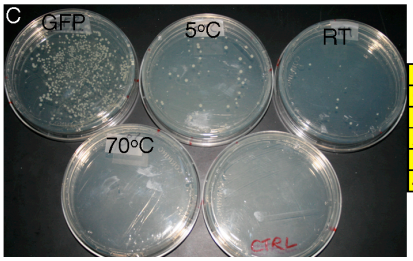

Petri Dish	Colony count
Control	0
1) GFP	480
2) 4h at 5C	47
3) 4h at 27C (RT)	13
4) 4h at 70C	0

Figure A-4.6. Panel A. UV-visible spectra of GFP incubated at 5 ^{o}C, 27 ^{o}C (RT), and 70 ^{o}C for 4 hours. Panel B. gel electrophoresis of samples from Panel A. Panel C: Petri dishes showing bacterial colonies which survived after *E. Coli* transformation. The bacteria which were transformed using the GFP plasmid incubated with gold at 70 ^{o}C did not survive on ampicillin containing plates, confirming the greatest degree of DNA degradation. The absence of bacterial colonies is sign of non-inclusion of the plasmid DNA, which carries the ampicillin resistant gene, in the bacterial DNA. The formation of narrowly dispersed Au NPs ultimately depends on temperature, gold-DNA template interaction, and final DNA fragmentation.

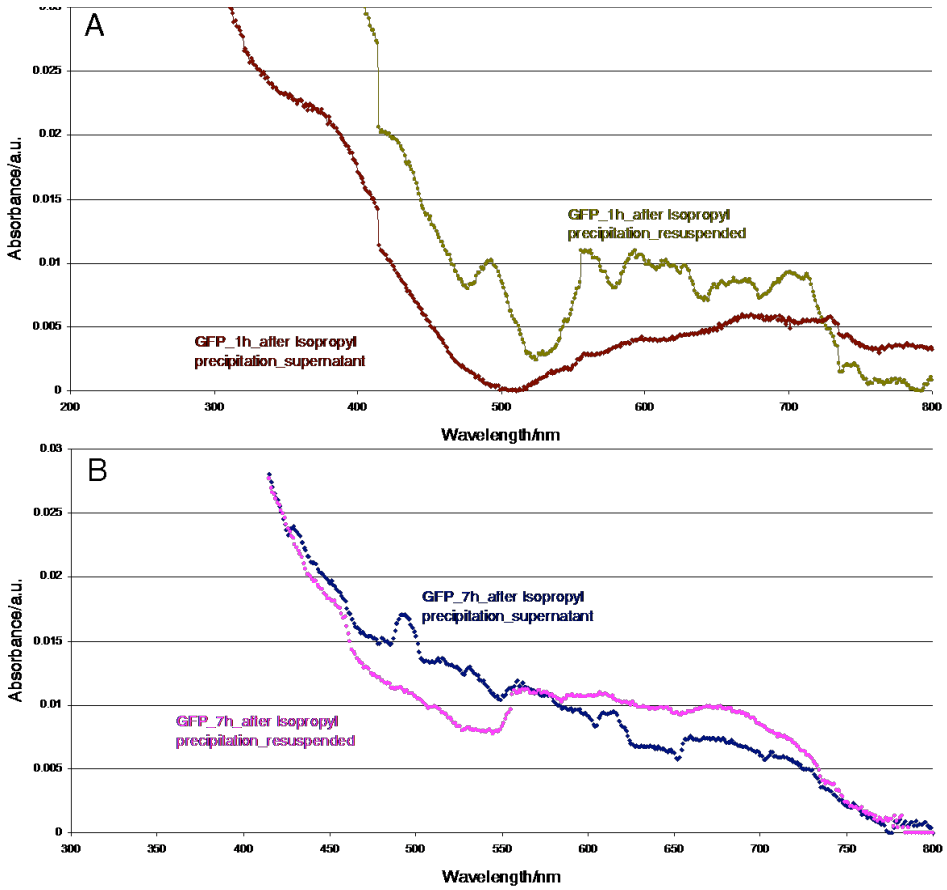

Figure A-4.7. UV-visible spectra of samples incubated for 1 h and 7 h after DNA precipitation with isopropyl-alcohol. This result confirms that the NPs are bound on the DNA template after 1 hour of incubation (see also TEM micrographs in Figure 4.2) and that the DNA fragments, formed upon template degradation, act as anti-aggregating agents. The scattering due to the precipitated DNA results in significant background and the lack of signal due to the Au NP indicates they are in the precipitate.

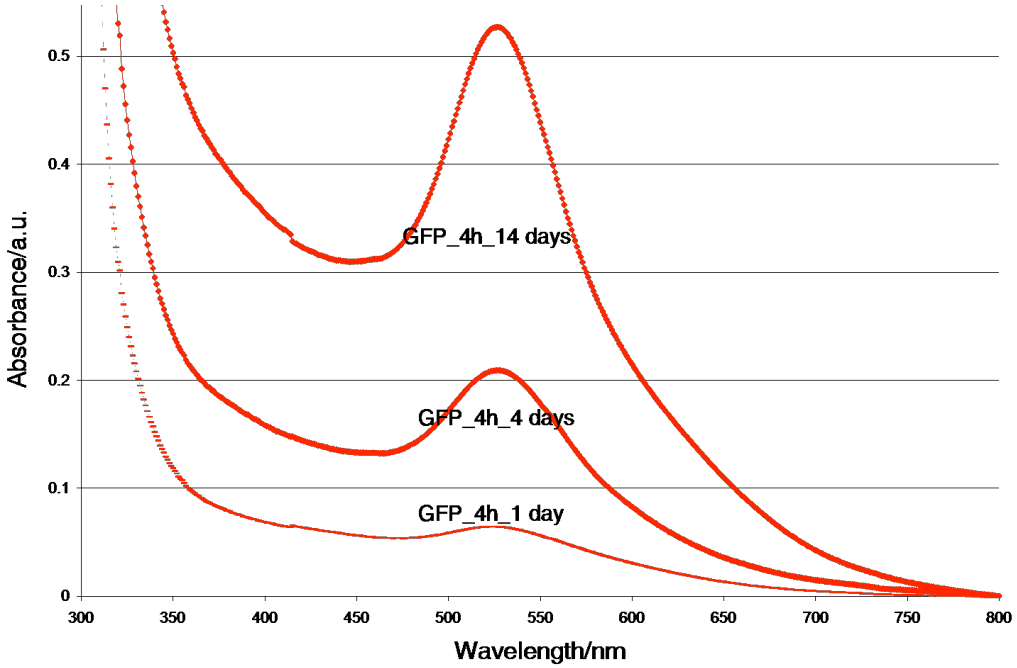

AuNP size	Abs/A.u.	[NP*]	Yield NP/%
9nm	0.0644	4.32×10^{-6} M	8%
	0.2092	1.40×10^{-5}	27%
	0.5267	3.53×10^{-5} M	69%

* $C_{\text{initial NP}} = N_{tot}/N_A \, V \, N = 5.14 \times 10^{-5}$
N_{tot} calculated from initial 0.016g of Au = $8.11 \times 10^{-5} \times N_A = 4.88 \times 10^{19}$
$N_A = 6.02 \times 10^{23}$
$N = 30.89602 \, D^3 = 22523$
Since the $C_{\text{initial NP}}$ is 3444 times bigger than the reference on Table, the ϵ has to be 3444 smaller than the reference ($= 1.49 \times 10^4$)
$C_{\text{synthesized NP}} = 0.2092 / 1 \times 1.49 \times 10^4 = 1.40 \times 10^{-5}$

Yield NP: $C_{\text{inintial NP}} / C_{\text{synthesized NP}}$ %

Figure A-4.8. Top: UV-visible spectra of samples after incubation for 4 h. The samples were allowed to sit at room temperature in the dark for a given amount of time. The yield of the reaction increases up to 69% after 2 weeks. The absence of a red shift confirms that the particles in solution neither re-aggregate nor collapse through time. A high stability in solution is therefore maintained over the course of weeks. Bottom: The table shows the yields calculated based on the absorbance values corresponding to the UV-visible spectra.

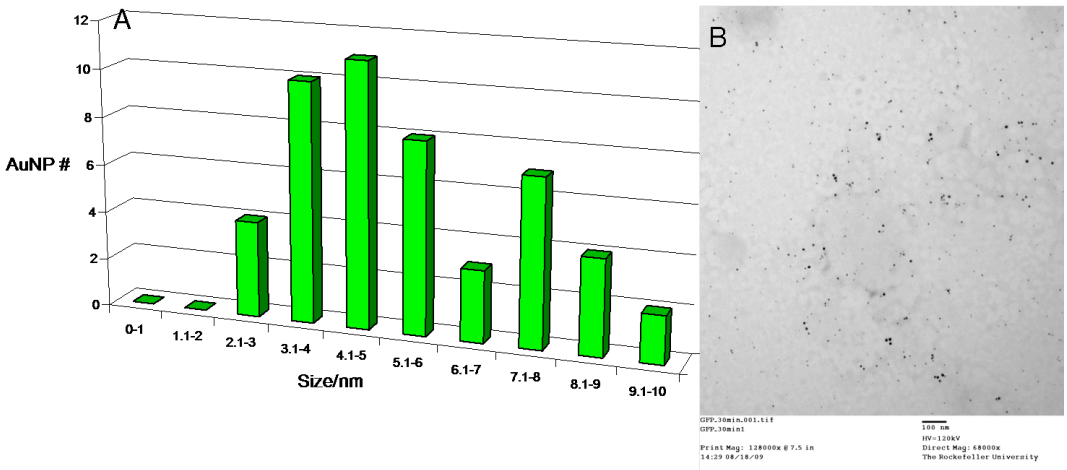

Figure A-4.9. Panel A. Histogram illustrating Au NP size distribution after incubating GFP with the Au phosphine for 30 min. Panel B. TEM image showing that particles are still bound to DNA strands and the bimodal distribution suggests that the DNA major and minor grooves may act as enucleating sites and the overall function of the DNA is that of a bio-molecular reactor.

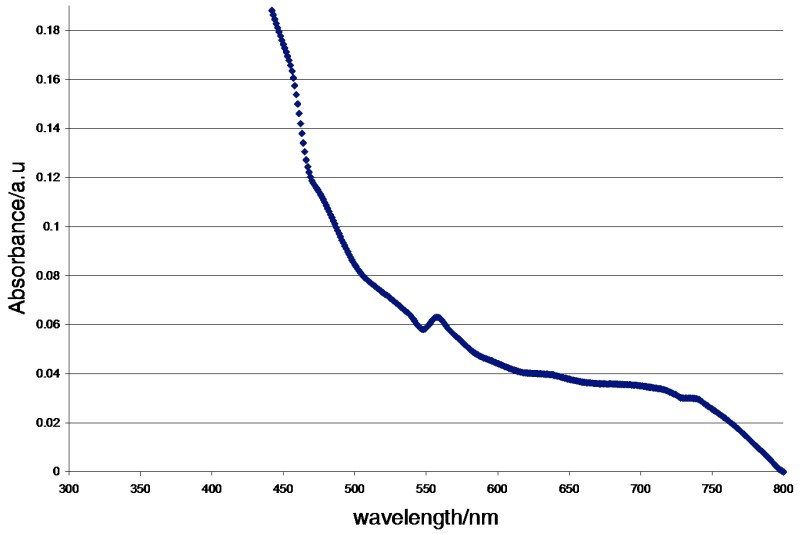

Figure A-4.10. UV-visible spectrum of DNA suspension incubated with gold phosphine solution at 70 ^{o}C for 21 hour until the whole aqueous solution evaporated and condensed on top of the PCR Eppendorf tube. This spectrum shows that in order to fabricate NPs and maintain their stability, an aqueous medium is necessary

Chapter 5

A GREENER SYNTHESIS OF ZINC OXIDE NANOMATERIALS IN WATER BY TEMPERATURE CONTROL OF pH

5.1 Introduction

Zinc Oxide is a non-metallic semiconductor with a wide range of uses and applications. Nearly 100,000 tons of ZnO is used per year as an additive to concrete and rubber tires, as white pigment in paints and glazes (China white), in smaller quantities as a preservative to human and animal food, as UV blocker in sun creams, as anti-inflammatory component in creams and ointments, and as catalysts [1-7]. There are specific properties inherent to ZnO that provide the compound with its versatility. These properties include a wide electron gap, high electron mobility, and transparency [7]. The importance of these physical and chemical properties can be seen directly in their application to the field of transparent electronics [7].

For more than a decade zinc oxide has been the focus of substantial research and development, especially in the synthesis of nanoscale particles, for more precise and dynamic applications. Nanoparticle (NP) fabrication is essential to the advancement of technologies including applications in solar cells [8-11], selective cancer-killing medicines [12], and

photonics [3]. There are a variety of ways to make nanomaterials of ZnO [13-16], many of these methods are cumbersome and/or have a significant environmental impact because they employ harsh conditions, require extensive amounts of time, use high temperature ovens, or use microwave heating [14, 16]. Thus for nanomaterials of ZnO, reducing environmental impact and manufacturing costs remain important objectives. There are several hydrothermal methods [13-15, 17], for example the report by the Vigneshwaran and coworkers employs microwave heating, sodium hydroxide, and overnight drying of the nano-ZnO solutions [18, 19]. Bauermann et al. reported the synthesis of ZnO NPs in 4 h at 37^{o}C, but high temperatures are needed to achieve size tunability of the crystals (i.e. sizes of 18 nm, 27 nm 63 nm, and 290 nm are obtained after the samples were treated at 37 ^{o}C , 80 ^{o}C, 600 ^{o}C, and 1000 ^{o}C, respectively) as well as the removal of interstitial hydrogen [20]. The latter is not necessary for some applications of the synthesized ZnO since hydrogen-doped zinc oxide has also shown to be useful in several technological applications [21-23].

We report herein a simple, scalable hydrothermal method to make ZnO NP that exploits temperature to precisely control the range of pH values of an organic amine buffer. The presence or absence of ethylenediaminetetraacetic acid (EDTA) in the tris(hydroxymethyl)aminomethane (Tris) buffer further modulates the morphology of the ZnO nanomaterials since both compounds can serve as nucleating sites, and as stabilizing agents that prevents agglomeration. This method ameliorates some of the environmental impacts of producing ZnO nanomaterials by reducing both energy and materials consumption.

5.2 Experimental Procedures

5.2.1 Materials

Zinc nitrate hexahydrate, Tris, were purchased from Sigma Aldrich. 1X TE buffer (EDTA containing buffer) was purchased by Fisher. Deionized nanopure (Millipore) water was used to prepare a 50 mM solution of zinc nitrate hexahydrate and a 100 mM solution of Tris buffer to which HCl was added until a final pH value of 7.92 was reached. The pH of the deionized nanopure water that was used to prepare all the solutions had a value of 7.11 (Orion pH meter). The solvent mixture of the two reactants had a pH value of 7.74 at 25 ^{o}C. See table 5.1 for details regarding the order of the reactants mixing and the procedural steps.

5.2.2 Instrumentation

Transmission Electron Microscopy (TEM). Data were collected at 200 kV on a Jeol 2100. The Jeol 2100 was equipped with an EDAX detector. X-Ray energy dispersive (EDS) analysis data were collected at minimal dead time (0-10) and count/seconds (<1000). This was performed to optimize signal to noise ratio. Only net-counts (sample – background see Figure 5.10) were considered. A 10 μL drop of the aqueous ZnO NP suspension was placed on a 300 mesh carbon coated copper grid, (TED Pella Inc.), and allowed to dry for 1 minute. The remaining liquid was removed away using a filter paper. The control samples were prepared in the same way. The shape of particles was determined by eucentric tilting (over at least an 60^{o} range) over the particles. Average particle sizes were determined by counting 50 particles from the TEM images for the NP samples using "imageJ" software (NIH).

UV-Visible. Beckman Coulter DU800 UV-visible spectrophotometer was used to collect the electronic spectra on 50 μL samples in 8 mm path length cells.

Photoluminescent Spectroscopy. Fluorescence spectra were taken on a Spex Tau-3 fluorometer in 1 cm quartz cuvettes in right angle mode.

Dynamic Light Scattering (DLS). 20 μL of the desired sample was diluted with nanopure water (ratio of 1:1), sonicated for ten seconds, loaded into a 3 mm cuvette and finally run in a Precision Detectors equipped with PDDLS/Batch and PDDLS/CoolBatch 90T System **(***PrecisionDeconvolve*[32] software)

X-ray Diffraction (XRD). All data were collected on a Bruker AXS D8 DISCOVER GADDS with VÅNTEC-2000 Micro-Diffractometer. Samples were prepared under a light microscope by attaching on a loop small crystals of the desired ZnO nanopowders.

Micro scale synthesis	**mL scale synthesis**
To an Eppendorf PCR tube add:	to a 7 mL amber vial add:
10 μL deionized nanopure water (pH 7.11)	0.5 mL deionized nanopure water
10 μL zinc nitrate (50 mM)	0.5 mL zinc nitrate (50 mM)
30 μL Tris (100 mM)	1.5 mL Tris (100 mM)
20 μL deionized nanopure water (pH 7.11)	1.0 mL deionized nanopure water
Incubate at 80 ^{o}C in a multiblock heater for 4 min to 32 min	Incubate at 80 ^{o}C in a multiblock heater for 4 min to 32 min
Remove at time corresponding to desired NP size	Remove at time corresponding to desired NP size
Centrifuge for 30 s, remove supernatant	Centrifuge for 30 s, remove supernatant
Allow to air dry	Allow to air dry

Table 5.1 Zinc oxide synthesis procedures

5.3 Results and Discussion

The overall objective was to design a synthetic method for ZnO that reduces the environmental impact, minimizes processing steps, yields size-tunable nanomaterials, and is amenable to scale-up. The strategy is based on the established temperature dependence of the pH

amine buffers; e.g. Figure 5.1 shows that the pH of the reaction mixture from a mL sized procedure where the pH is 7.9 at 25 ^{o}C and after 4 minutes of incubation at 80 ^{o}C it drops to ~6.8. This is consistent with what is observed for 50 mM Tris [24]. Upon cooling, the solution returns to basic pH, thereby driving ZnO formation. Other parameters affecting the morphology and properties of ZnO nanomaterials include the choice of complexing ligand such as EDTA, the counter-ion of the zinc(II) reagent, pH, temperature, and ionic strength [13, 25].

Bauermann et al. proposed a mechanism for the nucleation and growth of ZnO nanoparticles in which the dissolved precursor, zinc nitrate hexahydrate, forms aquo complexes wherein hydroxide ions initially coordinate the Zn^{2+} cations and an olation-type reaction takes place as the pH increases [20]. In their procedure the ZnO NP forms upon heating and the small temperature difference (~25 to 37 ^{o}C) corresponds to a small change in pH of the Tris buffer, so the reaction is not driven by pH. Since the NP size and morphology are the same at both temperatures, the amine in this case may serve to dictate particle growth [14].

In our study, the reaction that converts zinc nitrate into zinc hydroxide and finally into ZnO or Zn(H)O [20] is likely driven by the drastic *decrease* in pH value at higher temperature. In addition, the complex equilibriums and kinetics involved in the olation chemistry at 80 ^{o}C affect the pH of the reaction mixture, which shows marked time dependence: from a pH of about 7.5 after 1 minute of incubation time to about 5.9 after 16 minutes (Figure 5.1B). Overall the sizes of the NPs were observed to range from ~13 nm to ~20 nm according to the different incubation times (from 2 to 32 minutes). The result is a nearly 100-fold change in $[H^{+}]$ over this time. For the resulting NP size, there is a roughly 1 nm diameter increase for every 2 minutes (Figure 5.1A). After 16 minutes, the pH reaches an asymptote of about 5.7, which may explain the

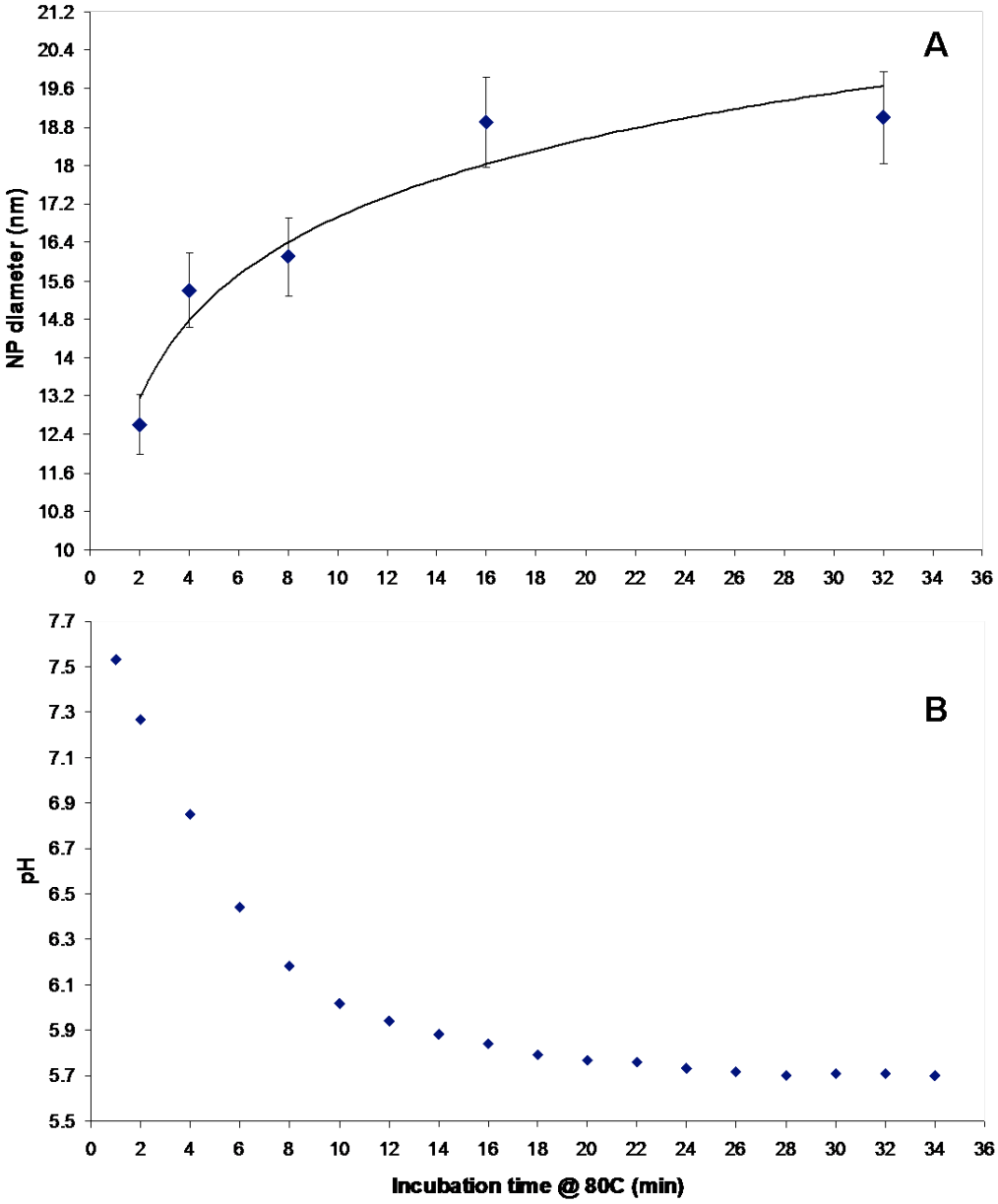

Figure 5.1. Graph showing (A) the ZnO NP diameter progressive increases with incubation time at 80 ^{o}C (error bars represent ± 5% dispersity) and (B) the pH decreases with incubation time at 80 ^{o}C. This illustrates that the incubation time, which dictates the pH, can be used to determine the size of the ZnO NP from about 12 nm to 20 nm under these conditions.

minimal change in NP size after this time (18.9 ± 2.3 nm after 16 minutes to 19.0 ± 2.3 nm after 32 min.

This method demonstrates the ability to finely tune the size of ZnO NP by controlling the incubation time at constant relatively elevated temperature.

Both the time-dependent acidification of the solution and the decreasing concentration of the starting zinc nitrate reagent left in solution may account for the upper limit of the ZnO NP size at about 20 nm. TEM images (Figure 5.2), DLS data (Figure 5.3), UV-visible spectra (Figure 5.4), and calculation using the Scherrer's equation from the XRD data (Figure 5.5, Table 2) are in excellent agreement with each other. In addition, the progressive red shift in the UV-

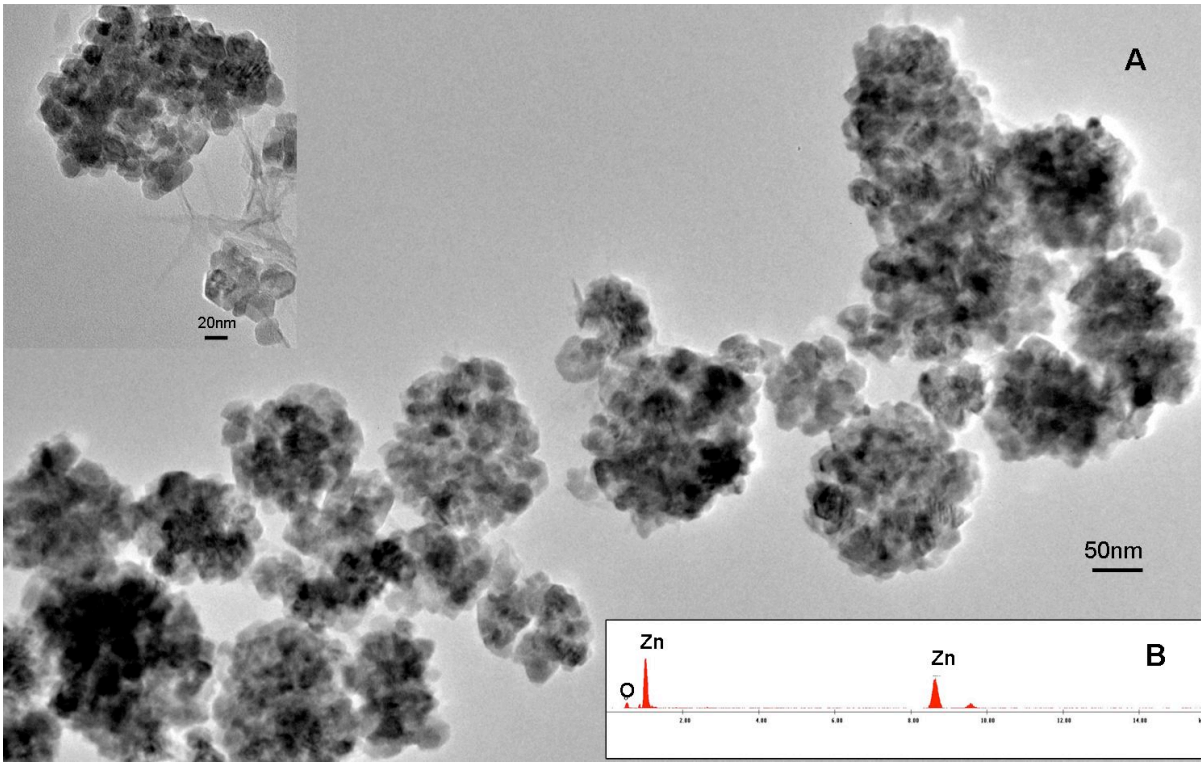

Figure 5.2. (A) TEM images of ZnO NPs formed by incubating the solution at 80 ^{o}C for 8 min in a microscale reaction. In upper left inset, NPs from a 32 min incubation sample is shown from a milliliter scale reaction. Even though ZnO NPs, as many other transition metal oxides, may undergo structural changes under the 200 kV electron beam, the hexagonal morphology it is still observed [27]. The drying effect of the liquid dropped onto the grid might also contribute to this reaggregation. (B) EDAX Netcounts of the material in panel A.

visible spectra corresponds to the increasing in NP diameter from the longer incubation times (Figure 5.5) [26].

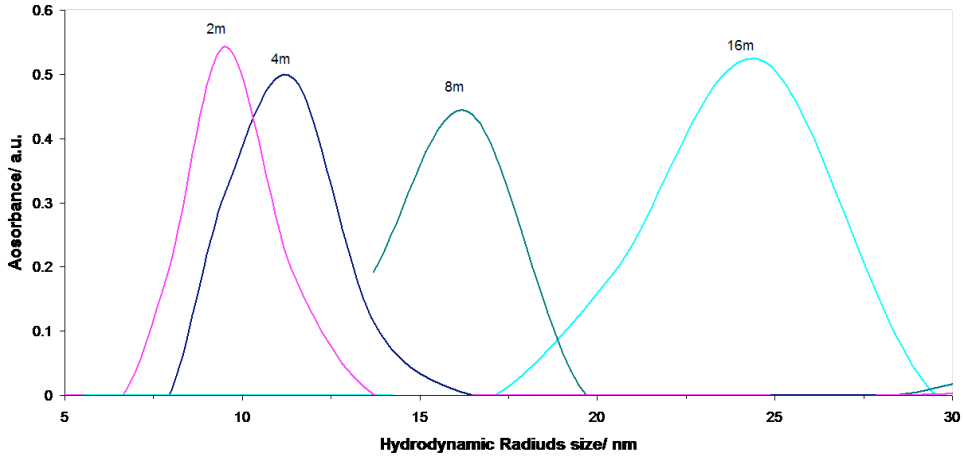

Figure 5.3. DLS data showing the size distribution of the ZnO NP after 2 m (violet), 4 min (blue), 8 min (aqua), and 16 min (light blue) of incubation time at 80 ^{o}C in a micro scale reaction. Note that the hydrodynamic radius of the NP increases with incubation time. The sizes are convolved with the solvation of the NP by water and the components of the TE buffer. This trend is in agreement with the red shift observed in the UV-visible spectra in Figure 5.5.

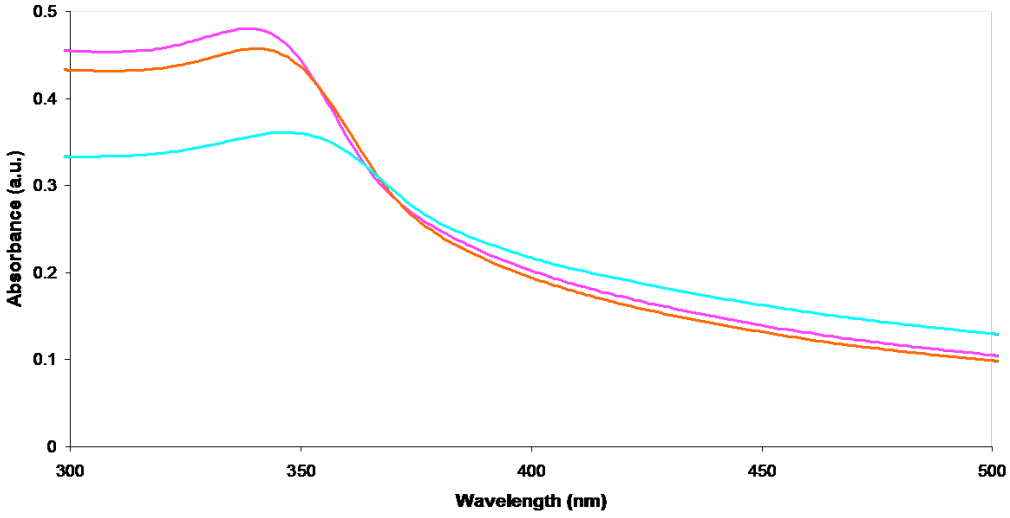

Figure 5.4. UV-visible spectrum of ZnO NPs synthesized at 80 ^{o}C after 4 min (violet), 8 min (orange), and 16 min (light blue) of incubation time in a micro scale reaction. The progressive red shift is in agreement with the XRD and the DLS data; confirming the size dependence of the NP products with different incubation times.

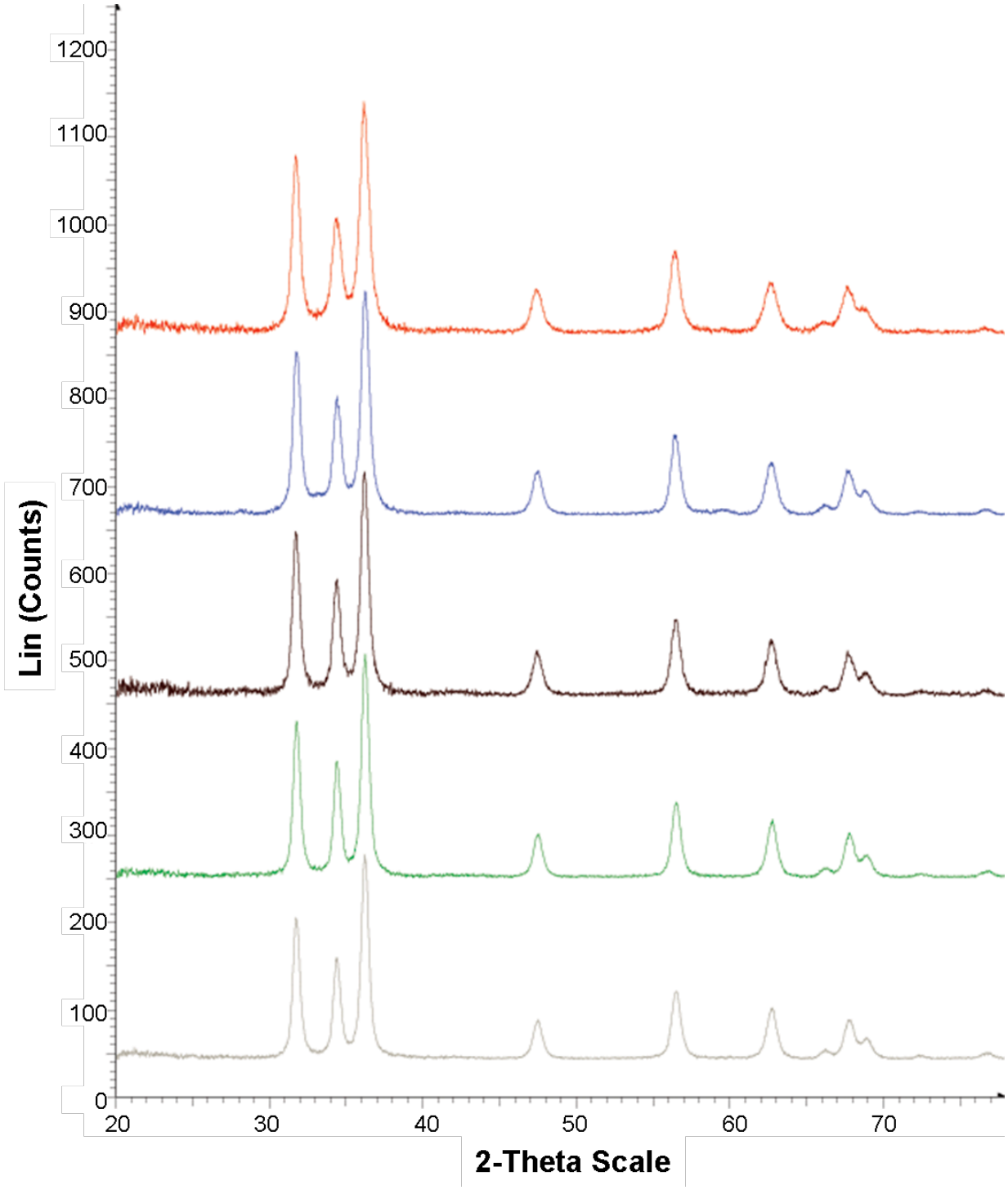

Figure 5.5. XRD spectra showing that the zincite crystal structure of the ZnO NP formed after 2 min (red), 4 min (blue), 8 min (maroon), 16 min (green), and 32 min (grey) of incubation time at 80 ^{o}C in a micro scale reaction. The calculated sizes from the spectra using the Scherrer equation are 12.6 ±1.9 nm, 15.4 ±2.2 nm, 16.1 ±2.2 nm, 18.9 ±2.3 nm, and 19.1 ±2.3 nm, respectively. See Table 2 for X-Ray diffraction analysis of ZnO NP synthesized at 80 ^{o}C.

Incubation at 80 °C (m)	*a*(Å)	*c*(Å)	*V*(Å^3)	*D* (nm)	10^3e
2	3.2465(91)	5.203(15)	47.50(30)	12.5(19)	1.9
4	3.2445(69)	5.200(11)	47.40(23)	15.4(22)	2.2
8	3.2399(76)	5.192(12)	47.20(25)	16.2(24)	2.2
16	3.2397(47)	5.1909(75)	47.18(15)	18.9(23)	2.3
32	3.2393(44)	5.1910(70)	47.17(14)	19.1(23)	2.3

Table 5.2. XRD analysis. The numbers in parenthesis are related to standard deviation (STD). Although some of the STD may appear large, this is representative of characteristics of nano particulate nature which exhibits broad peaks.

5.4 Scale-up of ZnO NP

The objective of the following experiment was to significantly increase the scale of the aforementioned synthetic strategy for ZnO NP, and is an indication that this is a practical, economic, and environmentally friendly method for industrial production of these materials. The strategy adopted was based on the above synthesis, but used TE buffer (10 mM Tris and 1 mM EDTA) instead of only Tris in nanopure water (See Table 5.1) [13]. TE buffer was used because the polydentate molecule EDTA was expected to bind to a crystal face as a means to control the growth of the ZnO NP into hexagonal plates (see below) [13].

In order to demonstrate the advantages of this method compared to other syntheses yielding commercial ZnO powders, it is necessary to evaluate several products through TEM, UV-visible, and photoluminescence (PL) spectroscopy to compare our product with the commercially available ZnO nanopowders. The UV-visible results show a distinct and quantifiable difference in the spectra near 360 nm (Figure 5.6 and 5.7). A narrow absorbance peak in the UV region is typical of a morphologically homogeneous ZnO nanoparticle solution [26], and provides evidence for uniformity in the crystalline structure. The UV band is quite broad in one of the commercially available powders of ZnO (Fisher, Figures 5.6), while the absorption peaks at 375 nm is narrower in for the material from Sigma-Aldrich (Figure 5.7). The latter is about 15 nm to

the red compared to the NP of ZnO fabricated herein (Figure 5.7). Comparative photoluminescent spectra (Figure 5.6 and 5.8) were also taken, and a substantial difference was observed in the 500-530 nm range, providing additional evidence that the ZnO NP formed in by our new method are generally of similar or better uniformity and size.

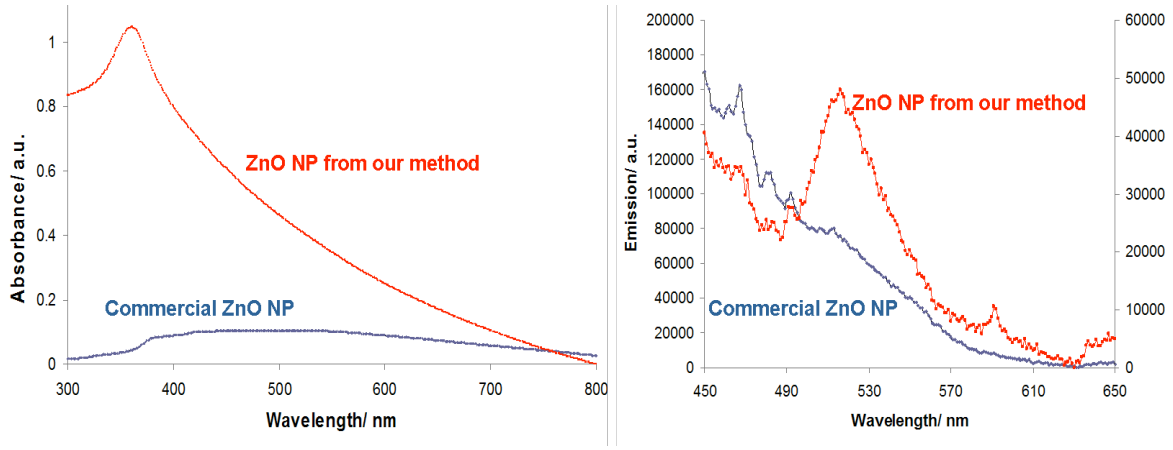

Figure 5.6: Left: UV-visible spectra comparing commercial ZnO nanopowder in water (blue, from Fisher) to the ZnO NP products from our method water (red); Right: photoluminescence spectra of the same Fisher ZnO nanopowder in water (blue) compared to photoluminescence of the ZnO NP from our synthesis (red).

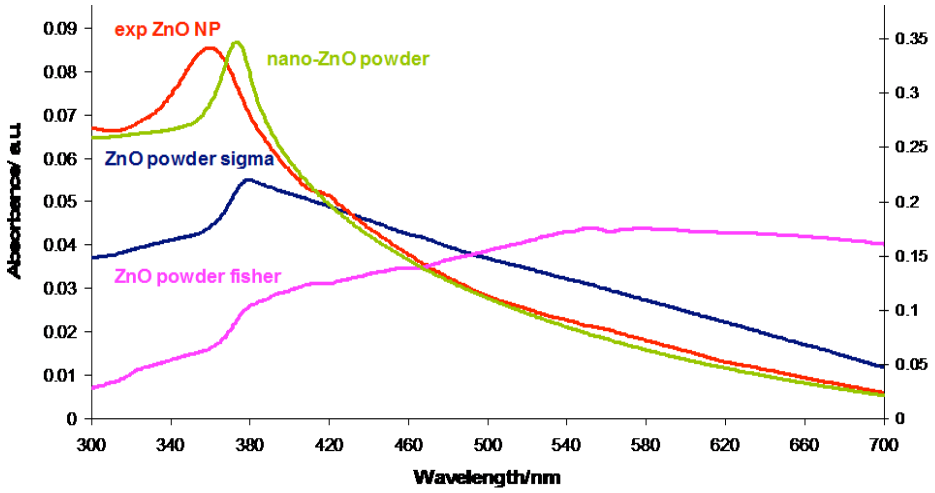

Figure 5.7. UV-visible spectra of different ZnO materials: experimental ZnO NP (red); Sigma-Aldrich ZnO nanopowder (lime); Sigma-Aldrich ZnO powder blue); Fisher ZnO powder (purple). Scale on the right is referred to the Sigma-Aldrich ZnO nanopowder (lime).

Finally, comparisons of the Fisher versus experimental ZnO products (Figures 5.9 & 5.10) through TEM provided objective evidence for morphological homogeneity of the NP formed in our synthetically produced material. Images taken from experimental samples showed hexagonal, puck-like nanostructure as well as a bimodal distribution. The Fisher ZnO nanopowder, however, contained a multitude of crystalline structures and no discernable uniform size distribution.

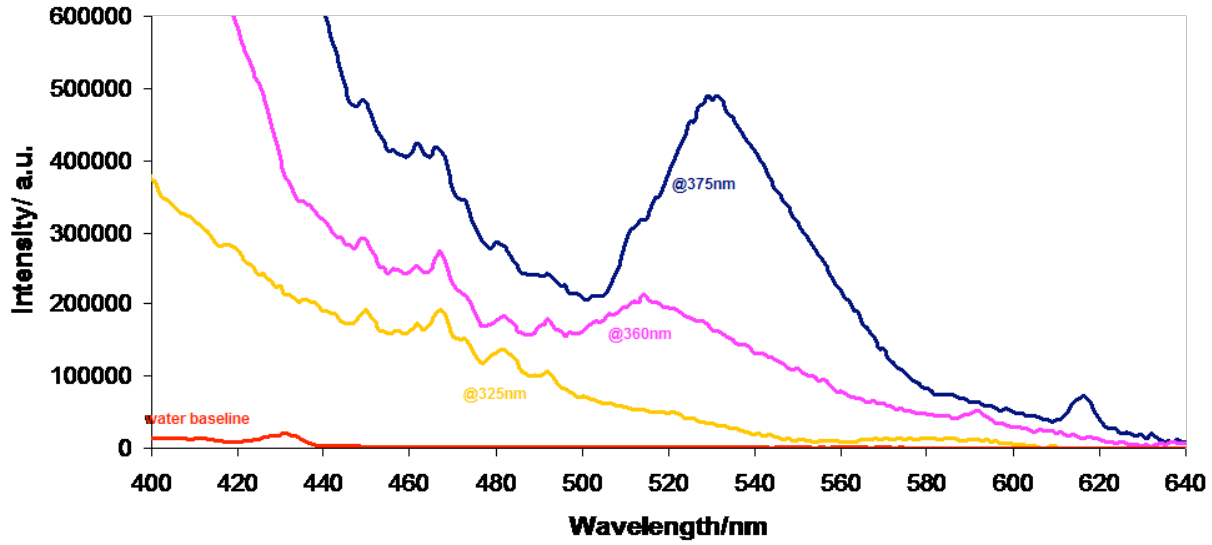

Figure 5.8. Photoluminescence spectra of experimentally fabricated ZnO NP with excitation wavelengths of 325 nm, 360 nm, and 375nm.

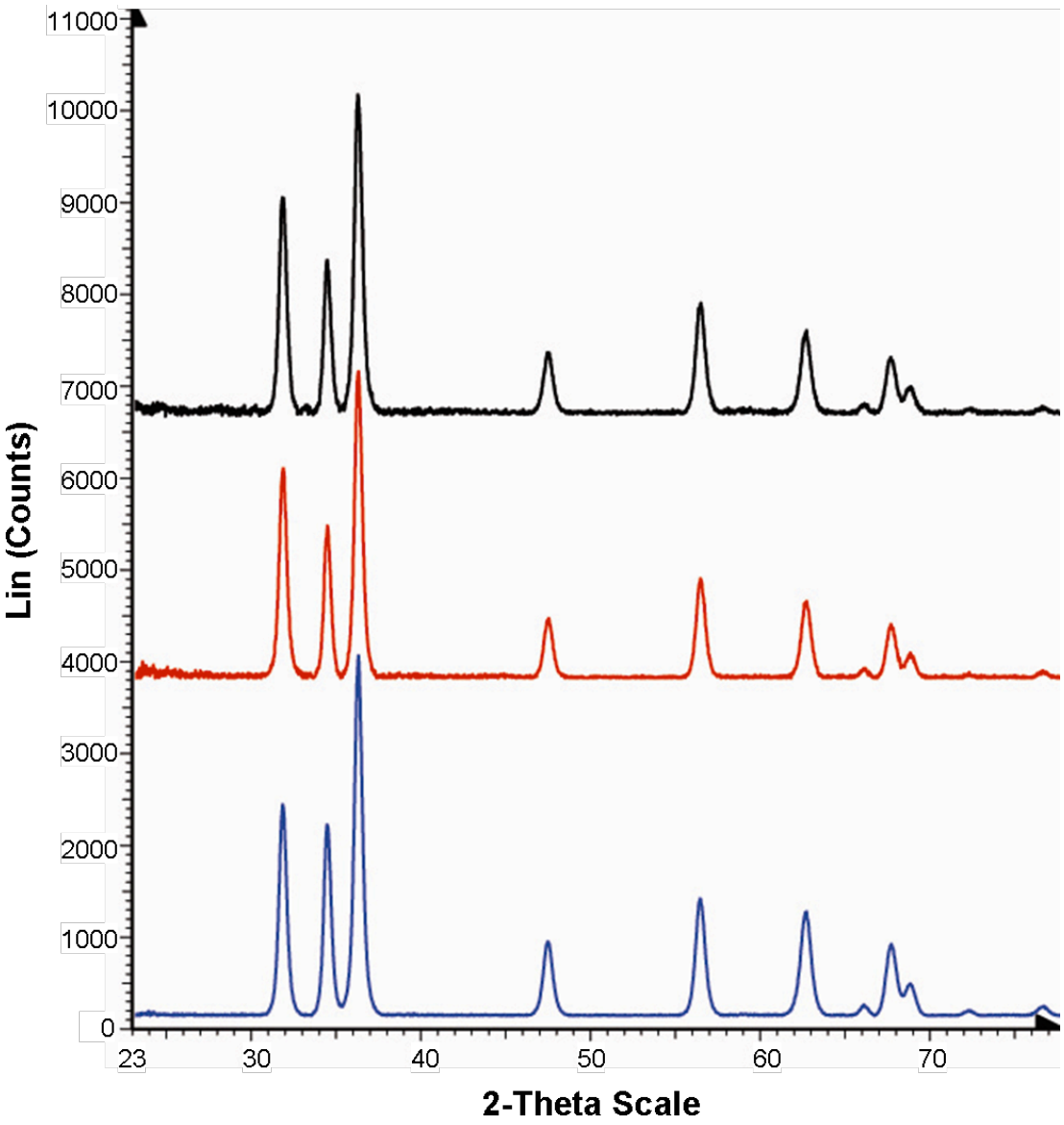

Figure 5.9. XRD spectra showing that the zincite crystal structure of the ZnO NPs after 4 min (blue), 30 min (red), and 60 min (black) of cooling down time (after 4 min incubation at 80 ^{O}C), does not change. This crystalline uniformity is consistent with the experiments done in the microscale.

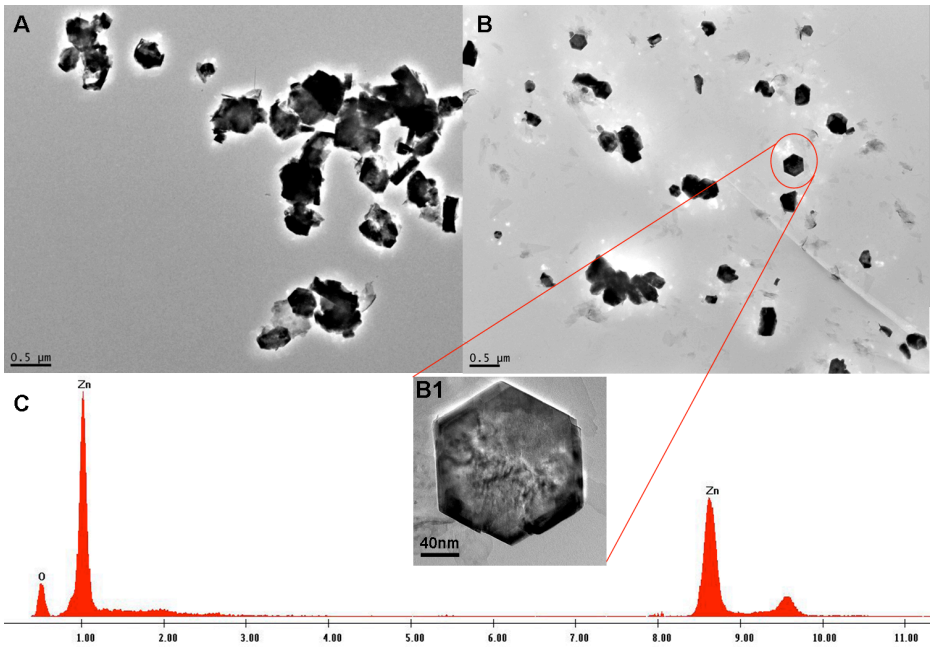

Figure 5.10. TEM images of experimental ZnO NP. The ZnO NPs tend to aggregate under the 200 kV electron beam. (B) EDAX Netcounts of panel B.

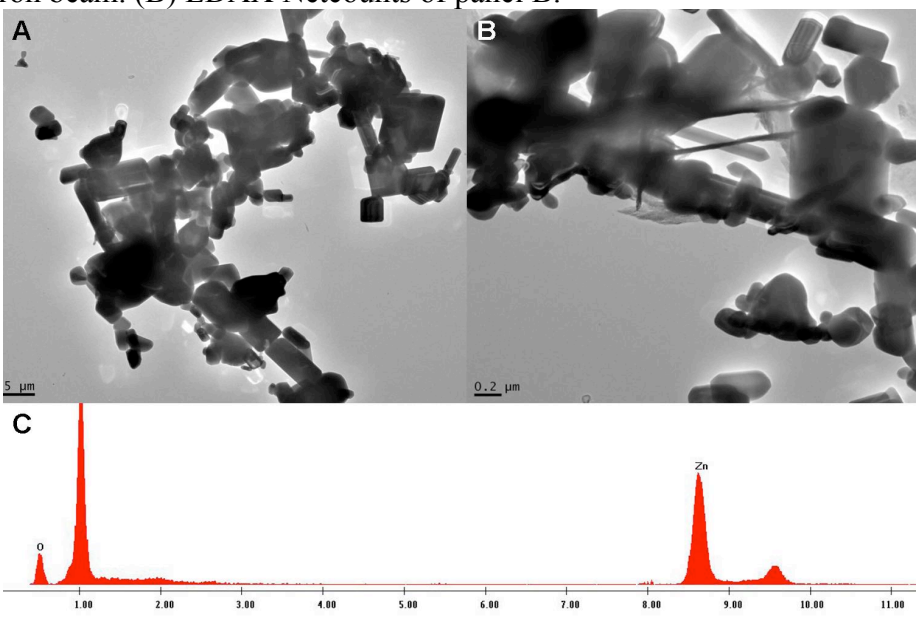

Figure 5.11. TEM images of a commercially available ZnO solution from Fisher: (A) before sonication (5 µm scale bar), and (B) after sonication for 30 s (0.2 µm scale bar). Note the (C) EDAX of sample B.

5.4.1 Modified synthetic method

400 mL of TE buffer (1 mM EDTA, 10 mM Tris) is added to 500 mL of deionized nanopure water (pH = 7.11) and heated to 80 ^{o}C. Whereupon, 400 mL of a 50 mM zinc nitrate

solution is added and 700 mL of a 100 mM Tris is also added. The temperature is brought back to 80 ^{o}C and incubated for 4 min before step cooling to 42^{o}C over 3 hours.

The milliliter-scale synthesis of the ZnO NP without the EDTA in the buffer (e.g. just Tris) results in morphologies that are similar to those observed from the microscale reactions in the Tris, but are more aggregated (TEM in Figure 5.2).

5.5 Conclusions

The synthesis of ZnO nanoparticles was reported wherein the particle size is finely controlled by the duration of incubation at elevated temperatures in a Tris buffered solution. The reaction is driven by the changes in pH as the reaction progresses during the incubation and as the reaction is cooled. This represents a green approach to fabricating NP with narrow dispersity wherein additives such as EDTA further modulate the morphology, e.g. hexagonal puck shaped

	Micro scale (< 0.5 mL)	**mL Scale (3 mL)**	**Macro scale (2 L)**
Rxn vessel	Eppendorf PCR	7 mL amber vial	3 L 3-neck flask
Nanopure water	10 μL	0.5 mL	500 mL
Tris buffer, 100 mM	30 μL	1.5 mL	700 mL
TE buffer (1 mM EDTA, 10 mM Tris)	--	--	400 mL
$Zn(NO_3)_2$, 50 mM	10 μL	0.5 mL	400 mL
other	20 μL water	1.0 mL	
Incubation time at 80 ^{o}C	4-32 min	4-32 min	4 min
Cooling	Remove from block heater	Remove from block heater	Step cooling to 42 ^{o}C over 3 h
comments	12-19 nm ZnO particles depending on incubation time	12-19 nm ZnO particles depending on incubation time	170 ±20 nm Hexagonal platelets

Table 5.3. Summary of the synthesis of ZnO NP.

nanocrystals. The scalability is summarized in Table 3. There are several important applications of doped ZnO NP [27-30]. Future studies will investigate the possibility of introducing metal ion dopants to increase the n-type character of the ZnO (e.g. Al) or make it a p-type material (e.g. Cu) for applications in transparent electronics [27], nanoelectronics such as for field effect transistors [27], gas sensors [28, 29], and ferromagnetism [30]. (See Chapter 6 for preliminary results.)

5.6 References

1. Walter, J. Tire Technology International. http://www.tiretechnologyinternational.com/
2. White, J. L., *Rubber Processing - Technology, Materials and Principles*. 1 ed.; Hanser/Gardner Publications, Inc.
3. Yang, H. Y., Lau, S P, Yu, S F, Huang, L, Tanemura, M, Tanaka, J, Okita, T, Hng, H H Field emission from zinc oxide nanoneedles on plastic substrates. *Nanotechnology* **2005** *16*.
4. Zhang, J.; Wang, Y.; Chen, B.; Li, C.; Wu, D.; Wang, X. Selective oxidation of CO in hydrogen rich gas over platinum-gold catalyst supported on zinc oxide for potential application in fuel cell. *Energy Conversion and Management* **2003,** *44*, 1805-1815.
5. Gamer, A. O.; Leibold, E.; van Ravenzwaay, B. The in vitro absorption of microfine zinc oxide and titanium dioxide through porcine skin. *Toxicology in Vitro* **2006,** *20*, 301-307.
6. Rao, B. B. Zinc oxide ceramic semi-conductor gas sensor for ethanol vapour. *Mater. Chem. Phys.* **2000,** *64*, 62-65.
7. Triboulet, R.; Munoz-Sanjosé, V.; Tena-Zaera, R.; Martinez-Tomas, M. C.; Hassani, S., The Scope of Zinc Oxide Bulk Growth. In *Zinc Oxide — A Material for Micro- and Optoelectronic Applications*, Nickel, N. H.; Terukov, E., Eds. Springer Netherlands: 2005; Vol. 194, pp 3-14.
8. Lai, M. H.; Lee, M. W.; Wang, G.-J.; Tai, M. F. Photovoltaic performance of new-structure ZnO-nanorod dye-sensitized solar cells. *Int. J. Electrochem. Sci.* **2011,** *6*, 2122-2130.
9. Cao, G. Popcorn-style dye-sensitized solar cells. *SPIE Newsroom* **2008**.
10. Zhang, Q.; Dandeneau, C. S.; Zhou, X.; Cao, G. ZnO nanostructures for dye-sensitized solar cells. *Adv. Materials* **2009,** *21*, 4087-4108.
11. Martinson, A. B. F.; Elam, J. W.; Hupp, J. T.; Pellin, M. J. ZnO nanotube based dye-sensitized solar cells. *Nano Letters* **2007,** *7*, 2183-2187.
12. Hanley, C., et.al. Preferential killing of cancer cells and activated human T cells using ZnO nanoparticles. *Nanotechnology* **2008,** *19*.
13. Govender, K.; Boyle, D. S.; Kenway, P. B.; O'Brien, P. Understanding the factors that govern the deposition and morphology of thin films of ZnO from aqueous solution. *J. Mat. Chem.* **2004,** *14*, 2575-2591.
14. Ohara, S.; Mousavand, T.; Umetsu, M.; Takami, S.; Adschiri, T.; Kuroki, Y.; Takata, M. Hydrothermal synthesis of fine zinc oxide particles under supercritical conditions. *Solid State Ionics* **2004,** *172*, 261-264.
15. Xu, L.; Li, Z.; Cai, Q.; Wang, H.; Gao, H.; Lv, W.; Liu, J. Precursor template synthesis of three-dimensional mesoporous ZnO hierarchical structures and their photocatalytic properties. *CrystEngComm* **2010,** *12*, 2166-2172.
16. Wang, W.-W.; Zhu, Y.-J. Shape-controlled synthesis of zinc oxide by microwave heating using an imidazolium salt. *Inorg. Chem. Comm.* **2004,** *7*, 1003-1005.
17. Baruah, S.; Dutta, J. Hydrothermal growth of ZnO nanostructures *Sci. Technol. Adv. Mater.* **2009,** *10* 013001-18.
18. Yadav, A.; Prasad, V.; Kathe, A. A.; Raj, S.; Yadav, D.; Sundaramoorthy, C.; Vigneshwaran, N. Functional finishing in cotton fabrics using zinc oxide nanoparticles. *Bull. Mater. Sci.* **2006,** *29*, 641–645.
19. Vigneshwaran, N., Kumar,Sampath, Kathe, A A , Varadarajan, P V, Prasad, Virendra Functional finishing in cotton fabrics using zinc oxide nanoparticles. *Nanotechnology* **2006,** *17*, 5087-5095.

20. Bauermann, L. P.; Bill, J.; Aldinger, F. Bio-friendly synthesis of ZnO nanoparticles in aqueous solution at near-neutral pH and low temperature. *J. Phys. Chem. B* **2006,** *110*, 5182-5185.
21. Hamby, D. W.; Lucca, D. A.; Lee, J. K.; Nastasi, M.; Kang, H. S.; Lee, S. Y. Effects of hydrogen implantation on the photoluminescence and carrier mobility of ZnO films. *Nuclear Instruments and Methods in Physics Research Section B: Beam Interactions with Materials and Atoms* **2006,** *249*, 196-199.
22. McCluskey, M. D.; Jokela, S. J.; Zhuravlev, K. K.; Simpson, P. J.; Lynn, K. G., *Infrared spectroscopy of hydrogen in ZnO*. AIP: 2002; Vol. 81, p 3807-3809.
23. Weber, M. H., Lynn, Kelvin G. Hydrogen in red ZnO defects or lattice expansion. *J. Phys.: Conf. Ser* **2011,** *262*.
24. Covington, A. K.; Bates, R. G.; Durst, R. A. Definition of pH scales, standard reference values, measurement of pH and related terminology. *Pure Appl. Chem.* **1985,** *57*, 531-542.
25. Kong, L.; Yang, J.-X.; Zhou, H.-P.; Tian, Y.-P.; Wu, J.-Y.; Ji, B.-K. A Surfactant-Free, Precursor-Induced Method to Flower-Like ZnO Nanostructures. *Current Nanoscience* **2009,** *5*, 474-478.
26. Hu, Zeshan; Oskam, Gerko; Searson, Peter C. Influence of solvent on the growth of ZnO nanoparticles. *J. Colloid Interf. Sci.* **2003,** 263, 454-460.
27. Su, D. Su Electron beam induced changes in transition metal oxides. *Anal. Bioanal. Chem.* **2002,** 374, 732-735.
28. Moballegh, A.; Shahverdi, H. R.; Aghababazadeh, R.; Mirhabibi, A. R. ZnO nanoparticles obtained by mechanochemical technique and the optical properties. *Surface Science* **2007,** *601*, 2850-2854.
29. Noriega, R.; Rivnay, J.; Goris, L.; Kälblein, D.; Klauk, H.; Kern, K.; Thompson, L. M.; Palke, A. C.; Stebbins, J. F.; Jokisaari, J. R.; Kusinski, G.; Salleo, A., *Probing the electrical properties of highly-doped Al:ZnO nanowire ensembles*. AIP: 2010; Vol. 107, p 074312.
30. Dimitrov, I. G., et al Al doped ZnO thin films for gas sensor application. *J. Phys.: Conf. Ser* **2008,** *113*, 012044.
31. Gong, H.; Hu, J. Q.; Wang, J. H.; Ong, C. H.; Zhu, F. R. Nano-crystalline Cu-doped ZnO thin film gas sensor for CO. *Sensors and Actuators B: Chemical* **2006,** *115*, 247-251.
32. Wu, S. Z., et al Ferromagnetism studies of Cu-doped and (Cu, Al) co-doped ZnO thin films. *J. Phys.: Conf. Ser.* **2011,** *263*, 012022.

Chapter 6

N- AND P-TYPE DOPING OF ZINC OXIDE FOR SENSING DEVICES: PRELIMINARY DATA

6.1 Introduction

Optical detection of toxic gases is of recent interest because of the high accuracy, rapid response time, good sensitivity, and room temperature performance [1]. Zinc oxide (ZnO) exhibits a high transparency in the visible spectrum and low electric resistance [2-4], so is a promising candidate for gas sensing applications. One type of optical sensor that has been proposed consists of a thin planar waveguide which detect variations in refractive indexes triggered by the interaction between the gas and the high sensitivity sensor material [5, 6]. Several gases such as NO_x, NH_3, SO_x, H_2, and etc. trigger a sensing response when reacting with ZnO. Doping ZnO has shown promise in improving the selectivity of the aforementioned ZnO materials, and small concentrations of dopants such as Al, In, Cu, and Sn have shown to be effective [4, 7]. Doping refers to the insertion of foreign atoms into the crystal structure of a material that, in the case of the semiconductor zinc oxide, alters its conductive [4] and

ferromagnetic characteristics [8]. There are other applications of doped ZnO in photonics, solar energy, and in biology [9, 10].

Given the present and potential applications of ZnO nanomaterials, including those with various dopants, there is a significant need for the facile, green synthesis that affords the means if add dopant atoms to the ZnO matrix. Therefore, we present a greener way to incorporate metal dopants into ZnO by further developing the synthetic methods described and illustrated in chapter 5. The overall goal is to find out if adding the salt of the dopant metal ion to the zinc nitrate reaction mixture will result in incorporation of this ion into the ZnO. Preliminary spectroscopic data from experiments where Cu (II) and Al (III) are added to the zinc nitrate reaction mixture include UV-visible spectra and XRD of the samples of the ZnO.

6.2 Experimental details

The synthetic method was carried out according to Table 5.1 (left column) with the following addition: 2 μL of 10 mM solution of copper nitrate monohydrate (for copper doping) and 10 mM aluminum ammonium sulfate (for aluminum doping) for a total volume of 72 μL in the PCR Eppendorf tube.

Materials

Zinc nitrate hexahydrate, Tris, copper nitrate monohydrate, $Cu(NO_3)_2$, and aluminum ammonium sulfate, $(NH_4)Al(SO_4)_2 \cdot 12H_2O$, were purchased from Sigma Aldrich. Deionized nanopure (Millipore) water was used to prepare a 50 mM solution of zinc nitrate hexahydrate and a 100 mM solution of Tris buffer to which HCl was added until a final pH value of 7.92 was reached. The pH of the deionized nanopure water that was used to prepare all the solutions had a

value of 7.11 (Orion pH meter). The solvent mixture of the two reactants had a pH value of 7.74 at 25 ^{o}C.

Instrumentation

UV-Visible. Beckman Coulter DU800 UV-visible spectrophotometer was used to collect the electronic spectra on 50 μL samples in 8 mm path length cells.

X-ray Diffraction (XRD). All data were collected on a Bruker AXS D8 DISCOVER GADDS with VÅNTEC-2000 Micro-Diffractometer. Samples were prepared under a light microscope by attaching on a loop small crystals of the desired ZnO nanopowders.

Transmission Electron Microscopy (TEM). All data were collected at 200 kV on a Jeol 2100 at the eucentric height to ensure that that all measurements and electron diffraction data were accurate for both collection and comparison. The Jeol 2100 was equipped with an EDAX extension where X-Ray energy dispersion analysis data were collected at minimal dead time (0-10) and count/seconds (<1000). This was performed to optimize signal to noise ratio. Only net-counts were considered (sample – background). A 10 μL drop of the aqueous ZnO NP suspension was placed on a 300 mesh carbon coated copper grid, (TED Pella Inc.), and allowed to dry for 1 minute. The remaining liquid was removed away using a filter paper. The control samples were prepared in the same way. The shape of particles was determined by eucentric tilting (over at least an 60^{o} range) over the particles. Average particle sizes were determined by counting 50 particles from the TEM images for the NP samples using "imageJ" software (NIH).

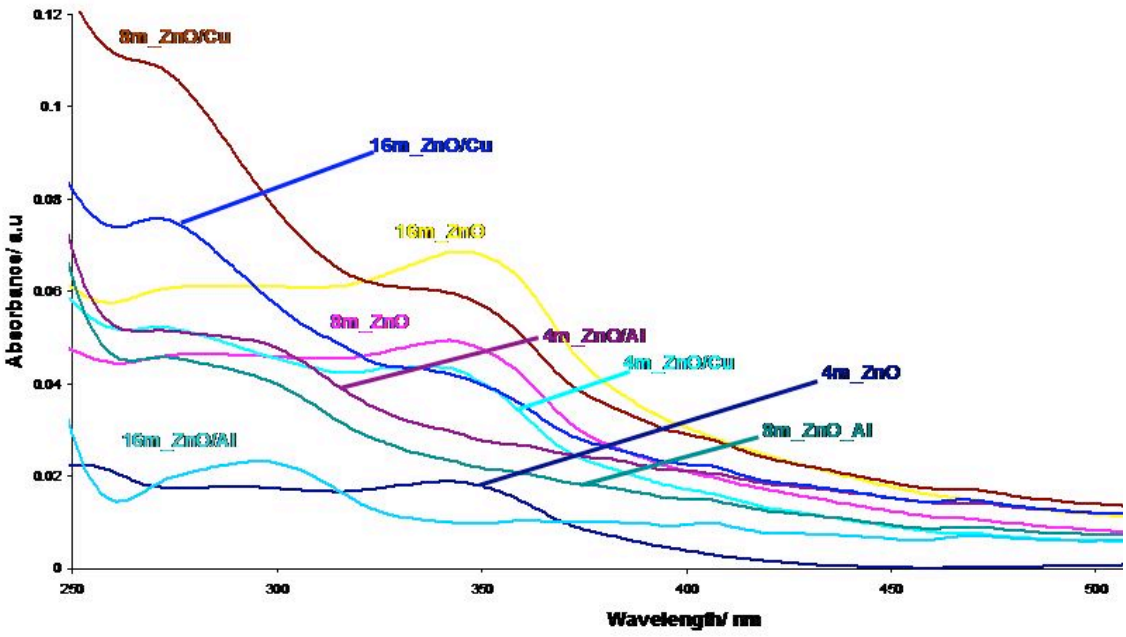

Figure 6.1. UV-Vis spectra of un-doped ZnO (dark blue, purple, and yellow), Al-doped ZnO NPs (aqua, blue, and violet), and Cu-doped ZnO NPs (maroon, blue navy, and light blue).

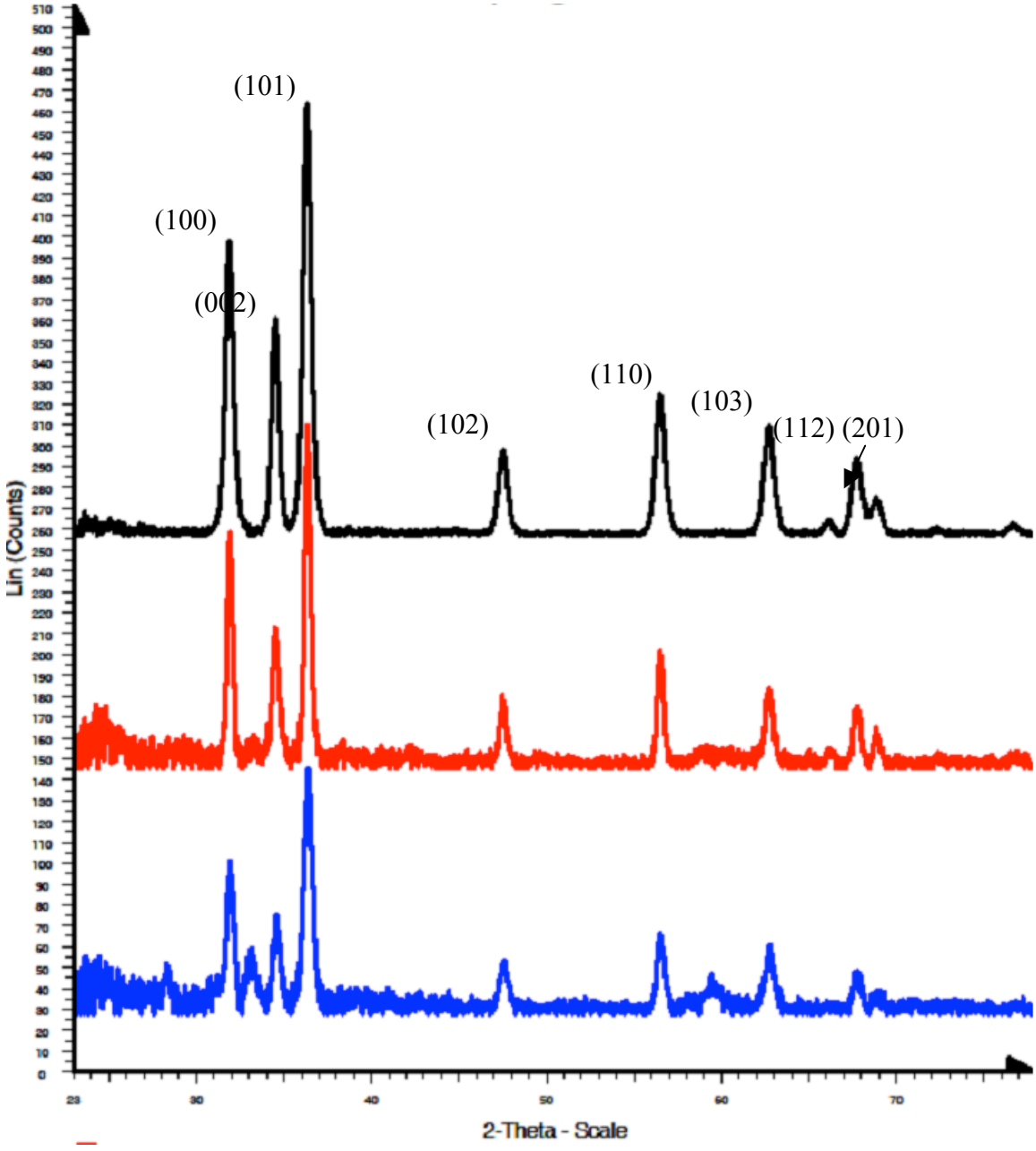

Figure 6.2. XRD data of un-doped ZnO (black), Al-doped ZnO (red) and Cu-doped ZnO NP (blue). For the Al-doped sample the quenching of the (102) diffraction order with comparison to the undoped ZnO sample, denote that doping was obtained [8].

6.3 Results and Discussion

Doping of the ZnO was attempted by adding a 2 μL aliquot of the solution containing the Al(III) or Cu(II) cations (~0.4 molar/molar %) before incubating at 80 ^{o}C. UV-visible spectra of the copper doping samples after 4 min, 8 min, and 16 min of incubation times (Figure 6.1) showed a progressive diminishment of the peak corresponding to the ZnO absorbance at λ= 360 nm, concomitant with an increase of the peak corresponding to the copper absorbance (λ= 270 nm). Furthermore the XRD data from the copper sample showed 3 extra peaks at 33, 48 and 59 (2 theta, Figure 6.2) meanwhile the ZnO crystal structure was unaltered [11].

The UV-visible spectra of the Al samples (resulting from the same incubation times, Figure 6.1) displayed a progressive increase in the absorbance about λ = 300 nm while the ZnO absorbance peak was not visible at any incubation time. XRD data for the aluminum dopant showed very small peaks at 33, 59, and 66 (2 theta, Figure 6.2) which might be artifacts due to the smaller signal-to-noise ratio that this spectrum displays. XRD data from scientific literature show that the peaks corresponding to the 002 and/or 102 planes of the ZnO crystal structure are quenched when dopants are added but no significant other peaks are observed [8]. According to [12] the quenching of the aforementioned peaks by XRD alone is not sufficient to conclude that doping has occurred.

Finally TEM and EDAX (Figures 6.3 and 6.4) results show that aluminum and copper dopants are associated with the ZnO NP (which still maintains its hexagonal structure) since Al and Cu are not detected when the background of the grid is run (carbon film and copper metal grids, also see Figure 6.4 caption). These results indicate that the metal dopant is somehow interacting with the semiconductor ZnO but there is no conclusive evidence that these metallic atoms are embedded in the crystal structure, laying on the surface, or both. Furthermore it is still

impossible to know, in the case that the metals were included in the crystal structure of ZnO, whether they are well ordered or randomly distributed.

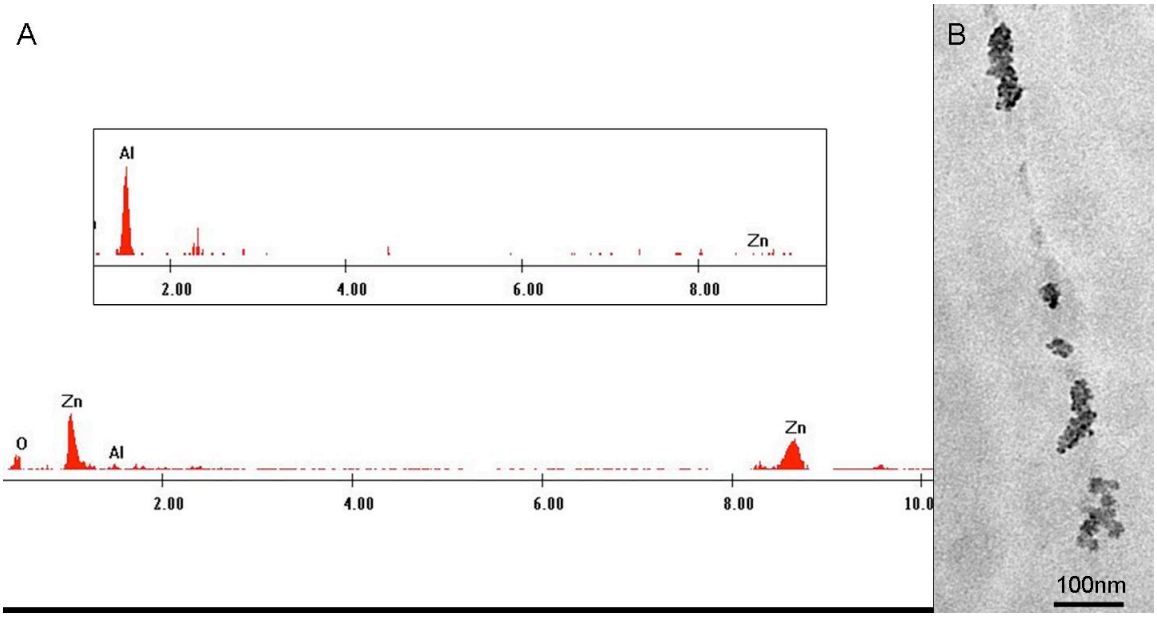

Figure 6.3. (A) X-Ray Energy Dispersive Analysis of Al-doped ZnO from image B. In the inset a netcounts EDAX obtained by subtracting the EDAX corresponding to the typical undoped zinc oxide (see chapter 5) from the EDAX corresponding to Al-doped Zinc oxide (note that the Aluminum peak is magnified). (B) TEM image of Al-doped ZnO (16 min sample). Aggregates of hexagonal shaped ZnO are still observed.

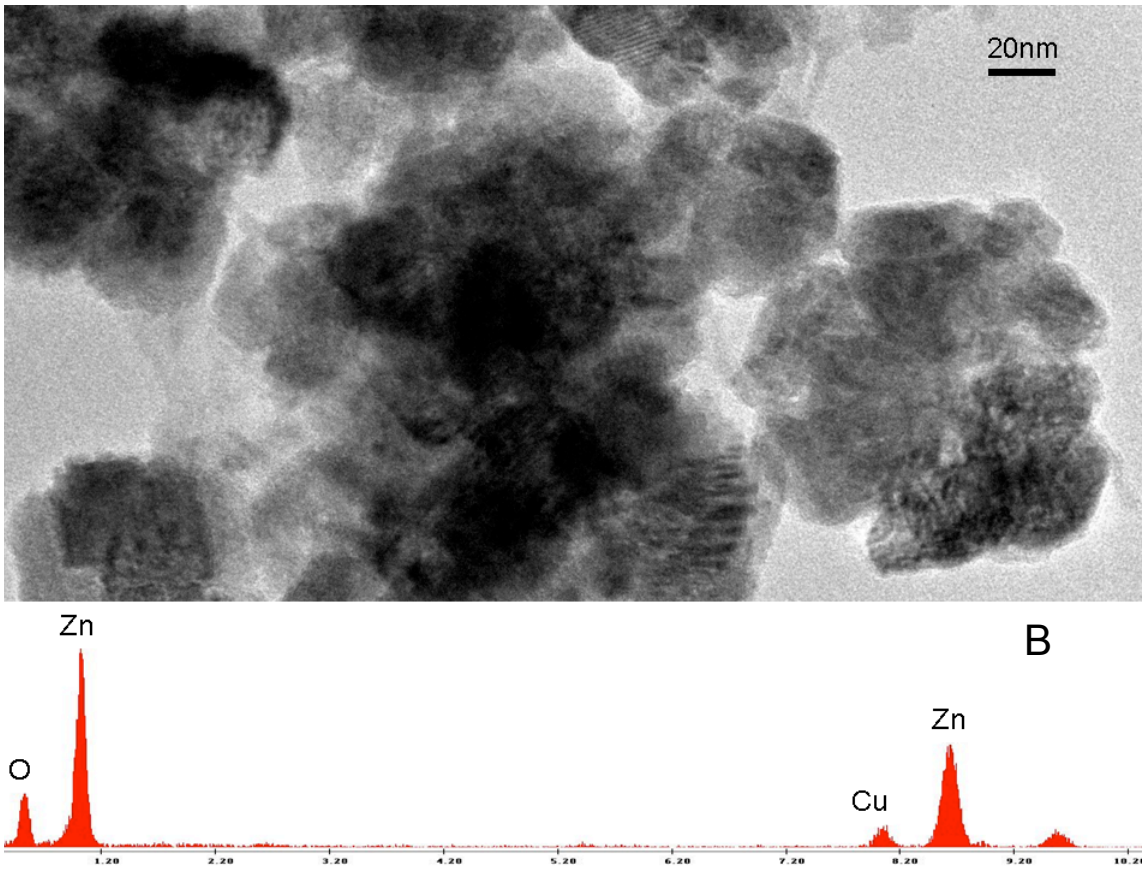

Figure 6.4. (A) TEM image of Cu-doped ZnO (16 min sample). Aggregates of hexagonal shaped ZnO are still observed. (B) X-Ray Energy Dispersive Analysis of Cu-doped ZnO from image A (net counts). Although a carbon coated copper grid was used to perform EDS, the NP aggregate was large and thick enough to still provide a Cu-line signal which otherwise would have been masked by the copper metal grid when subtracting the background signal (net count determination).

6.4 Conclusions

These data demonstrate that doping through the methodology described above is achievable, resulting in incorporation of foreign metals into the ZnO crystal structure. These results are promising but it remains to be determined whether this incorporation leads to increased conductivity of the ZnO material. If this is the case, the ability of the material to increase gas sensitivity may be feasible. Studies that look at the emission of the dope NP may reveal if the dopants are imbedded within the NP or adsorbed onto the NP.

6.5 References

1. Chtanov, A. and M. Gal, *Differential optical detection of hydrogen gas in the atmosphere.* Sensors and Actuators B: Chemical, 2001. **79**(2-3): p. 196-199.
2. Ashida, A., et al., *Optical propagation loss of ZnO films grown on sapphire*. Vol. 95. 2004: AIP. 1673-1676.
3. Holmelund, E., et al., *Pure and Sn-doped ZnO films produced by pulsed laser deposition.* Applied Surface Science, 2002. **197-198**: p. 467-471.
4. Paraguay D, F., et al., *Influence of Al, In, Cu, Fe and Sn dopants on the response of thin film ZnO gas sensor to ethanol vapour.* Thin Solid Films, 2000. **373**(1-2): p. 137-140.
5. Liu, P., Lee, Se-Hee, Cheong, Hyeonsik M., Tracy, C. E., Pitts, J. R., Smith, R. D. , *Stable Pd/V2O5 Optical H2 Sensor.* Journal of The Electrochemical Society, 2002. **149**(3): p. H76-H80.
6. Sarkisov, S.S., et al., *Single-Arm Double-Mode Double-Order Planar Waveguide Interferometric Sensor.* Appl. Opt., 2001. **40**(3): p. 349-359.
7. Viswanatha, R., et al., *Blue-Emitting Copper-Doped Zinc Oxide Nanocrystals.* The Journal of Physical Chemistry B, 2006. **110**(45): p. 22310-22312.
8. Wu, S.Z., et al, *Ferromagnetism studies of Cu-doped and (Cu, Al) co-doped ZnO thin films.* J. Phys.: Conf. Ser., 2011. **263**: p. 012022.
9. Lupan, O., et al, *Synthesis of nanostructured Al-doped zinc oxide films on Si for solar cells application.* Sol. Energ. Mat. Sol C., 2009. **93**: p. 1417-1422.
10. *New Measurement Information System of Biosensor in Relativity Humidity*, J. N. I. T., 2011. **2**(2): p. 31-37.
11. Jung, D, *Syntheses and characterizations of transition metal-doped ZnO.* Solid State Sci., 2010. **12**(4): p. 366-470.
12. Klingshirn, C., et al., *65 years of ZnO research – old and very recent results*. Phys. Status Solid B, 2010. **247**(6): p. 1424-1447.

Chapter 7

CONCLUSIONS

7.1 Design of Greener Syntheses

Despite nanotechnology being exploited for millennia [1] it is only in recent years that scientists have become aware of the properties that materials display at the nano-scale level. In the past decade, material scientists and nanotechnologists have focused their interest on fabricating nanomaterials and their efforts have grown exponentially. This incessant desire to synthesize more and more sophisticated and novel nanostructures has driven the need for greener synthesis. In order to design green synthetic routes, water, cationic aqueous precursors, and relatively mild conditions of temperature and pressure can be employed. Furthermore bio-macromolecules and/or bio-mimetic approaches may be used.

Several biological entities such as proteins [2], viruses [3], and calf thymus DNA [4] have been employed to yield metallic nanoparticles, but poor stability in aqueous media as well as reduced size tunability constitute limiting factors. Approaches that circumvent some of these problems have been described in this thesis.

In Chapter 3 we discussed the design of an environmentally-friendly method of fabricating gold, nickel, and cobalt nanoparticles using plasmid DNA as a mold. Hypothesis 1 was based on

the redox chemistry and the kinetics of this process. Using UV irradiation as well as relatively elevated heat for extensive times allowed us to have higher control over the NP size and ensured high product yields. Hypothesis 2 was based on the well known photo-induced redox chemistry that aqueous suspensions of DNA-bound metal cations undergo upon 254 nm-UV irradiation [5]. Furthermore it is well documented that plasmid DNA, in its toroidal condensation state, has a very robust structure and possesses a mono-dispersed inner cavity [6]. Although we have speculated that the inner diameter of the toroidal topology of plasmid DNA has been the main driver for controlling the size of the metallic nanodiscs upon UV irradiation [7] which triggered the electron loss, we cannot exclude the possibility that plasmid DNA may alternatively act as a seeding agent, since degraded segments of DNA were still observed to be appended to the NPs (Figure 3.11). Additionally, Tris, one of the components of TE buffer (in the plasmid DNA is dissolved) may also act as a seeding agent, and be co-responsible, along with toroidal plasmid DNA, for the NP formation.

Similarly Hypothesis 3, described in detail in Chapter 4, was based on the redox chemistry of thermally degraded DNA-bound metal cations. At relatively high temperatures (70 ^{o}C), the metallic precursors bound to the DNA reactor were reduced to metal and Au, Ag, Cr, and Pd nanoparticles were yielded. The plasmid DNA most likely acts as a nucleation site for the NP synthesis and provides the reducing equivalents, even though a seeding role is not excluded. Furthermore the plasmid DNA, upon thermal degradation, may be wrapped around the NPs and prevent aggregation (i.e. with its negatively charged phosphate backbone repelling other DNA-wrapped NPs). Tris buffer and acetone, may also contribute extra electrons for the completion of the reduction of the metallic NPs.

Hypothesis 4 (Chapter 5) was based on the known pH dependence of Tris buffer and the known olation chemistry of zinc salts which were controlled to make ZnO NP at relatively lower constant temperatures. This straightforward reaction yielded size tunable ZnO NPs in water. Mechanistically, the initial pH change of the Tris buffer may contribute to the first zinc salt precipitation and consequent formation of the ZnO NP product. Indeed, either the absence of the Tris buffer or the employment of a phosphate buffer yielded no ZnO product. Finally, the well known olation chemistry may explain why the reaction at constant temperature (80 ^{o}C), led to a progressive drop in pH over time until 32 min of incubation time at which point the maximum yield of the ZnO precipitate.

Together, these date demonstrate that we have been able to design straightforward, green, and cost effective methods to fabricate metallic NPs and zinc oxide nanopowders (Figure 7.1). Furthermore scalability issues that arise from traditional lab set-ups have been addressed and solved through the design of procedures for liter scale experiments. The high control of size and morphology of the NPs, the high degree of reproducibility, and the ease of this synthetic method will allow us to exploit these synthesized materials for gas sensing, solar cell device, and fungicide agents. In addition to that, the preliminary data on the copper and aluminum doping of zinc oxide (Chapter 6) show that these materials may be feasible in designing efficient structures for the above mentioned applications.

In conclusion, the synthesis of nanomaterials in water will be of great use in the near future when the scientific community recognizes the necessity of greener approaches.

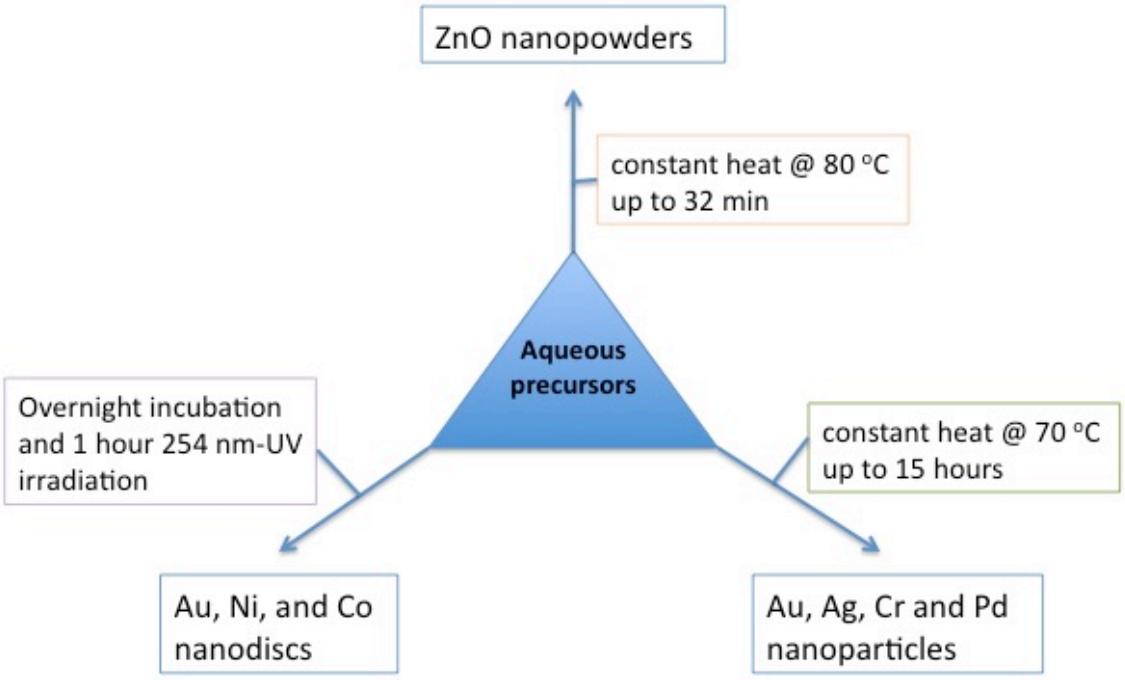

Figure 7.1. Scheme summarizing two greener approaches to synthesize metallic nanoparticles and a scalable aqueous based synthesis of zinc oxide nanopowders.

7.2 References

1. Freestone, I., Meeks, N., Sax, M., and Higgitt, C., *Lycurgus Cup* Gold Bulletin, 2007. **40**(4).
2. Douglas, T. et al., *Protein Size and Crystallinity in Protein-Templated Inorganic Nanoparticles, Chem. Mater.* 2010,. **22(**16), pp 4612–4618
3. Evans, D. J. et al, *Virus templated metallic nanoparticles*. Nanoscale, 2010. 2: p: 2596-2600.
4. Preston, T.C. and Signorell, R., *Calf thymus Formation of Gold Particles on Nanoscale Toroidal DNA Assembled with Bis(ethylenediamine)gold(III).* Lamgmuir, 2010. **26**(12): p: 10250-10253.
5. Berti, Lorenzo, Alessandrini, Andrea, and Paolo Facci, *DNA-Templated Photoinduced Silver Deposition*. J. Am. Chem. Soc. 2005. **127**(32): p. 11216-11217.
6. Hud, N.V., et al., Controlling the size of nanoscale toroidal DNA condensates with static curvature and ionic strength. P.N.A.S., 2003. **100**(16): p. 9296-9301
7. Samson, J., et al., *Fabrication of Metal Nanoparticles Using Toroidal Plasmid DNA as a Sacrificial Mold.* ACS Nano, 2009. **3**(2): p. 339-344.

Bibliography

Chapter 1

1. Kelly, K.L., et al., *The Optical Properties of Metal Nanoparticles: The Influence of Size, Shape, and Dielectric Environment.* J. Phys. Chem. B, 2002. **107**(3): p. 668-677.
2. Alvarez, M.M., et al., *Optical Absorption Spectra of Nanocrystal Gold Molecules.* J. Phys. Chem. B, 1997. **101**(19): p. 3706-3712.
3. Tian, Y. and C. Mao, *Molecular Gears: A Pair of DNA Circles Continuously Rolls against Each Other.* J. Am. Chem. Soc., 2004. **126**(37): p. 11410-11411.
4. Deng, J. and et al., *Fabrication and manipulation of solid-state SiO_2 nano-gears on a gold surface.* Nanotechnology, 2011. **22**(27): p. 275307.
5. Yezhelyev, M.V., et al., *Emerging use of nanoparticles in diagnosis and treatment of breast cancer.* Lancet Oncol., 2006. **7**(8): p. 657-667.
6. Service, R.F., *Nanoparticle Trojan Horses Gallop From the Lab Into the Clinic.* Science, 2010. **330**(6002): p. 314-315.
7. Minnich, A.J., et al., *Bulk nanostructured thermoelectric materials: current research and future prospects.* Energy Environ. Sci., 2009. **2**(5): p. 466-479.
8. Cavalcanti, A.a.R.A.F., Jr., *Nanorobotics Control Design: A collective Behavior Approach for Medicine.* IEEE Trans. Nanobio., 2005. **4**(2): p. 133-140.
9. Balas, F., et al., *Reported nanosafety practices in research laboratories worldwide.* Nature Nanotech., 2010. **5**(2): p. 93-96.
10. Daniel, M.-C. and D. Astruc, *Gold Nanoparticles: Assembly, Supramolecular Chemistry, Quantum-Size-Related Properties, and Applications toward Biology, Catalysis, and Nanotechnology.* Chem. Rev., 2003. **104**(1): p. 293-346.
11. Rechberger, W., et al., *Optical properties of two interacting gold nanoparticles.* Opt. Commun., 2003. **220**(1-3): p. 137-141.
12. Collins, P.G., M.S. Arnold, and P. Avouris, *Engineering Carbon Nanotubes and Nanotube Circuits Using Electrical Breakdown.* Science, 2001. **292**(5517): p. 706-709.
13. Craighead, H.G., *Nanostructure science and technology: Impact and prospects for biology.* J. Vac. Sci. Technol. A 2003. **21**(5): p. S216-S221.
14. Zeng, T., et al., *Fe_3O_4 nanoparticles: a robust and magnetically recoverable catalyst for three-component coupling of aldehyde, alkyne and amine.* Green Chem., 2010. **12**(4): p. 570-573.
15. Stracke, F., I. Rieman, and K. König, *Optical nanoinjection of macromolecules into vital cells.* J. Photochem. Photobiol., B, 2005. **81**(3): p. 136-142.
16. Zheludev, N.I., *Single nanoparticle as photonic switch and optical memory element.* J. Optic. Pure. Appl. Optic., 2006. **8**(4): p. S1.
17. Cheng, G., R.D. Shull, and A.R. Hight Walker, *Dipolar chains formed by chemically synthesized cobalt nanocubes.* J. Magn. Magn. Mater., 2009. **321**(10): p. 1351-1355.
18. Baker C, P.A., Pakstis L, Pochan DJ, Shah SI., *Synthesis and Antibacterial Properties of Silver Nanoparticles.* J. Nanosci. Nanotechnol., 2005. **5**: p. 244-249.
19. Vivero-Escoto, J.L., et al., *Mesoporous Silica Nanoparticles for Intracellular Controlled Drug Delivery.* Small, 2010. **6**(18): p. 1952-1967.

20. Wu, S., et al., *Electrodeposition of silver-DNA hybrid nanoparticles for electrochemical sensing of hydrogen peroxide and glucose.* Electrochem. Commun., 2006. **8**(8): p. 1197-1203.
21. Zhang, J., et al., *One-pot synthesis and characterization of rhodamine derivative-loaded magnetic core–shell nanoparticles.* J. Nanopart. Res., 2011. **13**(5): p. 1909-1916.
22. Cheng, G., et al., *Magnetic-Field-Induced Assemblies of Cobalt Nanoparticles.* Langmuir, 2005. **21**(26): p. 12055-12059.
23. Michael R. Hoffmann, S.T.M., Wonyong Choi, and Detlef W. Bahnemannt, *Environmental Applications of Semiconductor Photocatalysis.* Chem. Rev., 1995. **95**: p. 69-96.
24. Kamat, P.V., *Photochemistry on nonreactive and reactive (semiconductor) surfaces.* Chem. Rev., 1993. **93**(1): p. 267-300.
25. Jolivet, J.-P., *Metal Oxide Chemistry and Synthesis - From Solution to Solid State*2003, Chichester: John Wiley & Sons.
26. He, L., et al., *Antifungal activity of zinc oxide nanoparticles against Botrytis cinerea and Penicillium expansum.* Microbiol. Res., 2011. **166**(3): p. 207-215.
27. Saito, M. and S. Fujihara, *Large photocurrent generation in dye-sensitized ZnO solar cells.* Energy Environ. Sci., 2008. **1**(2): p. 280-283.
28. Ko, S.H., et al., *ZnO nanowire network transistor fabrication on a polymer substrate by low-temperature, all-inorganic nanoparticle solution process.* Appl. Phys. Lett., 2008. **92**(15): p. 154102.
29. Tang, Q., et al., *Characterizations of Cobalt Oxide Nanoparticles within Faujasite Zeolites and the Formation of Metallic Cobalt.* Chem. Mater., 2004. **16**(10): p. 1967-1976.
30. Kanan, M.W. and D.G. Nocera, *In Situ Formation of an Oxygen-Evolving Catalyst in Neutral Water Containing Phosphate and Co2+.* Science, 2008. **321**(5892): p. 1072-1075.
31. Cross, C.E., J.C. Hemminger, and R.M. Penner, *Physical Vapor Deposition of One-Dimensional Nanoparticle Arrays on Graphite: Seeding the Electrodeposition of Gold Nanowires.* Langmuir, 2007. **23**(20): p. 10372-10379.
32. Liu, J., et al., *Precise Seed-Mediated Growth and Size-Controlled Synthesis of Palladium Nanoparticles Using a Green Chemistry Approach.* Langmuir, 2009. **25**(12): p. 7116-7128.
33. Lei, Z., L. Zhang, and X. Wei, *One-step synthesis of silver nanoparticles by sonication or heating using amphiphilic block copolymer as templates.* J. Colloid Interface Sci., 2008. **324**(1-2): p. 216-219.
34. Kumar, P.S.S., et al., *Sonochemical synthesis and characterization of gold-ruthenium bimetallic nanoparticles.* Colloid Surface A, 2010. **356**(1-3): p. 140-144.
35. Kimling, J., et al., *Turkevich Method for Gold Nanoparticle Synthesis Revisited.* J. Phys. Chem. B, 2006. **110**(32): p. 15700-15707.
36. Goulet, P.J.G. and R.B. Lennox, *New Insights into Brust−Schiffrin Metal Nanoparticle Synthesis.* J. Am. Chem. Soc., 2010. **132**(28): p. 9582-9584.
37. Barakat, K.A., et al., *Disproportionation of Gold(II) Complexes. A Density Functional Study of Ligand and Solvent Effects.* J. Phys. Chem. B, 2006. **110**(30): p. 14645-14651.
38. Aljabali, A.A.A., et al., *Virus templated metallic nanoparticles.* Nanoscale, 2010. **2**(12): p. 2596-2600.

39. Asuri, P., et al., *The protein-nanomaterial interface.* Curr. Opin. Biotechnol., 2006. **17**(6): p. 562-568.
40. Kane, R.S. and A.D. Stroock, *Nanobiotechnology: Protein-Nanomaterial Interactions.* Biotechnol. Progr., 2007. **23**(2): p. 316-319.
41. Kumar, A. and A. Jakhmola, *RNA-Mediated Fluorescent Q-PbS Nanoparticles.* Langmuir, 2007. **23**(6): p. 2915-2918.
42. Sun, L., et al., *Fabrication of silver nanoparticles ring templated by plasmid DNA.* Appl. Surf. Sci., 2006. **252**(14): p. 4969-4974.
43. Becerril, H.A. and A.T. Woolley, *DNA-templated nanofabrication.* Chem. Soc. Rev., 2009. **38**(2): p. 329-337.
44. de la Escosura, A., et al., *Viral capsids as templates for the production of monodisperse Prussian blue nanoparticles.* Chem. Commun., 2008(13): p. 1542-1544.
45. Samson, J., et al., *Fabrication of Metal Nanoparticles Using Toroidal Plasmid DNA as a Sacrificial Mold.* ACS Nano, 2009. **3**(2): p. 339-344.
46. Yu, et al., *Gold Nanorods: Electrochemical Synthesis and Optical Properties.* J. Phys. Chem. B, 1997. **101**(34): p. 6661-6664.
47. Carrot, G., et al., *Gold nanoparticle synthesis in graft copolymer micelles.* Colloid Polym. Sci., 1998. **276**(10): p. 853-859.
48. Aslam, M., et al., *Novel one-step synthesis of amine-stabilized aqueous colloidal gold nanoparticles.* J. Mater. Chem., 2004. **14**(12): p. 1795-1797.
49. Jana, N.R., L. Gearheart, and C.J. Murphy, *Wet Chemical Synthesis of High Aspect Ratio Cylindrical Gold Nanorods.* J. Phys. Chem. B, 2001. **105**(19): p. 4065-4067.
50. Zanella, R., et al., *Alternative Methods for the Preparation of Gold Nanoparticles Supported on TiO2.* J. Phys. Chem. B, 2002. **106**(31): p. 7634-7642.
51. Preston, T.C. and R. Signorell, *Formation of Gold Particles on Nanoscale Toroidal DNA Assembled with Bis(ethylenediamine)gold(III).* Langmuir, 2010. **26**(12): p. 10250-10253.
52. Slocik, J.M., et al., *Viral templates for gold nanoparticle synthesis.* J. Mater. Chem., 2005. **15**(7): p. 749-753.
53. Sau, T.K., et al., *Size Controlled Synthesis of Gold Nanoparticles using Photochemically Prepared Seed Particles.* J. Nanopart. Res., 2001. **3**(4): p. 257-261.
54. *Zinc Oxide Nanostructures: Synthesis and Properties.* J. Nanosci. Nanotechno., 2005. **5**: p. 1561-1573.
55. Hingorani, S., et al., *Microemulsion mediated synthesis of zinc oxide nanoparticles for varistors studies*, Mater. Res. Bull., 1993. **28**(12): p. 1303-131.
56. Dong, Q., et al., *Synthesis of biomorphic ZnO interwoven microfibers using eggshell membrane as the biotemplate*, Mater. Lett., 2007. **61**(13): p. 2714-2717.
57. Krishnakuma, T., et al., *Microwave-assisted synthesis and characterization of flower shaped zinc oxide nanostructures*, Mater. Lett., 2009. **63**(2): p. 242-245.
58. Cohen, Stanley N., Chang, Annie C. Y., Boyer, Herbert W., and Robert B. Helling, *Construction of Biologically Functional Bacterial Plasmids In Vitro*. Proc. Natl. Acad. Sci. USA, **1973**. **70**(11): p. 3240-3244.
59. Barton, Jacqueline K., Goldberg, Jonathan M., Kumar, Challa V., and Nicholas J. Turro, *Binding Modes and Base Specificity of Tris(phenanthroline)ruthenium(II) Enantiomers with Nucleic Acids: Tuning the Stereoselectivity*. J. Am. Chem. Soc. **1986. 108**: p. 2081-2088.

60. Rosenthal, A., Coutelle, O., and M. Craxton, *Large-scale production of DNA sequencing templates by microtitre format PCR.* Nucleic Acids Res. **1993**. **21**(1): p. 173–174.
61. Candeias, L. P. and S. Steenken, *Structure and Acid-Base Properties of One-Electron-Oxidized Deoxyguanosine, Guanosine, and 1 -Met hylguanosine*. J. Am. Chem. Soc. **1989**. **111**: p. 1094-1099.
62. Shinde, Sujata S., Maroz, Andrej, Hay, Michael P., and Robert F. Anderson, *One-Electron Reduction Potential of the Neutral Guanyl Radical in the GC Base Pair of Duplex DNA*. J. Am. Chem. Soc. **2009**. **131**(14): p. 5203–5207.
63. Berti, Lorenzo, Alessandrini, Andrea, and Paolo Facci, *DNA-Templated Photoinduced Silver Deposition*. J. Am. Chem. Soc. **2005**. **127**(32): p. 11216–11217.
64. Armitage, Bruce, *Photocleavage of Nucleic Acids*. Chem. Rev. **1998**. **98**(3): p. 1171–1200.
65. Kawanishi, Shosuke, Hiraku, Yusuke, and Shinji Oikawa, *Mechanism of guanine-specific DNA damage by oxidative stress and its role in carcinogenesis and aging*. Mutation Research. **2001**. **488**(1): p.65-76.
66. Khanduri, Deepti, Adhikary, Amitava, and Michael D. Sevilla, *Highly Oxidizing Excited States of One-Electron-Oxidized Guanine in DNA: Wavelength and pH Dependence*. J. Am. Chem. Soc. **2011**. **133**(12): p. 4527–4537.
67. Vilfan, Igor D., Conwell, Christine C., Sarkar, Tumpa, and Nicholas V. Hud, *Time Study of DNA Condensate Morphology: Implications Regarding the Nucleation, Growth, and Equilibrium Populations of Toroids and Rods*. Biochemistry. **2006. 45**(26): p. 8174-8183.
68. Steenken, S.; Jovanovic, S. V. *How Easily Oxidizable Is DNA? One-Electron Reduction Potentials of Adenosine and Guanosine Radicals in Aqueous Solution.* J. Am. Chem. Soc. **1997**. **119**: p. 617-618.

Chapter 2

1. Alivisatos, A.P., *Semiconductor Clusters, Nanocrystals, and Quantum Dots.* Science, 1996. **271**(5251): p. 933-937.
2. Stellacci, F., *Nanoscale materials: A new season.* Nat Mater, 2005. **4**(2): p. 113-114.
3. Sharma, P., et al., *Gold-Speckled Multimodal Nanoparticles for Noninvasive Bioimaging.* Chem. Mater., 2008. **20**(19): p. 6087-6094.
4. A Wieckowski et al., *Catalysis and Electrocatalysis at Nanoparticle Surfaces*2003, New York: Marcel Dekker.
5. Grzelczak, M., et al., *Directed Self-Assembly of Nanoparticles.* ACS Nano, 2010. **4**(7): p. 3591-3605.
6. Song, Q. and Z.J. Zhang, *Shape Control and Associated Magnetic Properties of Spinel Cobalt Ferrite Nanocrystals.* J. Am. Chem. Soc., 2004. **126**(19): p. 6164-6168.
7. Cross, S.E., et al., *Human Skin Penetration of Sunscreen Nanoparticles: In-vitro Assessment of a Novel Micronized Zinc Oxide Formulation.* Skin Pharmacology and Physiology, 2007. **20**(3): p. 148-154.
8. Beek, W.J.E., M.M. Wienk, and R.A.J. Janssen, *Hybrid polymer solar cells based on zinc oxide.* J. Mater. Chem., 2005. **15**(29): p. 2985-2988.
9. Samson, J., et al., *Fabrication of Metal Nanoparticles Using Toroidal Plasmid DNA as a Sacrificial Mold.* ACS Nano, 2009. **3**(2): p. 339-344.

10. Masala, O. and R. Seshadri, *Synthesis Routes for Large Volumes of Nanoparticles.* Annual Review of Materials Research, 2004. **34**(1): p. 41-81.
11. Russell, J.J.B.a.L.D., *Electron Microscopy*1992, Boston: Jones and Bartlett Publishers.
12. B.E.P. Beeston, R.W.H.a.R.M., *Electron Diffraction and Optical Diffraction Techniques.* : Elsevier Science Ltd.
13. Eades, A., *One of my Failures: Diffraction in the TEM.* Microscopy Today, 2011. **19**(01).
14. Steeds, J.W., *Introduction to Analytical Electron Microscopy*1979.
15. Song, Y., et al., *Microfluidic Synthesis of Cobalt Nanoparticles.* Chem. of Mater., 2006. **18**(12): p. 2817-2827.

Chapter 3

1. Lu, A.-H., E.L. Salabas, and F. Schüth, *Magnetic Nanoparticles: Synthesis, Protection, Functionalization, and Application.* Angew. Chem. Inter. Ed., 2007. **46**(8): p. 1222-1244.
2. Feldheim, D.L.F., C. A., Jr., *Metal Nanoparticles: Synthesis, Characterization, and Applications;*2002, Ne York: Marcel Dekker.
3. Drain, C.M., et al., *Porphyrin nanoparticles as supramolecular systems.* New J. Chem., 2006. **30**(12): p. 1834-1843.
4. Frenkel, J.D., J., *Spontaneous and Induced Magnetization in Ferromagnetic Bodies.* Nature, 2003: p. 274–275.
5. Guo, F., et al., *Synthesis of cobalt nanoparticles in ethanol hydrazine alkaline system (EHAS) at room temperature.* Mater. Lett., 2002. **56**(6): p. 906-909.
6. Puntes, V.F., K. Krishnan, and A.P. Alivisatos, *Synthesis of Colloidal Cobalt Nanoparticles with Controlled Size and Shapes.* Topics in Catalysis, 2002. **19**(2): p. 145-148.
7. Puntes, V.F., K.M. Krishnan, and P. Alivisatos, *Synthesis, self-assembly, and magnetic behavior of a two-dimensional superlattice of single-crystal ?Co nanoparticles*. Vol. 78. 2001: AIP. 2187-2189.
8. Kim, S.-W., et al., *Synthesis of Monodisperse Palladium Nanoparticles.* Nano Lett., 2003. **3**(9): p. 1289-1291.
9. Takami, A., H. Kurita, and S. Koda, *Laser-Induced Size Reduction of Noble Metal Particles.* J. Phys. Chem. B, 1999. **103**(8): p. 1226-1232.
10. Kazakevich, P.V., et al., *Laser induced synthesis of nanoparticles in liquids.* Applied Surface Science, 2006. **252**(13): p. 4373-4380.
11. Vesperinas, A., et al., *Light-induced flocculation of gold nanoparticles.* Chem. Commun., 2007(38): p. 3912-3914.
12. Fang, Q., et al., *Palladium nanoparticles on silicon by photo-reduction using 172 nm excimer UV lamps.* Appl. Surf. Sci., 2004. **226**(1-3): p. 7-11.
13. Chen, P., et al., *Synthesis of Cu Nanoparticles and Microsized Fibers by Using Carbon Nanotubes as a Template.* J. Phys. Chem. B, 1999. **103**(22): p. 4559-4561.
14. Banerjee, I.A., L. Yu, and H. Matsui, *Cu nanocrystal growth on peptide nanotubes by biomineralization: Size control of Cu nanocrystals by tuning peptide conformation.* P. Natl. A. Sci., 2003. **100**(25): p. 14678-14682.
15. Sun, L., et al., *Fabrication of silver nanoparticles ring templated by plasmid DNA.* Appl. Surf. Sci., 2006. **252**(14): p. 4969-4974.

16. Aldaye, F.A., A.L. Palmer, and H.F. Sleiman, *Assembling Materials with DNA as the Guide.* Science, 2008. **321**(5897): p. 1795-1799.
17. Coffer, J.L., et al., *Dictation of the shape of mesoscale semiconductor nanoparticle assemblies by plasmid DNA*. Vol. 69. 1996: AIP. 3851-3853.
18. Flynn, C.E., et al., *Viruses as vehicles for growth, organization and assembly of materials.* Acta Mater., 2003. **51**(19): p. 5867-5880.
19. Maruszewski, K., et al., *Raman Spectra of Molecules Adsorbed on Ag Centers in Sol-Gel Matrices.* J. Sol-Gel Sci. Techn., 2003. **26**(1): p. 83-88.
20. Antonietti, M. and G.A. Ozin, *Promises and Problems of Mesoscale Materials Chemistry or Why Meso?* Chemistry – A European Journal, 2004. **10**(1): p. 28-41.
21. Zhong, Z., et al., *d-Glucose-Derived Polymer Intermediates as Templates for the Synthesis of Ultrastable and Redispersible Gold Colloids.* Langmuir, 2008. **24**(9): p. 4655-4660.
22. Ganesan, R.G., Aharon, *Synthesis of WO3 nanoparticles using a biopolymer as a template for electrocatalytic hydrogen evolution.* Nanotechnology, 2008. **19**(2).
23. Djalali, R., J. Samson, and H. Matsui, *Doughnut-Shaped Peptide Nano-Assemblies and Their Applications as Nanoreactors.* J. Am. Chem. Soc., 2004. **126**(25): p. 7935-7939.
24. Lipps, G., *Plasmids: Current Research and Future Trends;*2008, Norfolk, U.K.,: Caister Academic Press:.
25. *QIAGEN PlasmidAmp Kit-For direct amplification of plasmid DNA from bacterial colonies*.
26. Conwell, C.C., I.D. Vilfan, and N.V. Hud, *Controlling the size of nanoscale toroidal DNA condensates with static curvature and ionic strength.* Proceedings of the National Academy of Sciences, 2003. **100**(16): p. 9296-9301.
27. Bloomfield, V.A., *Condensation of DNA by multivalent cations: Considerations on mechanism.* Biopolymers, 1991. **31**(13): p. 1471-1481.
28. Bartolini, W.P. and M.V. Johnston, *Characterizing DNA photo-oxidation reactions by high-resolution mass measurements with matrix-assisted laser desorption/ionization time-of-flight mass spectrometry.* J. Mass. Spectrom., 2000. **35**(3): p. 408-416.
29. Boerner, L.J.K. and J.M. Zaleski, *Metal complex-DNA interactions: from transcription inhibition to photoactivated cleavage.* Curr. Opin. Chem. Biol., 2005. **9**(2): p. 135-144.
30. Sinha, R.P. and D.-P. Hader, *UV-induced DNA damage and repair: a review.* Photoch Photobio. Sci., 2002. **1**(4): p. 225-236.
31. Wong, C.; West, P. E.; Olson, K. S.; Mecartney, M. L.; Starostina, *N. Tip Dilation and AFM Capabilities in the Characterization of Nanoparticles*. J. Met. **2007**, *59*, 12–16.
32. web.archive.org/web/20070518092613/http://www.northland.cc.mn.us/Chemistry /standard/standard_reduction_potentials.htm. Standard reduction potentials
33. Schnell, J. R.; Berman, J.; Bloomfield, V. A. *Insertion of Telomere Repeat Sequence Decreases Plasmid DNA Condensation by Cobalt (III) Hexaammine.* Biophys. J. **1998**, *74*, 1484–1491.
34. Davey, C. A.; Richmond, T. J. *DNA-Dependent Divalent Cation Binding in the Nucleosome Core Particle.* Proc. Natl. Acad. Sci. U.S.A. **2002**, *99*, 11169–11174.
35. Liu, C.; Wang, M.; Zhang, T.; Sun, H. *DNA Hydrolysis Promoted by Di- and Multi Nuclear Metal Complexes.* Coord. Chem. Rev. **2004**, *248*, 147–168.
36. Berti, L.; Alessandrini, A.; Facci, P. *DNA-Templated Photoinduced Silver Deposition.* J. Am. Chem. Soc. **2005**, *127*, 11216–11217.

37. Burley, G. A.; Gierlich, J.; Mofid, M. R.; Nir, H.; Tal, S.; Eichen, Y.; Carell, T. *Directed DNA Metallization.* J. Am. Chem. Soc. **2006**, *128*, 1398–1399.
38. Horcas, I.; Fernandez, R.; Gomez-Rodriguez, J. M.; Colchero, J. *WSXM: A Software for Scanning Probe Microscopy and a Tool for Nanotechnology.* Rev. Sci. Instrum. **2007**, *78*,013705.

Chapter 4

1. Sun, Y.; Xia, Y. Shape-Controlled Synthesis of Gold and Silver Nanoparticles. *Science* **2002,** *298*, 2176-2179.
2. Wagner, J.; Köhler, J. M. Continuous Synthesis of Gold Nanoparticles in a Microreactor. *Nano Lett.* **2005,** *5*, 685-691.
3. Jana, N. R.; Gearheart, L.; Murphy, C. J. Seeding Growth for Size Control of 5−40 nm Diameter Gold Nanoparticles. *Langmuir* **2001,** *17*, 6782-6786.
4. Shanmugam, S.; Viswanathan, B.; Varadarajan, T. K. A novel single step chemical route for noble metal nanoparticles embedded organic-inorganic composite films. *Mater. Chem. Phys.* **2006,** *95*, 51-55.
5. Hiramatsu, H.; Osterloh, F. E. A Simple Large-Scale Synthesis of Nearly Monodisperse Gold and Silver Nanoparticles with Adjustable Sizes and with Exchangeable Surfactants. *Chem. Mater.* **2004,** *16*, 2509-2511.
6. Martinez-Hurtado, J. L. Metallic Nanoparticle Block Copoloymer Vesicles with Enhanced Optical Properties. *Nanomaterials* **2011,** *1*, 20-30.
7. Tiwari, P.; Vig, K.; Dennis, V.; Singh, S. Functionalized Gold Nanoparticles and Their Biomedical Applications. *Nanomaterials* **2011,** *1*, 31-63.
8. Campelo, J. M.; Conesa, T. D.; Gracia, M. J.; Jurado, M. J.; Luque, R.; Marinas, J. M.; Romero, A. A. Microwave facile preparation of highly active and dispersed SBA-12 supported metal nanoparticles. *Green Chem.* **2008,** *10*, 853-858.
9. Ravindra, P. Protein-mediated synthesis of gold nanoparticles. *Mater. Sci. Eng B-Solid* **2009,** *163*, 93-98.
10. Slocik, J. M.; Naik, R. R.; Stone, M. O.; Wright, D. W. Viral templates for gold nanoparticle synthesis. *J. Mater. Chem.* **2005,** *15*, 749-753.
11. Samson, J.; Varotto, A.; Nahirney, P. C.; Toschi, A.; Piscopo, I.; Drain, C. M. Fabrication of Metal Nanoparticles Using Toroidal Plasmid DNA as a Sacrificial Mold. *ACS Nano* **2009,** *3*, 339-344.
12. Kimling, J.; Maier, M.; Okenve, B.; Kotaidis, V.; Ballot, H.; Plech, A. Turkevich Method for Gold Nanoparticle Synthesis Revisited. *J. Phys.Chem. B* **2006,** *110*, 15700-15707.
13. Haiss, W.; Thanh, N. T. K.; Aveyard, J.; Fernig, D. G. Determination of Size and Concentration of Gold Nanoparticles from UV−Vis Spectra. *Anal. Chem.* **2007,** *79*, 4215-4221.
14. Liu, X.; Atwater, M.; Wang, J.; Huo, Q. Extinction coefficient of gold nanoparticles with different sizes and different capping ligands. *Colloid Surface B* **2007,** *58*, 3-7.
15. Aslam, M.; Fu, L.; Su, M.; Vijayamohanan, K.; Dravid, V. P. Novel one-step synthesis of amine-stabilized aqueous colloidal gold nanoparticles. *J. Mater. Chem.* **2004,** *14*, 1795-1797.

16. Leff, D. V.; Brandt, L.; Heath, J. R. Synthesis and Characterization of Hydrophobic, Organically-Soluble Gold Nanocrystals Functionalized with Primary Amines. *Langmuir* **1996,** *12*, 4723-4730.
17. Newman, J. D. S.; Blanchard, G. J. Formation of Gold Nanoparticles Using Amine Reducing Agents. *Langmuir* **2006,** *22*, 5882-5887.
18. Subramaniam, C.; Tom, R. T.; Pradeep, T. On the formation of protected gold nanoparticles from $AuCl_4^-$ by the reduction using aromatic amine. *J. Nanoparticle Res.* **2005,** *7*, 209-217.
19. Hud, N.; Polak, M. DNA-cation interactions: the major and minor grooves are flexible ionophores. *Curr. Opin. Struct. Biol.* **2001,** *11*, 293-301.
20. Hu, J.; Liu, Y. Pd Nanoparticle Aging and Its Implications in the Suzuki Cross-Coupling Reaction. *Langmuir* **2005,** *21*, 2121-2123.
21. Chandrasekhar, V.; Suriya Narayanan, R.; Thilagar, P. Organostannoxane-Supported Palladium Nanoparticles. Highly Efficient Catalysts for Suzuki-Coupling Reactions. *Organometallics* **2009,** *28*, 5883-5888.
22. Watt, J.; Cheong, S.; Toney, M. F.; Ingham, B.; Cookson, J.; Bishop, P. T.; Tilley, R. D. Ultrafast Growth of Highly Branched Palladium Nanostructures for Catalysis. *ACS Nano* **2009,** *4*, 396-402.
23. Maduraiveeran, G.; Ramaraj, R. Potential Sensing Platform of Silver Nanoparticles Embedded in Functionalized Silicate Shell for Nitroaromatic Compounds. *Anal. Chem.* **2009,** *81*, 7552-7560.
24. Encina, E. R.; Coronado, E. A. Plasmon Coupling in Silver Nanosphere Pairs. *J Phys. Chem. C* **2010,** *114*, 3918-3923.
25. Mitsuishi, M.; Tanaka, H.; Obata, M.; Miyashita, T. Plasmon-Enhanced Luminescence from Ultrathin Hybrid Polymer Nanoassemblies for Microscopic Oxygen Sensor Application. *Langmuir* **2010,** *26*, 15117-15120.
26. Ramesh, G. V.; Radhakrishnan, T. P. A Universal Sensor for Mercury (Hg, HgI, HgII) Based on Silver Nanoparticle-Embedded Polymer Thin Film. *ACS Appl. Mat. Interfaces* **2011,** *3*, 988-994.
27. Wang, W.; Shi, X.; Kariuki, N. N.; Schadt, M.; Wang, G. R.; Rendeng, Q.; Choi, J.; Luo, J.; Lu, S.; Zhong, C.-J. Array of Molecularly Mediated Thin Film Assemblies of Nanoparticles: Correlation of Vapor Sensing with Interparticle Spatial Properties. *J. Am. Chem. Soc.* **2007,** *129*, 2161-2170.
28. Pribik, R.; Aslan, K.; Zhang, Y.; Geddes, C. D. Metal-Enhanced Fluorescence from Chromium Nanodeposits. *J. Phys. Chem. C* **2008,** *112*, 17969-17973.

Chapter 5

1. Walter, J. Tire Technology International. http://www.tiretechnologyinternational.com
2. White, J. L., *Rubber Processing - Technology, Materials and Principles*. 1 ed.; Hanser/Gardner Publications, Inc.
3. Yang, H. Y., Lau, S P, Yu, S F, Huang, L, Tanemura, M, Tanaka, J, Okita, T, Hng, H H Field emission from zinc oxide nanoneedles on plastic substrates. *Nanotechnology* **2005** *16*.

4. Zhang, J.; Wang, Y.; Chen, B.; Li, C.; Wu, D.; Wang, X. Selective oxidation of CO in hydrogen rich gas over platinum-gold catalyst supported on zinc oxide for potential application in fuel cell. *Energy Conversion and Management* **2003,** *44*, 1805-1815.
5. Gamer, A. O.; Leibold, E.; van Ravenzwaay, B. The in vitro absorption of microfine zinc oxide and titanium dioxide through porcine skin. *Toxicology in Vitro* **2006,** *20*, 301-307.
6. Rao, B. B. Zinc oxide ceramic semi-conductor gas sensor for ethanol vapour. *Mater. Chem. Phys.* **2000,** *64*, 62-65.
7. Triboulet, R.; Munoz-Sanjosé, V.; Tena-Zaera, R.; Martinez-Tomas, M. C.; Hassani, S., The Scope of Zinc Oxide Bulk Growth. In *Zinc Oxide — A Material for Micro- and Optoelectronic Applications*, Nickel, N. H.; Terukov, E., Eds. Springer Netherlands: 2005; Vol. 194, pp 3-14.
8. Lai, M. H.; Lee, M. W.; Wang, G.-J.; Tai, M. F. Photovoltaic performance of new-structure ZnO-nanorod dye-sensitized solar cells. *Int. J. Electrochem. Sci.* **2011,** *6*, 2122-2130.
9. Cao, G. Popcorn-style dye-sensitized solar cells. *SPIE Newsroom* **2008**.
10. Zhang, Q.; Dandeneau, C. S.; Zhou, X.; Cao, G. ZnO nanostructures for dye-sensitized solar cells. *Adv. Materials* **2009,** *21*, 4087-4108.
11. Martinson, A. B. F.; Elam, J. W.; Hupp, J. T.; Pellin, M. J. ZnO nanotube based dye-sensitized solar cells. *Nano Letters* **2007,** *7*, 2183-2187.
12. Hanley, C., et.al. Preferential killing of cancer cells and activated human T cells using ZnO nanoparticles. *Nanotechnology* **2008,** *19*.
13. Govender, K.; Boyle, D. S.; Kenway, P. B.; O'Brien, P. Understanding the factors that govern the deposition and morphology of thin films of ZnO from aqueous solution. *J. Mat. Chem.* **2004,** *14*, 2575-2591.
14. Ohara, S.; Mousavand, T.; Umetsu, M.; Takami, S.; Adschiri, T.; Kuroki, Y.; Takata, M. Hydrothermal synthesis of fine zinc oxide particles under supercritical conditions. *Solid State Ionics* **2004,** *172*, 261-264.
15. Xu, L.; Li, Z.; Cai, Q.; Wang, H.; Gao, H.; Lv, W.; Liu, J. Precursor template synthesis of three-dimensional mesoporous ZnO hierarchical structures and their photocatalytic properties. *CrystEngComm* **2010,** *12*, 2166-2172.
16. Wang, W.-W.; Zhu, Y.-J. Shape-controlled synthesis of zinc oxide by microwave heating using an imidazolium salt. *Inorg. Chem. Comm.* **2004,** *7*, 1003-1005.
17. Baruah, S.; Dutta, J. Hydrothermal growth of ZnO nanostructures *Sci. Technol. Adv. Mater.* **2009,** *10* 013001-18.
18. Yadav, A.; Prasad, V.; Kathe, A. A.; Raj, S.; Yadav, D.; Sundaramoorthy, C.; Vigneshwaran, N. Functional finishing in cotton fabrics using zinc oxide nanoparticles. *Bull. Mater. Sci.* **2006,** *29*, 641–645.
19. Vigneshwaran, N., Kumar,Sampath, Kathe, A A , Varadarajan, P V, Prasad, Virendra Functional finishing in cotton fabrics using zinc oxide nanoparticles. *Nanotechnology* **2006,** *17*, 5087-5095.
20. Bauermann, L. P.; Bill, J.; Aldinger, F. Bio-friendly synthesis of ZnO nanoparticles in aqueous solution at near-neutral pH and low temperature. *J. Phys. Chem. B* **2006,** *110*, 5182-5185.
21. Hamby, D. W.; Lucca, D. A.; Lee, J. K.; Nastasi, M.; Kang, H. S.; Lee, S. Y. Effects of hydrogen implantation on the photoluminescence and carrier mobility of ZnO films. *Nuclear Instruments and Methods in Physics Research Section B: Beam Interactions with Materials and Atoms* **2006,** *249*, 196-199.

22. McCluskey, M. D.; Jokela, S. J.; Zhuravlev, K. K.; Simpson, P. J.; Lynn, K. G., *Infrared spectroscopy of hydrogen in ZnO*. AIP: 2002; Vol. 81, p 3807-3809.
23. Weber, M. H., Lynn, Kelvin G. Hydrogen in red ZnO defects or lattice expansion. *J. Phys.: Conf. Ser* **2011,** *262*.
24. Covington, A. K.; Bates, R. G.; Durst, R. A. Definition of pH scales, standard reference values ,measurement of pH and related terminology. *Pure Appl. Chem.* **1985,** *57*, 531-542.
25. Kong, L.; Yang, J.-X.; Zhou, H.-P.; Tian, Y.-P.; Wu, J.-Y.; Ji, B.-K. A Surfactant-Free, Precursor-Induced Method to Flower-Like ZnO Nanostructures. *Current Nanoscience* **2009,** *5*, 474-478.
26. Moballegh, A.; Shahverdi, H. R.; Aghababazadeh, R.; Mirhabibi, A. R. ZnO nanoparticles obtained by mechanochemical technique and the optical properties. *Surface Science* **2007,** *601*, 2850-2854.
27. Noriega, R.; Rivnay, J.; Goris, L.; Kälblein, D.; Klauk, H.; Kern, K.; Thompson, L. M.; Palke, A. C.; Stebbins, J. F.; Jokisaari, J. R.; Kusinski, G.; Salleo, A., *Probing the electrical properties of highly-doped Al:ZnO nanowire ensembles*. AIP: 2010; Vol. 107, p 074312.
28. Dimitrov, I. G., et al Al doped ZnO thin films for gas sensor application. *J. Phys.: Conf. Ser* **2008,** *113*, 012044.
29. Gong, H.; Hu, J. Q.; Wang, J. H.; Ong, C. H.; Zhu, F. R. Nano-crystalline Cu-doped ZnO thin film gas sensor for CO. *Sensors and Actuators B: Chemical* **2006,** *115*, 247-251.
30. Wu, S. Z., et al Ferromagnetism studies of Cu-doped and (Cu, Al) co-doped ZnO thin films. *J. Phys.: Conf. Ser.* **2011,** *263*, 012022.

Chapter 6

1. Chtanov, A. and M. Gal, *Differential optical detection of hydrogen gas in the atmosphere.* Sensors and Actuators B: Chemical, 2001. **79**(2-3): p. 196-199.
2. Ashida, A., et al., *Optical propagation loss of ZnO films grown on sapphire*. Vol. 95. 2004: AIP. 1673-1676.
3. Holmelund, E., et al., *Pure and Sn-doped ZnO films produced by pulsed laser deposition.* Applied Surface Science, 2002. **197-198**: p. 467-471.
4. Paraguay D, F., et al., *Influence of Al, In, Cu, Fe and Sn dopants on the response of thin film ZnO gas sensor to ethanol vapour.* Thin Solid Films, 2000. **373**(1-2): p. 137-140.
5. Liu, P., Lee, Se-Hee, Cheong, Hyeonsik M., Tracy, C. E., Pitts, J. R., Smith, R. D. , *Stable Pd/V2O5 Optical H2 Sensor.* Journal of The Electrochemical Society, 2002. **149**(3): p. H76-H80.
6. Sarkisov, S.S., et al., *Single-Arm Double-Mode Double-Order Planar Waveguide Interferometric Sensor.* Appl. Opt., 2001. **40**(3): p. 349-359.
7. Viswanatha, R., et al., *Blue-Emitting Copper-Doped Zinc Oxide Nanocrystals.* The Journal of Physical Chemistry B, 2006. **110**(45): p. 22310-22312.
8. Wu, S.Z., et al, *Ferromagnetism studies of Cu-doped and (Cu, Al) co-doped ZnO thin films.* J. Phys.: Conf. Ser., 2011. **263**: p. 012022.
9. Lupan, O., et al, *Synthesis of nanostructured Al-doped zinc oxide films on Si for solar cells application.* Sol. Energ. Mat. Sol C., 2009. **93**: p. 1417-1422.
10. *New Measurement Information System of Biosensor in Relativity Humidity*, J. N. I. T., 2011. **2**(2): p. 31-37.

11. Jung, D, *Syntheses and characterizations of transition metal-doped ZnO.* Solid State Sci., 2010. **12**(4): p. 366-470.
12. Klingshirn, C., et al., *65 years of ZnO research – old and very recent results*. Phys. Status Solid B, 2010. **247**(6): p. 1424-1447.

Chapter 7

1. Freestone, I., Meeks, N., Sax, M., and Higgitt, C., *Lycurgus Cup* Gold Bulletin, 2007. **40**(4).
2. Douglas, T. et al., *Protein Size and Crystallinity in Protein-Templated Inorganic Nanoparticles, Chem. Mater.* 2010. **22(**16): p.4612–4618
3. Evans, D. J. et al, *Virus templated metallic nanoparticles*. Nanoscale, 2010. (2): p. 2596-2600.
4. Preston, T.C. and Signorell, R., *Calf thymus Formation of Gold Particles on Nanoscale Toroidal DNA Assembled with Bis(ethylenediamine)gold(III)*. Lamgmuir, 2010. **26**(12): p. 10250-10253.
5. Berti, Lorenzo, Alessandrini, Andrea, and Paolo Facci, *DNA-Templated Photoinduced Silver Deposition*. J. Am. Chem. Soc. 2005. **127**(32): p. 11216-11217.
6. Hud, N.V., et al., Controlling the size of nanoscale toroidal DNA condensates with static curvature and ionic strength. P.N.A.S., 2003. **100**(16): p. 9296-9301.
7. Samson, J., et al., *Fabrication of Metal Nanoparticles Using Toroidal Plasmid DNA as a Sacrificial Mold.* ACS Nano, 2009. **3**(2): p. 339-344.